Universitat
de les Illes Balears

MASTER'S THESIS

Beyond the Stationary Phase Approximation: an alternative approach to model gravitational waves from precessing compact binaries in the Fourier Domain

Maria de Lluc Planas Llompart

Master's Degree in Advanced Physics and Applied Mathematics

(Specialisation/Pathway *Astrophysics and Relativity*)

Centre for Postgraduate Studies

Academic Year 2020-21

Beyond the Stationary Phase Approximation: an alternative approach to model gravitational waves from precessing compact binaries in the Fourier Domain

Maria de Lluc Planas Llompart

Master's Thesis

Centre for Postgraduate Studies

University of the Balearic Islands

Academic Year 2020-21

Key words:

Gravitational waves, black hole binaries, precession, stationary phase approximation,

Fourier domain

Thesis Supervisor's Name: Sascha Husa

Tutor's Name (if applicable)

Tutor's Name (if applicable)

Abstract

The first detection of gravitational waves of a black hole binary [1] opened the current observational era of gravitational wave astronomy. Several gravitational waves from merging compact binaries have already been observed during the three observational "runs" [2, 3], with the expectation of increasing the detection rate with upgraded and upcoming detectors.

Sophisticated data analysis methods are indispensable for the detection of gravitational waves and it requires theoretical models to estimate the source parameters. Through the "matched filtering" method, the theoretical templates are cross correlated against the observed signal at the detector, so one can infer the source parameters using Bayesian inference. In order to sample the posterior probability distribution of the parameters, Bayesian inference requires at least millions of evaluations of the likelihood function. The better the sensitivity of the detectors, the more accurate and computationally efficient the signal templates need to be. This is why one of the main efforts of the gravitational wave group at the UIB is to improve the current Inspiral-Merger-Ringdown (IMR) waveforms in the Fourier domain, which describe the amplitude and phase needing a low computational cost to evaluate them and hence, making them a reasonable template for applications in Bayesian inference.

In this work I focus on the challenging effect that a complete representation of the spins implies on waveform models, known as *spin precession*. In case of having a black hole binary with misaligned spins, i.e. when the angular momenta of the individual black holes are not orthogonal to the orbital plane, the spin-orbit and the spin-spin couplings induce a precession of the orbital plane and of the spins themselves. This precession leads to a modulation of the signal as seen by the observer, and increases the dimensionality of the problem, which makes it difficult to cover the large parameter space with numerical relativity simulations. However, the fact that the acceleration due to the orbital motion dominates and the power radiated due to precession can be neglected in the inspiral gives rise to a fruitful approach to modelling this effect [4–7]: One can use a (non-inertial) co-precessing frame in which the decomposed waveform is similar to a non-precessing one, performing a time-dependent rotation that follows the precession of the orbital plane. In order to create efficient Fourier domain models, one needs to understand how to translate the time rotation from an inertial frame to the co-precessing one into a Fourier domain transfer function.

Our purpose is thus to implement the formalism developed in [8] in order to process the time domain modulation necessary to treat precession in the Fourier domain, while retaining the compactness of a Fourier domain amplitude and phase representation of the

signal. This new formalism, based on the separation of time-scales between precession and orbital motion directly in the Fourier domain, seeks to overcome the limitations of the Stationary Phase Approximation (SPA) [9]. This method can only be applied to compute the Fourier transform of non-precessing systems, i.e. with aligned spins, during the inspiral, and hence, it is not applicable to IMR precessing waveforms. A better approach than SPA is crucial to deal with the challenging events we may detect with the upgraded and upcoming detectors.

Contents

CHAPTER 1

Introduction to Gravitational Waves

Gravitational waves are ripples in the spatio-temporal distance between observers, which propagate in all directions from their source as transverse waves travelling at the speed of light. In order to emit gravitational waves, the source must have a large time-varying quadrupole moment, which leads to a metric perturbation that carries energy and information about the process. This fact implies that objects that are static or radially oscillating will not produce gravitational waves. The Universe is filled with violent processes which undergo rapid accelerations and hence, produce gravitational waves that can be detected with our instruments. Scientists have defined four categories based on the nature of the signals: Compact Binary Coalescence (CBC), Continuous, Stochastic and Burst.

Compact Binary Coalescences are short duration transients and they are a particularly efficient astrophysical process to generate gravitational waves. Indeed, all the objects LIGO has detected so far fall into this category [2, 3], and mostly in the subclass of Black Hole Binaries (BBH). However, the compact binaries also include those formed by two Neutron Stars (BNS), with a first detection on August 17, 2017 [10], and by a Neutron Star and a Black Hole (NSBH). The first ever detection of this last type of merger was on January 05, 2021, followed by a second event of the same nature just 10 days apart [11]. All three groups are included in the same category because they share the same mechanism of wave-generation: the pair of dense objects revolve around each other, emitting gravitational waves which carry away part of the system's orbital energy. This loss of energy causes the objects to orbit around each other faster, emitting stronger gravitational waves and hence, loosing more energy, inevitably ending with the coalescence of both objects. Since the amount of radiated energy increases as objects get closer together, the more compact and heavier sources, which are black holes, produce gravitational waves that are easier to detect. Continuous gravitational wave models are also well known and understood, and those more likely to detect by LIGO are thought to be produced by a single massive spinning object: a neutron star [12]. The effect of spinning will generate gravitational waves if there is any imperfection in the spherical shape. They are called continuous waves because if the spin-rate of the star is constant, so are the emitted waves, with the same frequency and amplitude. This type of signals are expected to be longer than the ones produced by CBC, but much simpler, since they look as an almost perfect single-frequency sinusoid over short time (like "pure tones"), with a very slow decrease in frequency (*spindown*). However, the longer the signal, the more expensive the searches are, since the matched filtering needs to cover the parameter space extremely densely with templates. There are more examples of continuous gravitational waves: for instance, with LISA we will be able

to detect continuous waves from white dwarf binaries [13].

The other two sources are not as well understood as the previous ones. Although it is very unlikely at the current sensitivities of detectors that two gravitational waves of detectable amplitude pass the Earth at the same time, weak signals can create a background of weak gravitational waves that are filling the Universe, mixed together randomly. Such a background may also have been generated during the first fractions of a second of expansion of the universe [14]. This mix of small waves is called a "Stochastic Signal", and even though they would be difficult to detect, it will allow us to see farther than ever into the universe. Finally, in contrast with the long duration of stochastic waves, burst [15] are those short-duration gravitational waves expected from sources we do not know about or how to model their signals accurately, and hence, we cannot assume they have the well-defined properties of other waveforms. This fact makes its detection a big challenge, but it would also give the most revealing information about the events yet unknown in the universe.

1.1 Einstein Field Equations: Gravitational Waves

General Relativity describes gravity as a geometric property of spacetime, which implies that the dynamical field which creates gravity is the metric tensor describing the curvature of spacetime itself, and not some other field propagating through spacetime. The idea of describing gravity as the geometry of a curved manifold arises from the principle of equivalence. One of the forms of this principle states that, in contrast to what happens for other forces, unaccelerated or freely falling particles follow concrete trajectories, called "geodesics". This can be extended to the Einstein Equivalence Principle: "The outcome of any local non-gravitational experiment in a freely falling laboratory is independent of the velocity of the laboratory and its location in spacetime" [16].

The Einstein's Field Equations (EFE) govern how the spacetime metric responds to energy and momentum. Albert Einstein developed these equations in 1915 in his publication of the theory of general relativity [17] as a generalization of the Poisson equation for the Newtonian potential. An alternative route is through the principle of least action, i.e. the Lagrangian Formulation, which leads to the same relation between the metric and the energy tensor, the EFE:

$$R_{ab} - \frac{1}{2}Rg_{ab} = \frac{8\pi G}{c^4}T_{ab}. \tag{1.1.1}$$

In the previous equation, R_{ab} is the Ricci curvature tensor, R the scalar curvature, g_{ab} the metric tensor, G the Newton's gravitational constant, c the speed of light in vacuum and T_{ab} the stress-energy tensor. The Ricci tensor is defined as a contraction of the Riemann tensor, which is a combination of Christoffel coefficients and its derivatives:

$$R_{ab} = R^{c}{}_{acb} = \frac{\partial \Gamma^{c}{}_{ab}}{\partial x^c} - \frac{\partial \Gamma^{c}{}_{ac}}{\partial x^b} + \Gamma^{c}{}_{ab}\Gamma^{d}{}_{cd} - \Gamma^{c}{}_{ad}\Gamma^{d}{}_{bc}. \tag{1.1.2}$$

The Christoffel symbols $\Gamma^{a}{}_{bc}$ are defined as

$$\Gamma^{a}{}_{bc} = \frac{g^{ad}}{2}\left(\frac{\partial g_{db}}{\partial x^c} + \frac{\partial g_{dc}}{\partial x^b} - \frac{\partial g_{bc}}{\partial x^d}\right). \tag{1.1.3}$$

The scalar curvature R is defined as the trace of the Ricci curvature tensor, $R = g^{ab}R_{ab} = R^a_a$. Taking the trace in Equation (1.1.1), we then find $R = -8\pi GT/c^4$, which plugged into that same equation gives an equivalent expression for the EFE,

$$R_{ab} = \frac{8\pi G}{c^4}\left(T_{ab} - \frac{1}{2}Tg_{ab}\right). \tag{1.1.4}$$

This new form gives a better understanding when considering the stress-energy tensor T_{ab} to be zero in the region under consideration. In Eq. (1.1.4), we see that in that particular case the right term vanishes and the EFE are referred to as *vacuum field equations* or *vacuum Einstein equations*:

$$R_{ab} = 0. \tag{1.1.5}$$

The Einstein Field Equations (1.1.1) are a set of second-order differential non-linear equations for the metric tensor field g_{ab}. The ten unknown functions of the metric components can be found by solving the ten independent equations contained in the EFE. Even though they seem simple written as tensor equations, they are extremely complicated to solve, and the fact that they are non-linear implies that two solutions cannot be superposed to create a third one. It is thus necessary to make assumptions in order to solve them exactly, such as imposing metric symmetries. The Einstein Equations predict the existence of phenomena such as black holes (BHs), the expansion of the universe and also gravitational waves (GWs), which were predicted one year after the publication of the Theory of General Relativity Einstein [18] and detected for the first time roughly 100 years later [1].

The simplest starting point for discussions of GWs is linearized gravity. We will consider the weak-field limit, but not necessarily static, where test particles can move freely. When considering these assumptions, we surpass the Newtonian limit including phenomena which are absent in Newtonian theory, but it is still possible to solve analytically the EFE for the ten metric coefficients g_{ab}. The weakness of the field can be expressed in terms of a metric which is decomposed in a flat Minkowski metric η_{ab} plus a small perturbation h_{ab}

$$g_{ab}(x) = \eta_{ab} + h_{ab}(x),\ |h_{ab}| \ll 1, \tag{1.1.6}$$

where we will restrict the Minkoswky metric to take its canonical form $\eta_{ab} = \mathrm{diag}(-1,1,1,1)$, i.e. to assume that the coordinate system is approximately Cartesian and inertial. Furthermore, the assumption of h_{ab} to be small allow us to neglect anything higher than the first order terms in the metric perturbation and hence permit us to use η^{ab} and η_{ab} to raise and lower indices, since the corrections would be higher than the perturbation:

$$g^{ab}(x) = \eta^{ab} - h^{ab}(x),\ h^{ab} = \eta^{ac}\eta_{bd}h_{cd}. \tag{1.1.7}$$

One can now study both the gravitational radiation itself, i.e. its propagation in the absence of sources ($T_{ab} = 0$), and then consider the equations coupled to energy so we can determine which kind of sources can generate gravitational waves.

The linearized Einstein vacuum equations are obtained inserting Eq. (1.1.6) into Eq. (1.1.5) and expanding it to first order in $h_{ab}(x)$. The first term obtained in this expansion is the Ricci curvature of flat spacetime, which vanishes, and the second, the linearized equation. If we substitute Eq. (1.1.6) into Eq. (1.1.3), we obtain the first-order perturbation terms of the Christoffel symbols – the zeroth order vanishes since the

components of η_{ab} are constant:

$$\delta\Gamma^c_{ab} = \frac{1}{2}\eta^{cd}\left(\frac{\partial h_{da}}{\partial x^b} + \frac{\partial h_{db}}{\partial x^a} - \frac{\partial h_{ab}}{\partial x^d}\right). \tag{1.1.8}$$

If we now insert Eq. (1.1.8) into Eq. (1.1.2), noticing that the last two terms do not contribute because they are of second order in h_{ab}, we obtain the perturbation of the Ricci tensor:

$$\delta R_{ab} = \frac{\partial \delta\Gamma^c_{ab}}{\partial x^c} - \frac{\partial \delta\Gamma^c_{ac}}{\partial x^b}. \tag{1.1.9}$$

The linearized EFE in vacuum are then obtained by substituting Eq. (1.1.8) into Eq. (1.1.9)

$$\delta R_{ab} = \frac{1}{2}[-\Box h_{ab} + \partial_a V_b + \partial_b V_a] = 0, \tag{1.1.10}$$

where $\Box = \eta^{ab}\partial_a\partial_b$ is the flat-space wave operator (d'Alembertian), G and c has been set to 1 and the vector V_a is defined as

$$V_a = \partial_c h^c_a - \frac{1}{2}\partial_a h^c_c. \tag{1.1.11}$$

The Equation (1.1.10) contains a set of ten linear, partial differential equations for the metric perturbation $h_{ab}(x)$. Since coordinates are arbitrary, one can simplify the solution by an smart choice of coordinates, as long as this new set leaves the components of η_{ab} unchanged. If we now consider the change

$$x'^a = x^a + \xi^a(x), \tag{1.1.12}$$

where $\xi^a(x)$ are four arbitrary functions of the same small size as $h_{ab}(x)$, it implies the following metric transformation:

$$g'_{ab}(x') = \frac{\partial x^c}{\partial x'^a}\frac{\partial x^d}{\partial x'^b} g_{cd}(x) = \eta_{ab} + h'_{ab} = \eta_{ab} + (h_{ab} - \partial_a\xi_b - \partial_b\xi_a). \tag{1.1.13}$$

Hence, adding a term $\partial_a\xi_b + \partial_b\xi_a$ to the metric perturbation is physically equivalent to the change of coordinates in Eq. (1.1.12). Indeed, this *gauge transformation* is analogous to the one of the vector potential in electromagnetism: $A_a \to A_b + \partial_a\Lambda$. $\xi^a(x)$ are arbitrary functions, and hence they can be chosen so that the vector defined in Eq. (1.1.11) in this new set of coordinates verifies $V'_a(x) = 0$, the so called *harmonic gauge condition*. In fact, one can assume that the initial coordinate system already satisfies this condition, $V_a(x) = 0$, which simplifies Eq. (1.1.10) to

$$\Box h_{ab} = 0. \tag{1.1.14}$$

Equation (1.1.14) is the simplest form to write the linearized Einstien equations in vacuum. As any wave equation, it admits as a solution a superposition of plane waves, the *gravitational waves*, which propagate at the speed of light. Then, a general solution to this equation can be written as

$$h_{ab}(x) = A_{ab}e^{i\mathbf{k}\cdot\mathbf{x}}, \tag{1.1.15}$$

where A_{ab} is a 4×4 matrix, symmetric and corresponds to the amplitudes of the different wave components. Indeed, this matrix is not arbitrary and the choice of an appropriate set of coordinates can simplify it. One can show by explicit calculations that the metric

perturbation is purely spatial, i.e. $h_{tj} = 0$, and also traceless, $h^b_b = 0$. In addition, the *harmonic gauge condition*, which consisted in setting $V_a(x) = 0$, implies that the metric perturbation, besides spatial, it is also transverse, i.e. $k^j a_{tj} = \partial_a h_{ab} = 0$, and also verifies that $a_{tt} = 0$. This is the so-called *transverse-traceless (TT) gauge* and it fixes the local gauge freedom. If we now set the z-axis in the propagation direction of the wave, the amplitude matrix is reduced to a 2×2 traceless and symmetric matrix in the x-y plane. This exhibits the fact that gravitational waves have only two local degrees of freedom, which are called the h_+ and $h_\times$ polarizations:

$$h_{ab}(x) = \begin{bmatrix} 0 & 0 & 0 & 0 \\ 0 & h_+ & h_\times & 0 \\ 0 & h_\times & -h_+ & 0 \\ 0 & 0 & 0 & 0 \end{bmatrix} e^{i\mathbf{k}\cdot\mathbf{x}}. \tag{1.1.16}$$

One can now discuss the effects of the two polarizations separately. Their effect on a circle of test particles is to distort them into ellipses oscillating in + and × patterns, respectively, as seen in Figure 1.1.

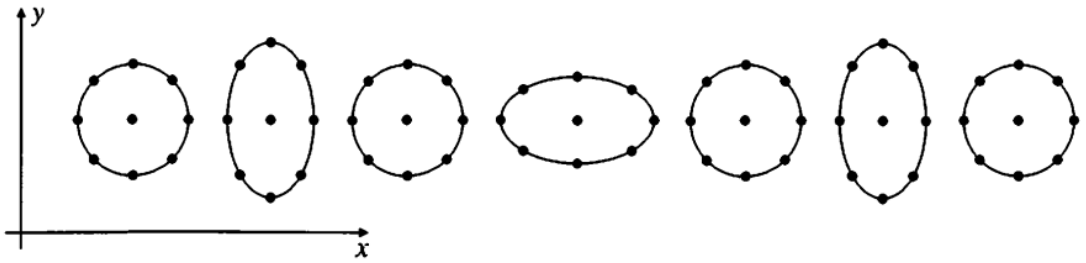

1.1.1: + polarization: particles are distorted into ellipses which oscillate in a + pattern.

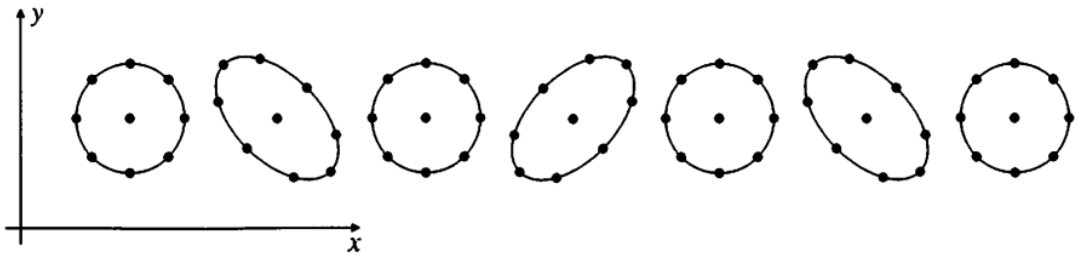

1.1.2: × polarization: particles are distorted into ellipses which oscillate in a × pattern.

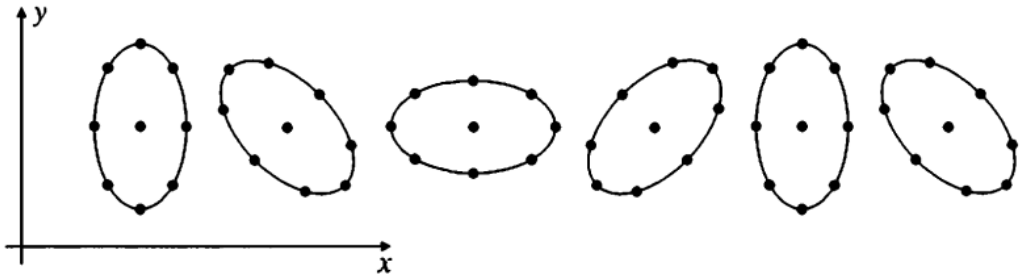

1.1.3: R polarization: particles are distorted into an ellipse which rotates in a right-handed sense.

Figure 1.1: Effect of a gravitational wave with different polarizations on a circle of test particles. Credit: [19].

We can also consider the right and left handed circularly polarized modes, defining them as

$$h_R = \frac{1}{\sqrt{2}}(h_+ + ih_\times), \quad h_L = \frac{1}{\sqrt{2}}(h_+ - ih_\times). \tag{1.1.17}$$

The effect of these two polarizations are the rotation of the particles in a right or left-handed sense, respectively, including the h_R polarization in Figure 1.1.3.

Hence, all the degrees of freedom of the EFE (1.1.1) have been reduced to two polarization states h_+ and $h_\times$, which can be written as

$$\begin{aligned} h_+(t,r) &= A_+ \cos\left(\omega\left(t - \frac{r}{c}\right) + \Phi_+\right), \\ h_\times(t,r) &= A_\times \cos\left(\omega\left(t - \frac{r}{c}\right) + \Phi_\times\right), \end{aligned} \tag{1.1.18}$$

where the amplitudes $A_{+/\times}$, frequency ω and phases $\Phi_{+/\times}$ give all the astrophysical information.

Let us now consider the EFE coupled to matter in order to discuss the generation of gravitational waves. In this case we need to consider Equation (1.1.1) with non-vanishing T_{ab}, so we cannot assume the transverse-traceless form we derived before. However, the same way it has been done for the vacuum equations, one can use gauge transformations to impose gauge conditions on the metric perturbation. If we consider again the Lorentz Gauge $V_a(x) = 0$, the four conditions on h_{ab} can be simplified if we define a trace-reversed amplitude as

$$\bar{h}_{ab} = h_{ab} - \frac{h}{2}\eta_{ab}, \quad \bar{h} = \eta^{ab}\bar{h}_{ab} = -h, \quad \bar{h}^{TT}_{ab} = h^{TT}_{ab}, \tag{1.1.19}$$

since this way the harmonic condition becomes

$$\frac{\partial \bar{h}^{ab}}{\partial x^b} = 0. \tag{1.1.20}$$

We have shown that the left-hand side of the EFE (1.1.1) in the harmonic gauge takes the form $\delta R_{ab} = -1/2\Box h_{ab}$, which implies $\delta R = -1/2\Box h$. Setting G=c=1,

$$\delta R_{ab} - \frac{1}{2}\delta R g_{ab} = 8\pi T_{ab}, \tag{1.1.21}$$

and the linearization of the Einstein equation (1.1.1) is thus

$$\Box \bar{h}_{ab} = -16\pi T_{ab}. \tag{1.1.22}$$

The solution to this last equation can be obtained using a Green function. The Green function $G(x^d - y^d)$ for the $\Box$ operator is the solution of

$$\Box_x G(x^d - y^d) = \delta^{(4)}(x^d - y^d), \tag{1.1.23}$$

which has two possible solutions, which can be thought of as "retarded" or "advanced" (waves travelling forward or backward in time). We will be interested in the retarded solution, which allows the following general solution for the perturbation (see any textbook development e.g. [19])

$$\bar{h}_{ab}(t,\mathbf{x}) = 4\int \frac{1}{|\mathbf{x}-\mathbf{y}|} T_{ab}(t_r,\mathbf{y}) d^3y, \tag{1.1.24}$$

where the retarded time is defined as $t_r = t - |\mathbf{x} - \mathbf{y}| = t - r$. From this last equation we see that the disturbance at $(t, \mathbf{x})$ is the sum of the contributions at the point $(t_r, \mathbf{x} - \mathbf{y})$ on the past light cone. One can now impose some simplifications: we consider the source isolated, far away, and slowly moving (i.e. non-relativistic motion). Working in the Fourier domain, one can find a compact form for the trace-reversed perturbation in terms of the Fourier transform of the quadrupole moment tensor of the energy density, defined as

$$I_{ij}(t) = \int d^3y T^{00}(t, \mathbf{y}) y_i y_j = \int d^3y \rho(t, \mathbf{y}) y_i y_j, \tag{1.1.25}$$

where ρ denotes the mass density. The traceless mass or reduced quadrupole moment can thus be defined as

$$Q_{ij}(t) = \int \rho(t, \mathbf{y}) d^3y \left(y_i y_j - \frac{1}{3} r^2 \delta_{ij} \right) = I_{ij} - \frac{1}{3} \delta_{ij} \delta^{kl} I_{kl}. \tag{1.1.26}$$

Transforming the perturbation expression in terms of Q_{ij} back to the time domain, we obtain the quadrupole formula, which gives the expression for the metric perturbation if we are far away from the source

$$\bar{h}_{ij}(t, \mathbf{x}) = \frac{1}{r} \frac{2G}{c^4} \frac{d^2 Q_{ij}}{dt^2} \left(t - \frac{r}{c} \right), \tag{1.1.27}$$

where all the c and G factors have been added back. We thus see that the gravitational wave produced by the simplified source we have considered is proportional to the second derivative of the quadrupole moment when the observer's past light cone intersects the source. If we compare the gravitational radiation with the electromagnetic one, we see that the leading contribution for this last comes from the dipole moment of the charge density. Since the quadrupole moment is smaller than the dipole moment, gravitational waves are hence much more weaker than the electromagnetic radiation. One now could think about the energy emitted via gravitational waves, which explicit calculations lead to the following expression for the luminosity or power of gravitational waves

$$L = \frac{G}{5c^5} \sum_{ij} \left\langle \left(\frac{d^3 Q_{ij}}{dt^3}(t_r) \right)^2 \right\rangle, \tag{1.1.28}$$

These expressions in terms of the quadrupole moment give us an intuition of the possible sources of gravitational waves. Indeed, they give quantitative good results for sources with weak gravitational fields, although the complete description (numerical integration of the EFE) is needed when considering high strong fields.

1.2 Gravitational wave detections

The emission of gravitational waves is thus related to an energy loss, which in the conditions explained above, is ruled by Equation (1.1.28). This fact made it possible to indirectly prove the existence of gravitational waves through pulsars, rapidly rotating neutron starts with radio emission. The discovery of the relativistic binary pulsar PSR B1913+16 in 1974 by Russell A. Hulse and Joseph H. Taylor permitted to verify that the change in the orbital motion of the binary (obtained by the pulsar emission) followed approximately the quadrupole formalism prediction [20]. This was the first ever proof of the existence of gravitational waves, which was awarded the Nobel Prize in Physics in 1993. This proof

rejected the idea of gravitational waves being a mathematical artefact and encouraged scientist to directly measure gravitational waves. After several attempts, at first using resonant mass detectors, and then, interferometers, the first direct detection was achieved on September 14, 2015 by the Advanced Laser Interferometer Gravitational-Waves Observatory (LIGO) [1]. This first detected gravitational wave was emitted by a black hole binary with initial masses of $36^{+5}_{-4}M_{\odot}$ and $29^{+4}_{-4}M_{\odot}$. There have been three observation "runs" (O1, O2, O3), carried out with the advanced generation of interferometric gravitational wave detectors, and black hole binaries are the main source of the detections done so far. In general, compact binaries are a particularly efficient way to accelerate bodies, and concretely black holes, the most compact (known) objects, can become closer and hence, create stronger gravitational waves. Between observation runs, the detectors are upgraded, some other detectors become operative and their sensitivity increases further. LIGO has played a role in all detections to date, with the Virgo detector [21] joining during the second observation run. The GEO600 detector [22] began taking data simultaneously with Advanced LIGO on September 18, 2015. During O1 and O2, the LIGO-Virgo collaboration detected 11 GW events [2], including the first ever detection of a black hole merger [1] and also the merger of a binary neutron star on August 17, 2017 [10]. The third observation run was suspended on March 26 2020 [23] due to the COVID-19 pandemic, approximately a month before its planned end. On 25 February 2020, during this last observational run, the Kamioka Gravitational Wave Detector KAGRA [24] in Japan became operational, joining LIGO and Virgo during the second part of O3. Fifty-six detection candidates from this run have been publicly announced on `gracedb.ligo.org`, and a first report on the discoveries from compact binary coalescences detected by Advanced LIGO and Advanced Virgo in the first half of this run (O3a) present 39 candidate gravitational wave events [3]. The catalog includes for the first time events with asymmetric mass ratios, for instance [25], and the first two ever detections of BHNS mergers [11]: GW200105, GW200115. The sources have component masses of $8.9^{+1.2}_{-1.5}$M$\odot$ and $1.9^{+0.3}_{-0.2}$M$\odot$ for GW200105 and $5.7^{+1.8}_{-2.1}$M$\odot$ and $1.5^{+0.7}_{-0.3}$M$\odot$ for GW200115. There is also another potential NSBH candidate: the event GW190814, an observation of a compact binary coalescence involving a 22.2 - 24.3 M$\odot$ black hole and a compact object with a mass of 2.50 - 2.67 M$\odot$ [26]. Another important event of this last observational run is GW190521, the first observational evidence of an intermediate mass black hole in the pair-instability mass gap [27, 28]. The next observation run, O4, is planned to start at the end of 2022 and will reach the design sensitivity of the detectors. Further detector upgrades after O4 are already scheduled and also new incorporations: the one from the Indian Initiative in Gravitational-wave Observations LIGO India [29], planned to become operative in 2023, the Einstein Telescope ET [30] and the first space-based detector, the Laser Interferometer Space Antenna LISA [31] , both planned to become operative during the 2030s. During the following runs, we will thus be able to detect phenomena much more massive than those detected up to date by our current detectors, such as mergers of supermassive black holes, which are typically found at the centers of galaxies, and also gravitational waves from other sources than compact coalescences.

1.2.1 Gravitational wave interferometers

Interferometers were first invented in the 19^{th} century by Albert Michelson, and nowadays are widely used in many fields due to their possibility to perform very small measurements, otherwise impossible to achieve. In the particular case of gravitational waves, they are able

to measure distances of ten thousandth times the size of a photon. They work essentially as Michelson interferometers, merging two sources of light to create an interference pattern which contains information about the phenomenon observed. Gravitational waves distort the space-time as they travel, stretching in one direction and compressing in the perpendicular one, as seen in Figure 1.1. LIGO interferometers have orthogonal arms, see 1.2, so when a gravitational wave passes by, it causes one of the arms to get longer, and the other one shorter, motion known as "differential arm" motion. The change in length of the arms varies the distance the laser beams travel, which leads to an interference phase which transmits an optical signal proportional to the strain of the wave. A simplified scheme of the aLIGO interferometer can be seen in Figure 1.2.2. Other arm configurations are also possible, and for instance, LISA and the ET will have three arms.

1.2.1: Areal views of the the LIGO Hanford and LIGO Livingston interferometers. Credits: LIGO Caltech [32]

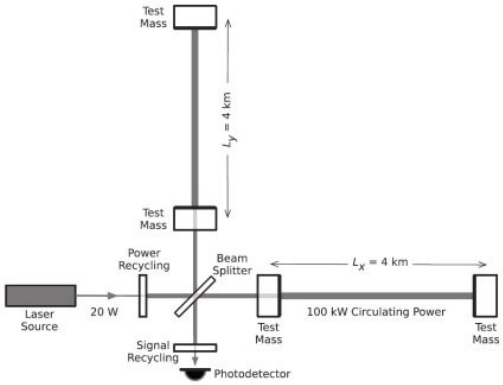

1.2.2: Diagram of a simplified LIGO interferometer. Credit: [1]

Figure 1.2: LIGO interferometers.

Although the main idea is simple, in practise it is not. The physical effect of a gravitational wave is to perturb the relative positions of the test particles in the interferometer arms. If the two masses are separated by a distance L and the strain of the wave is h, then the change in their distance will be approximately given by

$$\frac{\delta L}{L} \sim h. \tag{1.2.1}$$

The strain of the first ever detection [1] was of the order of 10^{-21}, which following Equation (1.2.1) implies that the sensitivity has to reach

$$\delta L \sim 10^{-16} \left(\frac{h}{10^{-21}}\right) \left(\frac{L}{km}\right) cm. \tag{1.2.2}$$

Due to this high resolution, great efforts need to be done in order to reduce all kind of noise sources and optical phase fluctuations. The sensitivity curve of the detector is thus obtained as the sum of all the noise contributions, which depend on the frequency. The noise curve of the Advanced LIGO detector during the first observational run O1 can be seen in Figure 1.3.

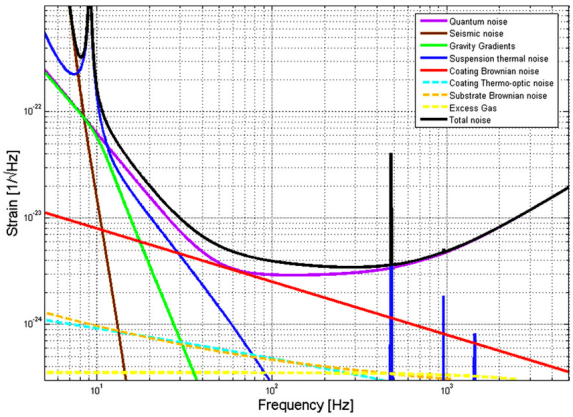

1.3.1: Model for the different noise contributions for the aLIGO detectors and the resulting curve, obtained using the GWINC-v2 software package. Credit: [33].

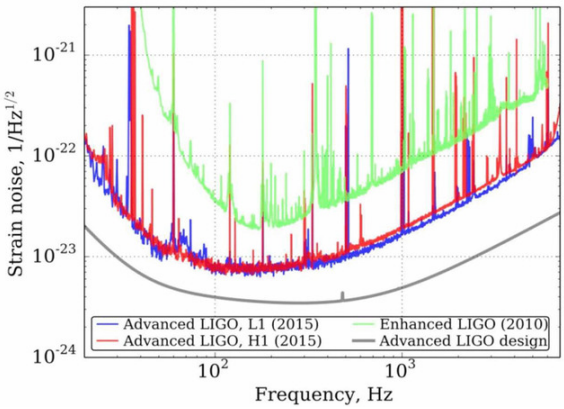

1.3.2: Spectral amplitude of the total strain noise in units of strain per $\sqrt{Hz}$. Credit: [34].

Figure 1.3: Sensitivity of the Advanced LIGO detectors during O1 (September 2015-January 2016).

Figure 1.3 shows a model for some of the noise contributions and the total noise curve, and then the real curve during the first observation run. Also, in the right plot one can see that the sensitivity increased with respect to the Enhanced LIGO detectors, especially in the low frequency band. The limitation at low and high frequencies is what makes the coalescence of compact binaries the easiest phenomena to detect, as can be seen in Figure 1.4. In fact, the most sensitive frequency band is between 100 and 300 Hz, which corresponds to the merger of black holes with stellar masses.

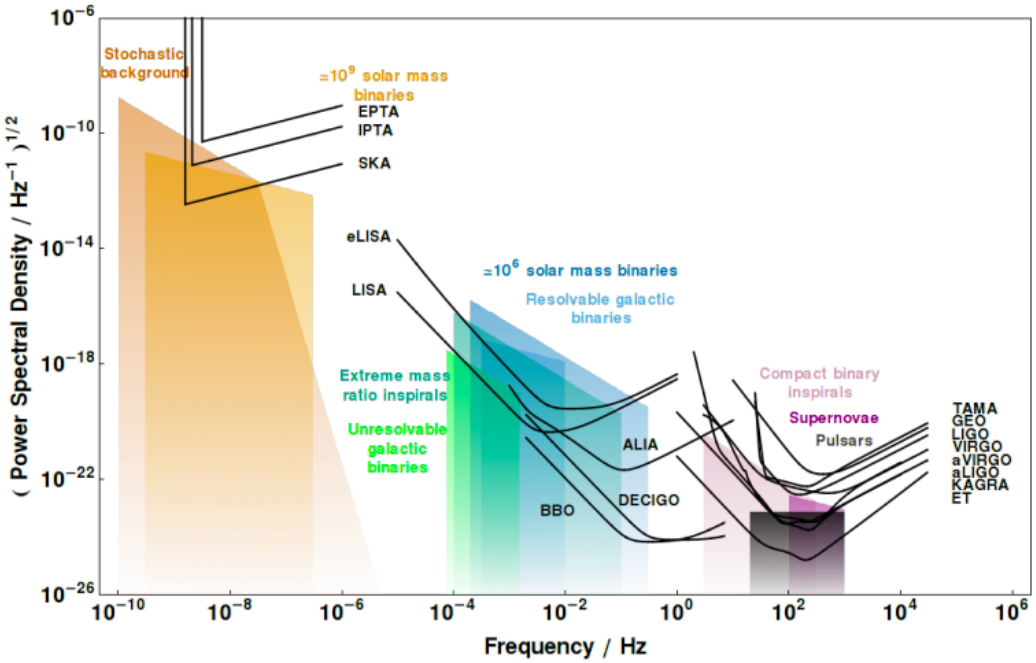

Figure 1.4: Square root of the power spectral density, the so called power spectral amplitude, with some of the possible sources of gravitational waves and the sensitivity of some of the detectors. Source: [35].

Inspiralling massive black holes merge together faster, which implies that they can only reach low frequencies, whereas lighter black holes can inspiral together closer, achieving high frequencies, both cases implying that the merger can be outside of the frequency band of our ground-based detectors. The low frequency limit is established by fluctuating Newtonian gravity gradients and Earth vibrations and hence, this lower frequency band can be achieved with space-based detectors such as LISA. These detectors can reach up to 10^{-4}Hz, which permits to detect much more massive phenomena. Some of the possible sources of gravitational waves and the detectors capable to detect them are included in Figure 1.4.

1.3 Data analysis

The output of the detector is a time series $x(t)$, which includes all the noise fluctuations mentioned before, $n(t)$, and also a possible GW signal $s(t)$, so $x(t) = s(t) + n(t)$. The detector will store the data every step of time Δt with a sampling frequency $f = 1/\Delta t$ during a finite time, so

$$t_j = t_0 + j\Delta t \;\rightarrow\; x(t_j) = x_j = s_j + n_j \;,\; j = 0, 1, ..., N-1. \tag{1.3.1}$$

In signal processing, it is useful to consider the frequency-domain representation of the time series. One can find in Appendix A the Fourier conventions we are using in this project, as well as some of the main theorems and definitions.

1.3.1 Noise Characterization

The overall effect of noise can often be well described as a random process, which is usually assumed to be Gaussian-distributed. This is a consequence of the *Central Limit Theorem*, which ensures that a process that arises from a large number of subprocesses will be approximately Gaussian, regardless of the probability distribution of each of the individual random variables. We will refer to noise as *white noise* if the processes are frequency independent, whereas it will be *coloured* when the signal does not have equal power in every band of a given bandwidth. Finally, a random process is said to be *stationary* if its statistical properties are independent of time. In that case, the *Ergodic Theorem* establishes that the time averages over a particular realisation $n(t)$ are equivalent to the ensemble averages over different realisations of the random process. When considering a sufficiently small frequency band or a short time, then the detector noise can be considered as white, stationary and Gaussian, as a first approximation. Moreover, without loss of generality, one can assume that $\langle n(t) \rangle = 0$. For a stationary random process $n(t)$, one can use the Ergodic theorem to rewrite the autocorrelation function $C_n(t)$ (A.3.3) as

$$C_n(t) = \lim_{T\to\infty} \int_{-T/2}^{T/2} dt' n(t') n(t+t') = \langle n(t') n(t+t') \rangle. \tag{1.3.2}$$

$C_n(0)$ corresponds to the second moment $\langle n^2 \rangle$ of the random process, and if n has 0 mean, then it also is equal to the variance of n σ_n^2. For white processes, the values of the series are statistically independent, so in that case, $C_n(t)$ will be proportional to a Dirac delta function $\delta(t)$. Using Equation (A.3.4) then one can see that white noise has a flat power spectrum, which implies that the total power is equally distributed in frequency. Using the result found in Equation (1.3.2) and the definition of the Power Spectral Density in

Equation (A.3.4), one can find a definition for the noise description when considering stationary gaussian noise

$$S_n(f) = 2\int_{-\infty}^{\infty} dt\langle n(t')n(t+t')\rangle e^{-2i\pi ft}, \tag{1.3.3}$$

from which one can deduce that, in the frequency domain, the components are statistically independent when $f \neq f'$:

$$\langle \tilde{n}(f)\tilde{n}^*(f')\rangle = \delta(f-f')\frac{S_n(f)}{2}. \tag{1.3.4}$$

Since $n(t)$ is dimensionless, then $S_n(f)$ has dimensions of Hz^{-1}. The noise of the detector can be thus characterized by $\sqrt{S_n(f)}$, which is called the *spectral amplitude* (see Figures 1.3 and 1.4). In those Figures, we see that each curve has a characteristic frequency dependence, which implies that the noise of the gravitational wave detectors is colored. Moreover, real noise is not perfectly Gaussian, but it can be considered as a superposition of Gaussian noise and non-Gaussian artefacts: "lines" and "glitches". The spectral lines are artifacts at fixed frequencies from periodic processes in the detector and its environment, such as the power lines of electrical input. "Glitches" are brief, loud noise artifacts which are environmental or instrumental but can mimic gravitational waves.

One needs to be able to detect a signal $s(t)$ which is much weaker than the noise $n(t)$ of the detector output $x(t)$. The matched-filtering [36] (for a textbook development see e.g. [37] ch. 7) is the optimal method to detect possible signals in Gaussian noise if these signals can be predicted theoretically. This method will be described in the next section.

1.3.2 Matched Filtering: Detections & Parameter Estimation

The main idea of matched filtering is to compute the scalar product or "match" between the output of the detector $x(t)$ and a filter function $h(t)$, chosen such that it maximizes the signal-to-noise ratio (SNR). The SNR is by definition the quotient of S, the expected value of the filtered value when the signal is present, and N, which is the root-mean-squared value of the filtered data when the signal is absent. Taking into account the definition of the one-sided PSD $S_n(f)$, and remembering that $\langle n(t)\rangle = 0$, it can be shown that

$$\mathrm{SNR} = \frac{S}{N} = \frac{\int_{-\infty}^{\infty} df\tilde{x}(f)\tilde{h}^*(f)}{\left(\int_{-\infty}^{\infty} df\frac{S_n(f)}{2}|\tilde{h}(f)|^2\right)^{1/2}}. \tag{1.3.5}$$

We can now define the scalar product between two real variables in terms of $S_n(f)$:

$$(A(t)|B(t)) = 4\cdot \mathrm{Re}\int_0^{\infty} df\frac{\tilde{A}^*(f)\tilde{B}(f)}{S_n(f)}. \tag{1.3.6}$$

This definition of the scalar product leads to the following expression for the SNR

$$\mathrm{SNR} = \frac{(s|u)}{(u|u)^{1/2}}, \text{ with } \tilde{u}(f) = \frac{S_n(f)}{2}\tilde{h}(f). \tag{1.3.7}$$

Now it is clear which is the template h that maximizes the SNR (1.3.7): it has to be chosen so the scalar product with s is maximum, i.e., choosing u parallel to h, getting

$$\tilde{h}(f) \propto \frac{\tilde{s}(f)}{S_n(f)}. \tag{1.3.8}$$

Inserting this solution for the optimal filter into Eq. (1.3.7), we get the optimal value of the SNR

$$\mathrm{SNR}^2_{opt} = (s|s) = 4\int_0^\infty df \frac{|\tilde{s}(f)|^2}{S_n(f)}. \tag{1.3.9}$$

In order to efficiently cover the physical parameter space of the signals with our waveform models or templates h, one needs to construct a *template bank*, which consists of a set of filters for various points in parameter space. There is a geometric method for determining the template placement [38], based on the *mismatch* between templates, which uses a metric defined on the space of signal parameters. For Gaussian noise, this would be the optimal search strategy: to optimize the SNR over the templates h. However, the detector's noise is not completely Gaussian, and hence, more tests are needed to confirm a detection. Detections then not only correspond to statistically significant peaks in the SNR, but also it is necessary to perform the χ^2 test, see for instance [1, 39, 40], which permits to discriminate between signal and noise.

This first step is what is known as a "search" (see e.g. [40]), which delivers statistically significant detections, optimized to maximize the detection rate and minimize the false alarm rate. There are different ways to perform searches based on the different sources which can produce gravitational waves, ranking the events according to an appropriate detection statistic. Unmodelled signals can be detected by the *generic transient searches*, since these operate without a concrete waveform model and only classify the detections according to their amplitude and frequency evolution. The *matched filter binary coalescence searches* are dedicated exclusively to the detection of gravitational waves from binaries of compact objects. It calculates the matched-filter signal-to-noise ratio (1.3.5) and identifies its maximum in time within a template bank of possible signals. The separation between templates is optimized for reasons of computational efficiency, and hence matched-filter searches only provide a rough estimation of the source parameters. It is thus necessary a more detailed follow-up analysis to determine the complete features of the source, which is the second step of data analysis, known as "parameter estimation". During this second step, approximately $10^7 - 10^9$ models based usually on general relativity are used, in front of the approximately 10^5 templates used during binary coalescence searches.

"Parameter estimation" [41] uses the methods of Bayesian inference [42] to measure the parameters of the source, both the intrinsic parameters (masses and spins) and the extrinsic parameters (sky location, distance, inclination, polarization and coalescence phase). These analysis provide the distribution of the source parameters and also estimates of the errors. Bayesian inference describes the state of knowledge about an unknown parameter as a probability density, denoted as $p(\theta, H)$, where $\int p(\theta, H) = 1$. Bayes' theorem permits to obtain an updated (posterior) probability distribution $p(\theta|d, H)$ of the source parameter we are looking for from its prior probability distribution $p(\theta, H)$ and the received data d from the experiment:

$$p(\theta|d, H) = \frac{p(\theta|H)p(d|\theta, H)}{p(d|H)}. \tag{1.3.10}$$

Therefore, parameter estimation using Bayesian inference provides a probability distribution of the source parameters.

1.4 Outline

This project is motivated by the need for accurate and computationally efficient waveform models for parameter estimation. In this project we will focus on the improvement of phenomenological Fourier domain models for waveforms coming from binary black hole systems with misaligned spins, which exhibit a phenomenon known as *spin precession*. The rest of the text is then organised as follows:

Chapter 2 gives an overview of gravitational waves coming from black hole binaries. This chapter introduces general features, the characterization of the waveform during the different phases of the coalescence and some of the approaches used to perform waveform models.

Chapter 3 is focused on the case of precessing waveforms. It will describe the direct effects of precession, as well as the main approach to deal with it: to decompose the waveform in a co-precessing frame in where it is similar to the one generated by a non-precessing system. Some of the methods used to perform precession will also be mentioned.

Chapter 4 introduces the Fourier domain description of precession. It describes the SPA approximation, which is the method used to translate the time domain modulation of precession into the frequency domain, a concrete phenomenological frequency domain model, IMRPhenomXPHM, and then an alternative algorithm to surpass the SPA. This algorithm, proposed in Ref. [8], has been implemented for this work.

Chapter 5 shows the results obtained after applying the formalism described in Section 4.3 to precessing binary systems.

Chapter 6 discusses the formalism implemented in this project, its relevance for the upcoming O4 run as well as future work on this topic.

Appendix A features additional material about the Fourier domain representation, including the convention used in this project, as well as some essential theorems.

CHAPTER 2

Gravitational Waves from Black Hole Binaries

Black hole binary (BHB) mergers are key sources of gravitational waves, and most detected events are of this type, from the first ever detection [1] to most of the detections published to date [2, 3]. In order to produce gravitational waves, bodies need to be accelerated so they vary their quadrupole moment, as shown in Equation (1.1.27). A particularly efficient way to accelerate masses is through orbital motion, so compact binaries become a clear target for gravitational wave detections. The rate of the orbital motion determines the amount of energy radiated, and the distance between objects determines the orbital frequency: the closer the objects, the higher is this frequency and hence, the power radiated. Since black holes are the most compact astrophysical bodies, they are the most effective known source of gravitational waves. In this Chapter we will first discuss briefly the main features of black holes and then we will focus on the description of the gravitational wave signal coming from black hole binaries, explaining the more basic physics involved and the current approaches used to model these signals.

2.1 Black Holes

A black hole is a region of spacetime where neither matter nor radiation can escape due to the strong gravity. These objects are predicted by the theory of general relativity, and they can be found as solutions to the EFE (1.1.1). The first solution that characterized black holes was found by Karl Schwarzschild in 1916 [43], a few months after the publication of general relativity. In Schwarzschild coordinates (t, r, θ, ϕ), the Schwarzschild metric is given by

$$\mathrm{d}s^2 = -\left(1 - \frac{R_s}{r}\right) c^2 \mathrm{d}t^2 + \left(1 - \frac{R_s}{r}\right)^{-1} \mathrm{d}r^2 + r^2(\mathrm{d}\theta^2 + \sin^2\theta \mathrm{d}\phi^2), \tag{2.1.1}$$

where R_s is the Schwarzschild radius $R_s = \frac{2GM}{c^2}$. This solution describes the gravitational field of an object with mass M, with spherical symmetry, stationary and in the vacuum region. At sufficiently large distances (compared to R_s), the Schwarzschild metric is asymptotic to Minkowski space, and indeed at large distance the solution agrees with the Newtonian description of gravity. The line element has two singularities: one at $r = 0$, which is a curvature singularity, and a coordinate singularity at the Schwarzschild radius. The physical interpretation of this second singular point was not understood at that time, but now this surface is known as the *event horizon*, where causal influences

can only cross it in one direction. This in fact corresponds to a null surface, consistent with $g_{tt}(R_s) = 0$. This singularity can be avoided in suitable coordinates: a complete description of the Schwarzschild metric was found by Martin Kruskal [44], introducing the Kruskal-Szekeres coordinates, which cover the entire manifold. This last result was published at the beginning of the golden age of general relativity, when also the discovery of pulsars encouraged the study of compact objects. During this period more general solutions for black holes were found. In 1963, Roy Kerr found the equilibrium solution of rotating black holes [45] and in 1965, Ezra Newman solved the Einstein Equations for a point mass that is both rotating and charged [46]. The no-hair theorem [47, 48] also emerged during the golden era and it states that a stationary black hole solution is completely described by only the three parameters included in the Newman solution: the mass M, the charge Q and the angular momentum $\mathbf{J}$. Moreover, although the mass of a black hole can take any positive value, the other two quantities need to satisfy the following constraint (in geometric units $G = c = 1$)[49]:

$$Q^2 + \frac{J^2}{M^2} \leq M^2. \tag{2.1.2}$$

The gravitational collapse of stars is a known fortation channel of black holes. This phenomenon occurs when the internal pressure cannot support its own gravity, which usually happens because there is insufficient "fuel" to maintain the stellar nucleosynthesis, and hence the temperature is not high enough to prevent the gravitational collapse. If the mass of the remnant, i.e. the mass of the object that remains after the explosion, exceeds the Tolman-Oppenheimer-Volkoff limit [50] (between 2 or $3M_\odot$) then there is no degeneracy pressure able to stop the collapse, and the object inevitably collapses to form a black hole. Due to the strength of the electromagnetic force, these black holes are expected to be neutral, the same way the predecessor star is. If a net charge is present in an astrophysical body, then it would repel and attract particles, so it would eventually be neutralized. Rotation is however an expected property of general black holes, and according to Equation (2.1.2) the angular momentum needs to satisfy

$$J \leq \frac{GM^2}{c}. \tag{2.1.3}$$

We can now define a dimensionless spin parameter $\chi = \frac{cJ}{GM^2}$ such that

$$0 \leq \chi \leq 1. \tag{2.1.4}$$

General black holes will be thus determined by their mass and their angular momentum or spin, and are referred to as *Kerr black holes*, named by Roy Kerr, who found their equilibrium solution. Nevertheless, they are usually classified according exclusively to their mass (see Figure 2.1.1). The detection of gravitational waves from black hole binary systems also contributes to the understanding of the possible mass range of black holes. Figure 2.1.2 shows the masses of the compact objects observed either by electromagnetic messengers or gravitational waves until now.

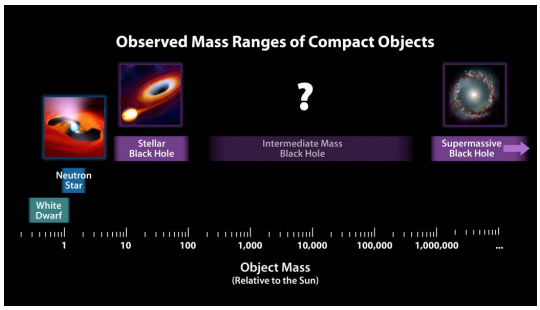

2.1.1: Relative masses of super-dense cosmic objects. Image credit: NASA/JPL-Caltech.

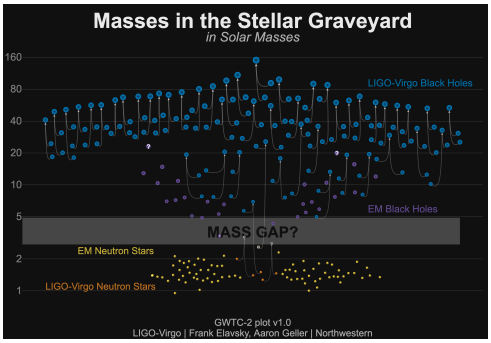

2.1.2: Masses of compact objects detected so far. Credit: LIGO-Virgo/ Frank Elavsky, Aaron Geller/ Northwestern [3].

Figure 2.1: Black hole mass distribution.

Of particular interest will be intermediate-mass black holes (IMBH) in the mass gap between $130-250M_\odot$ which, unlike stellar black holes, cannot be formed by the collapse of a single star due to the phenomenon of pair production, which leads to the pair-instability supernova as the latest stage of the evolution of very massive stars [51]. They cannot be formed as supermassive black holes either, since their environments lack the super dense extreme conditions observed at the center of galaxies. The first (and only) observational evidence of an intermediate mass black hole in the mass gap was the gravitational wave event GW190521 [27, 28]. An extended reanalysis of this event has also been carried out by the UIB group [52], among others. This detection corresponds to the collision of two stellar black holes ($65M_\odot$ and $85M_\odot$), resulting in a $142M_\odot$ black hole, entering the IMBH pair-instability mass gap range.

2.2 Black hole Binaries

We can now consider binaries of general black holes, i.e. Kerr black holes. In this case, the parameter space will be composed by the two masses and spins, giving rise to eight dimensions, which will completely describe our problem if the orbit is circular. In case of having an eccentric orbit, then two more parameters are needed: the eccentricity and the orientation of the ellipse. Most of the current waveform models focus however on circular orbits, which turned out to be a good approximation [53]: eccentric orbits tend to circularize rapidly in the absence of other forces. Therefore, we will also keep this simplification in this project. It is convenient to introduce geometric units, setting $G = c = 1$. Since fundamental constants other than G and c are absent in vacuum general relativity we can furthermore choose $M = G = c = 1$, expressing the fact that in this case the mass M acts as a scale parameter. The parameter space of black hole binaries can then be parameterized by the mass ratio $q = m_1/m_2 \geq 1$ and the spin vectors of the two black holes.

Independently of the properties of the component masses, the evolution of a compact binary system is characterized by three distinctive phases. The following discussion is in fact also valid for any compact object binary, i.e. BNS, NSBH or BBH. Figure 2.2 shows the evolution of the first detection GW150914 [1]: a compact binary coalescence

of initial black hole masses 36^{+5}_{-4}M$\odot$ and 29^{+4}_{-4}M$_\odot$, which resulted in a final black hole of mass 62^{+4}_{-4}M$_\odot$ and hence, $3.0^{+0.5}_{-0.5}$M$_\odot$ were radiated in gravitational waves.

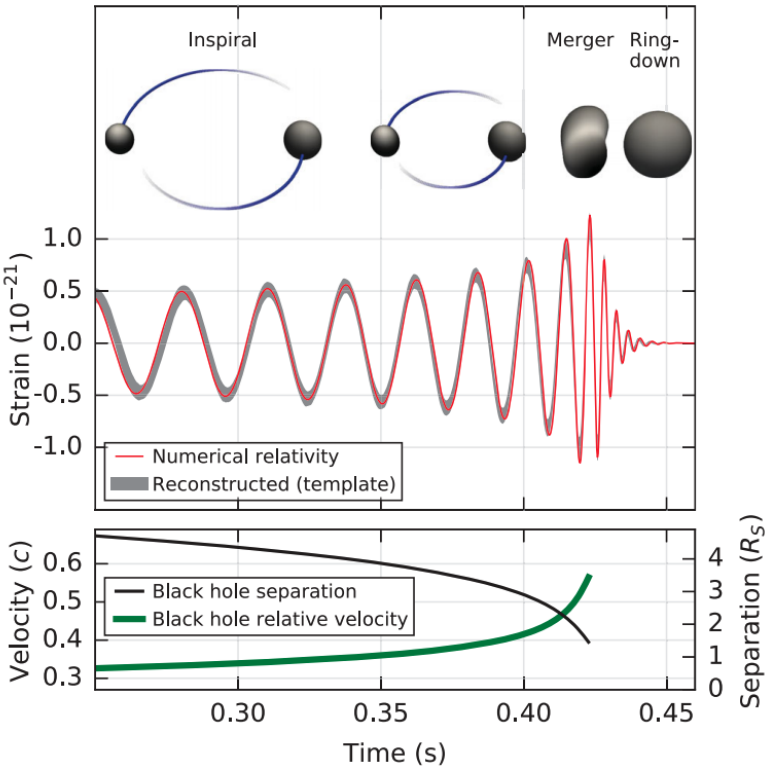

Figure 2.2: *Top*: Gravitational-wave strain amplitude, including the phases of the binary evolution. *Bottom*: Keplerian effective black hole separation in terms of the Schwarzschild radius R_s and the effective relative velocity given by the Post-Newtonian parameter v/c. Source: Results of the first ever detection GW150914 [1].

The inspiral is the first phase of the evolution, where the objects revolve around each other during a large period of time. During this phase, orbital energy of the system is carried away through the emission of gravitational waves, which leads to a tightening of the orbit. The decrease in the orbital separation translates into an increase in the orbital frequency and, therefore, in the (Keplerian) velocity $v = (GM\pi f)^{1/3}$ (see bottom plot in Figure 2.2). This provokes the emission of stronger gravitational waves, whose amplitude increases as the masses get closer, and hence a greater loss of energy which accelerates the approach between the compact objects. When the compact objects orbit fast enough and the signal frequency enters the frequency band of our detectors, then the strain may overcome the noise curves (see Figure 1.3.2) and the radiated waves can be detected. This process ends with the merger of the two components, which corresponds to the peak amplitude and the following ringdown of the remnant black hole. This last stage is characterized by the oscillation of the final object, which emits gravitational waves with a rapidly decaying amplitude until it settles down to the stationary solution: a Kerr black hole. In this last part of the evolution, the exponential decay of the amplitude quickly makes the signal undetectable. The binary evolution is then characterized by the amplitude of the gravitational waves emitted (see top plot in Figure 2.2).

Several techniques have been developed to provide an accurate description of the complete Inspiral-Merger-Ringdown description of compact binary coalescences. During

the slow evolution of the inspiral, one can assume some simplifications and rely on Newtonian physics up to a certain order in the parameter v^2/c^2, the so called post-Newtonian approximation [54]. This expansion will however break down when velocities come close to the speed of light i.e. during the last orbits and merger, where one needs to directly solve the EFEs numerically to find an accurate description of the signal. In Section 2.2.1 we will describe the usual decomposition used for the gravitational wave signal coming from binaries. Finally, Section 2.2.2 includes a brief overview about the different methods used during the Inspiral-Merger-Ringdown description of gravitational waves of compact binary systems.

2.2.1 Spherical harmonic decomposition

The gravitational wave strain h depends on an inertial time coordinate t, its position in the sky and also on the source parameters, which considering geometric units are $(q, \boldsymbol{\chi}_1, \boldsymbol{\chi}_2) \equiv \boldsymbol{\lambda}$. Introducing the standard spherical coordinate system, the sky position can be represented by the angles θ and ϕ, which are the standard polar coordinates on the unit sphere, and the distance r. At large distance (as is the case in astronomy), the strain is inversely proportional to the distance, i.e.

$$h(t, \mathbf{r}, \boldsymbol{\lambda}) = \frac{h_0(t, \hat{\mathbf{r}}, \boldsymbol{\lambda})}{r} + O(r^{-2}), \tag{2.2.1}$$

and one is only interested in the quantity h_0. Furthermore, the strain can be written in terms of the transverse-traceless polarizations introduced in Section 1.1, Eq. (1.1.16),

$$h(t, \mathbf{r}, \boldsymbol{\lambda}) = h_+(t, \mathbf{r}, \boldsymbol{\lambda}) - i h_\times(t, \mathbf{r}, \boldsymbol{\lambda}), \tag{2.2.2}$$

so the gravitational wave is completely described as a single complex quantity. Analogous to other radiation problems, the angular dependence can be described by spherical harmonics. The tensor strain can be expanded in terms of spin-weighted spherical harmonics (SWSHs) with spin weight $s = -2$ [55, 56],

$$h(t, \mathbf{r}, \boldsymbol{\lambda}) = \frac{1}{r} \sum_{l \geq 2, m=-l}^{m=l} h_{lm}(t, \boldsymbol{\lambda}) Y^{-2}_{lm}(\hat{\mathbf{r}}) = \frac{1}{r} \sum_{l,m} h_{lm}(t, \boldsymbol{\lambda}) Y^{-2}_{lm}(\theta, \phi). \tag{2.2.3}$$

Higher order terms are strongly suppressed, and for comparable mass systems only a handful of terms in Eq. (2.2.3) are required for current data analysis applications [57]. Indeed, a qualitatively good result for systems with equal masses and spins aligned to the orbital angular momentum (non-precessing systems) can be obtained only considering the dominant quadrupole modes, i.e. the $(l, m) = (2, \pm 2)$, which correspond to the direction of higher emission. For instance, the spherical harmonics for these modes are given by

$$Y^{-2}_{2,\pm 2} = \sqrt{\frac{5}{64\pi}} (1 \pm \cos(\theta))^2 e^{\pm 2i\phi}. \tag{2.2.4}$$

It is useful thus to discuss directly the modes $h_{lm}(t, \boldsymbol{\lambda})$ instead of the value of the strain in any particular direction. Indeed, this representation highly simplifies the problem, since one can represent the waveform in terms of a few time-dependent functions, instead of a single function that depends both on time and two angles. Each of these modes, which

take complex values, can now be described in terms of their amplitude $A(t, \boldsymbol{\lambda})$ and the phase $\Psi(t, \boldsymbol{\lambda})$, following the relation

$$h_{lm}(t, \boldsymbol{\lambda}) = A_{lm}(t, \boldsymbol{\lambda}) e^{i\Psi_{lm}(t, \boldsymbol{\lambda})}, \tag{2.2.5}$$

where A_{lm} and Ψ_{lm} can be taken as real functions. The phase derivative $\dot{\Psi}_{lm}$ is proportional to the frequency of the mode h_{lm}, which approximately corresponds to m times the orbital frequency of the binary. Modes with $m > 0$ have negative frequency and correspond to right-handed circularly polarized waves that are concentrated in the northern hemisphere with respect to the orbital plane. One the other hand, those modes with negative values of m will have positive frequency and following the same right-handed rule, are circularly polarized waves but concentrated in the southern hemisphere.

The spherical harmonic decomposition (2.2.3) is however not the most natural for the complete evolution of the binary. During the ringdown, the final black hole relaxes toward its stationary solution and the gravitational wave emission is dominated by a superposition of quasinormal modes (QNM) (see for instance [58]). During the QNM emission, the strain can be written as

$$h(t, \boldsymbol{\lambda}, \theta, \phi) \approx \sum_{l,m,n} a_{lmn}(t, \boldsymbol{\lambda}) {}_{-2}\mathcal{Y}_{lm}(\theta, \phi) e^{i(\omega_{lmn} t + \Phi_{lmn}(t, \boldsymbol{\lambda}))}, \tag{2.2.6}$$

where ${}_{-2}\mathcal{Y}_{lm}(\theta, \Phi)$ are the *spheroidal harmonics of spin weight* $s = -2$ [59, 60], $a_{lmn}(t, \boldsymbol{\lambda})$ and $\Phi_{lmn}(t, \boldsymbol{\lambda})$ are the amplitude and phase offsets, fitted to numerical relativity data and finally, the complex frequencies ω_{lmn} depend on the final black hole spin and mass, as can be seen in Figure 2.3. Their real and imaginary parts define the ringdown and damping frequencies:

$$\begin{aligned} f_{lm}^{\text{ring}}(M_{\text{f}}, \chi_{\text{f}}) &= \text{Re}(\omega_{lm})/2\pi \\ f_{lm}^{\text{damp}}(M_{\text{f}}, \chi_{\text{f}}) &= \text{Im}(\omega_{lm})/2\pi. \end{aligned} \tag{2.2.7}$$

Note that in the last Equation the index n denotes the different overtones, which for $n > 1$ are strongly damped. For this reason we will in the following only consider the dominant values, which imply setting $n = 1$.

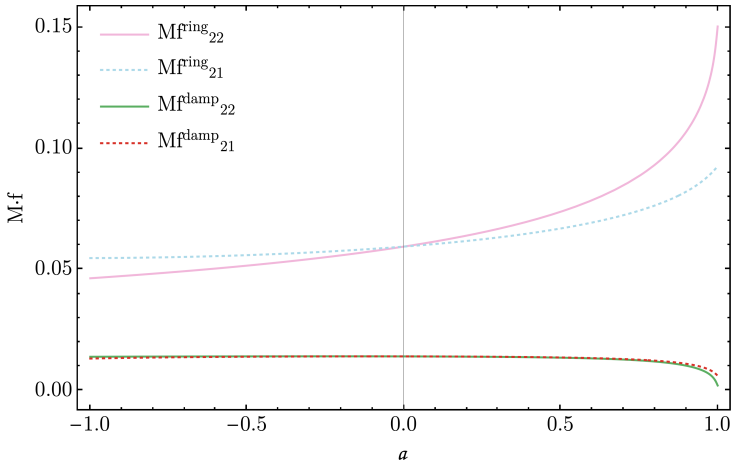

Figure 2.3: Ringdown and damping frequencies for a generic Kerr black hole with dimensionless spin a.

Therefore, during this last stage of the binary evolution, the spheroidal harmonics become a more natural basis because these are the functions related to the quasi normal

modes, although they do not form a complete basis that can be used during the complete evolution, whereas the spherical harmonics do. It is important to mention than the l and m indices that appear in the spheroidal harmonic decomposition (2.2.6) do not correspond to the ones of the spherical decomposition (2.2.3). We will refer to the quasinormal modes with $m > 0$ as *prograde ringdown modes* and those with $m < 0$, as *retrograde ringdown modes*. In the particular case where the spin vectors of both black holes are aligned to the orbital angular momentum, only the prograde modes will be excited, and again the signal will be circularly polarized. For a more particular case, however, both the prograde and retrograde modes will be excited and the correspondence between the spherical modes' frequencies and the ringdown frequencies will be more challenging. Further discussion on this topic can be found in Chapters 4 and 5.

Another effect of this new decomposition (2.2.6) is that it can result in a mode mixing for those modes that have approximately the same real part of the ringdown frequency ω_{lmn} when using the spherical harmonic decomposition [61–63].

2.2.2 Inspiral-Merger-Ringdown description

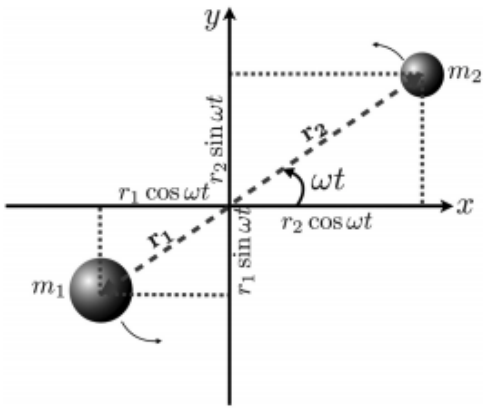

Figure 2.4: A two body system of masses m_1 and m_2 orbiting in the x-y plane. Credit: [64].

During the early inspiral of a binary system, analytical approximations can provide a good qualitative description of the gravitational wave signal, based on Kepler's third law and Einstein's quadrupole formula (Equation (1.1.27)). If we consider the system shown in Figure 2.4, we can calculate the reduced quadrupole tensor moment (1.1.26), which is given by

$$Q = \sum_{A\in[1,2]} \frac{m_A}{3} \begin{pmatrix} 2x_A^2 - y_A^2 & 3x_A y_A & 0 \\ 3x_A y_A & 2y_A^2 - x_A^2 & 0 \\ 0 & 0 & -r_A^2 \end{pmatrix}. \tag{2.2.8}$$

Taking into account the geometry included in Figure 2.4, assuming a circular orbit of separation r and orbital frequency ω (and hence $f_{\rm orb} = \frac{\omega}{2\pi}$), then it is straightforward to show that Q is given by

$$Q(t) = \frac{1}{2}\mu r^2 \begin{pmatrix} \cos(2\omega t) + 1/3 & \sin(2\omega t) & 0 \\ \sin(2\omega t) & 1/3 - \cos(2\omega t) & 0 \\ 0 & 0 & -2/3 \end{pmatrix}. \tag{2.2.9}$$

The radiation power emitted during the process can then be calculated using Eq. (1.1.28), leading to

$$L = \frac{\mathrm{d}}{\mathrm{d}t} E_{\rm GW} = \frac{32}{5}\frac{G}{c^5}\mu^2 r^4 \omega^6. \tag{2.2.10}$$

This power radiated comes from the orbital energy of the system $E_{\rm orb} = -\frac{GM\mu}{2r}$, so the following equality holds during the inspiral, where the approximations are valid:

$$L = -E_{\rm orb} = \frac{GM\mu}{2r^2}\dot{r}. \tag{2.2.11}$$

We can now make use of Kepler's third law, which establishes a relation between the radius of the orbit r and its orbital frequency, so $r^3 = GM/\omega^2$. Taking its derivative and substituting all the r's of Eq. (2.2.11), one can obtain a differential equation for the orbital frequency:

$$\dot{\omega}^3 = \left(\frac{96}{5}\right)^3 \frac{\omega^{11}}{c^{15}} G^5 \mu^3 M^2 = \left(\frac{96}{5}\right)^3 \frac{\omega^{11}}{c^{15}} (G\mathcal{M})^5, \tag{2.2.12}$$

where $\mathcal{M} = (\mu^3 M^2)^{1/5}$ is the chirp mass. Before solving this equation, which will give the relation between time and frequency, we can calculate the gravitational wave strain polarizations from the quadrupole moment (2.2.9) using the quadrupole formula (1.1.27) and setting the z-axis orthogonal to the x-y plane (for a textbook development see e.g. [37] ch. 4.1):

$$\begin{aligned} h_+(t) &= \frac{4G\mu\omega^2 r^2}{Rc^4} \frac{1+\cos^2(\theta)}{2} \cos(2\omega t + 2\phi), \\ h_\times(t) &= \frac{4G\mu\omega^2 r^2}{Rc^4} \cos(\theta) \sin(2\omega t + 2\phi), \end{aligned} \tag{2.2.13}$$

where r is the separation between both objects, R the distance to the system, η the reduced mass and ω the orbital frequency. The polarizations show that the emitted waves have a frequency of twice the orbital frequency, so we can define the frequency of the gravitational waves as $\omega_{\rm GW} = 2\omega$). Inserting this relation into Eq. (2.2.12) and solving the differential equation for $f_{\rm GW} = \frac{\omega_{\rm GW}}{2\pi}$ gives the evolution of the gravitational wave frequency in time:

$$\begin{aligned} f_{\rm GW}(t) &= \frac{1}{\pi} \left(\frac{5}{256(t_{\rm coal} - t)}\right)^{3/8} \left(\frac{G\mathcal{M}}{c^3}\right)^{-5/8}, \\ \tau(f) &= \frac{5}{256} (\pi f_{\rm GW})^{-8/3} \left(\frac{G\mathcal{M}}{c^3}\right)^{-5/3}, \end{aligned} \tag{2.2.14}$$

where $t_{\rm coal}$ is the coalescence time starting at a reference time and τ corresponds to the time until coalescence ($\tau = t_{\rm coal} - t$). These last expressions imply that the time during which the system is emitting gravitational waves that can be observed by our detectors depends on the masses of the compact objects involved. We now consider two equal mass systems, a neutron star binary of masses $M_{\rm NS} = 3M_\odot$ and a black hole binary of masses $M_{\rm BH} = 50M_\odot$ binary. The LIGO detector at design sensitivity starts its detectable frequency range at approximately 10 Hz, which, using Equation (2.2.14), implies that the times these binaries systems are emitting detectable waves are $\tau_{\rm BNS} \approx 15$ minutes and $\tau_{\rm BBH} \approx 8$ seconds. Hence, a signal coming from a black hole binary can last several seconds, but hundreds of seconds from a neutron star binary.

The numbers obtained from these approximations give good estimates, but the equations will be only valid during the early inspiral, and more expanded descriptions are needed to perform gravitational wave data analysis. During the late inspiral, a post-Newtonian (PN) expansion [54] of Equations 2.2.13 and 2.2.10 can further improve the accuracy of the description, including deviations in terms of an expansion in the parameter v^2/c^2. As the velocity of the binary increases, higher order expansions become desirable: current PN expressions are available at 3PN, i.e. $(v/c)^6$, or even 4PN order. This expansion will however break down when the velocity comes close to the speed of light, i.e. during the last orbits and merger. During this late stage of the binary evolution, perturbative methods cannot be used anymore, but the EFEs must be solved numerically instead. Hence, a complete description of the gravitational wave signal from binaries of compact objects became possible only after the breakthroughs in numerical simulations in 2005 [65–67].

Systematic errors in theoretical descriptions of WFs reduce their efficiency for detection and increases parameter bias for parameter estimation. In order to improve further the efficiency of the waveform models for gravitational wave data analysis, one might go beyond those waveforms for discrete points on the parameter space produced by numerical simulations. Catalogs can be built up using numerical relativity (NR) waveforms, which combined with theoretical models permit to develop accurate descriptions of the signal for wider regions of the parameter space. Initially, waveform models were based on modelling only the quadrupole modes, which are the dominant contributions of the spherical harmonic decomposition described in Eq. (2.2.3). These models achieve qualitatively good results for non-precessing systems, with mass ratio close to one and for moderate signal-to-noise ratios. The need to go beyond these approximations led to the incorporation of higher modes, unequal spins and the possibility higher mass ratios in upgraded models. Other effects have also been incorporated to the latest waveform models, such as misaligned spins or eccentricity. The effect of misaligned spins, which leads to a phenomenon known as *precession*, is discussed in detail in Chapter 3. Most of the models are calibrated to NR in order to obtain more reliable result for the late evolution of the binary. However, those effects such precession and eccentricity that increase the parameter space are more difficult to calibrate due to the high computational cost of those simulations. Hence, waveform developers have been using different approximations to deal with this particular cases in order to achieve more efficient models for data analysis.

Several methods have been proposed following these ideas, and three major families can be classified in this framework. The time domain effective-one-body (EOB) models [68–88] are based on a mapping between the general relativistic two-body problem into an effective one-body problem, i.e. the motion of a test particle in an effective metric. The method relies on a deformation of the Schwarzschild metric and introducing a non-perturbative method for re-summing the PN expansion of the equations of motion. Some of these models are also calibrated to numerical relativity, the so called EOB-NR, which are used for data analysis. Phenomenological models, on the other hand, are usually developed in the frequency domain, and constructed from closed expressions, giving rise to the IMRPhenom family [57, 89–100]. The IMRPhenomX family has been partially developed at the UIB, as well as the complete IMRPhenomT family, the first phenomenological model developed in the time domain [98–100]. These two families form the fourth generation of phenomenological waveform models. Finally, the surrogate waveform models (NRSurrogate [101–103]) take pre-computed NR waveforms and interpolate them in parameter space in order to quickly produce a waveform for any parameter values included in the interpolation. This way it can be evaluated much faster than a complete NR simulation and with the same accuracy if a sufficiently large set of waveforms are considered.

As previously mentioned, models can be constructed in the time or in the frequency domain. The time domain description is naturally related to the description of the binary system in terms of an initial value problem, which often simplifies the interpretation of the waveform in terms of the dynamics of the system. Frequency domain templates are however most natural to compute the scalar product with the detector data, whereas time domain waveforms need to be previously Fourier transformed. This operation does not necessarily imply a substantial increases of computational cost, but one needs to carefully window the data before the operation, which is difficult to achieve across the entire parameter space of waveforms, including different start frequencies or sampling parameters. A further inconvenience associated with time domain waveforms is that different spherical harmonic

modes have different frequencies at a given time: In a co-precessing frame a (l, m) mode will have a frequency of approximately m times the orbital frequency. Thus, at the time when the mode with highest $|m|$ that has a sufficiently large amplitude to give a significant contribution to the signal enters the sensitive detector band at a given frequency (say 20 Hz), modes with lower $|m|$ will have not yet entered the sensitive band of the detector. The length of the waveform that has to be computed thus depends on the "highest" modes used. As can be seen from Eq. (2.2.14), to leading post-Newtonian order the length of the waveform Δt in time scales as

$$\Delta t \approx f_{start}^{-8/3}, \tag{2.2.15}$$

as a function of the start frequency f_{start}. Including $|m| = 4$ modes in addition to the dominant $|m| = 2$ modes thus requires a waveform that is longer by a factor of 6.35, which typically leads to a comparable increase in computational cost.

Frequency domain models are thus highly desirable from a data analysis point of view. However, due to "smearing out" the time domain signal with the integral that corresponds to the Fourier transform often complicates the interpretation of the waveform morphology. A typical example is the quasinormal mode emission, where the oscillation frequency and exponential damping time are more easily identified in the time domain, and in particular describing the precessing ringdown is much simpler in this domain. In consequence, while for non-precessing waveforms the accuracy of frequency domain waveform models is at least as high es for time domain waveforms [96], in the precessing sector it is still inferior to time domain models.

These ideas motivate the improvement of current frequency domain models for the large part of the parameter space of black hole binaries where the component spins are misaligned. Current frequency domain models usually rely on the stationary phase approximation (SPA, described in Sec. 4.1), to convert closed form expressions for precessing waveforms in the time domain into closed form expressions in the frequency domain. The SPA is however not appropriate for the merger/ringdown phases of the binary. Due to the large dimensionality of the parameter space of precessing systems, covering this region of parameter space with NR simulations is computationally very expensive, which complicates the NR calibration for precessing waveform models. Hence, waveform developers have been trying to surpass the SPA without relying on NR in order to keep with simple and fast models. Different approaches have thus been considered to deal with precession in the frequency domain, and in this project we will focus on the one described in Ref. [8]. This implementation and its results will address and give some answers to the current status of precession in the frequency domain and its following development steps, in concrete for the phenomenological family IMRPhenomX and its precessing model IMRPhenomXPHM.

CHAPTER 3

Gravitational Waves from Precessing Systems

3.1 Non-precessing Binaries

For binaries composed of Kerr black holes, i.e. black holes which are rotating, the orientation of the spin vectors will determine the behaviour of the waveform. Black hole binaries with the spin vectors $(\mathbf{S_1}, \mathbf{S_2})$ orthogonal to the orbital plane, or equivalently, parallel to the orbital angular momentum $(\mathbf{L})$, are referred to as *non-precessing binaries*. In this particular case, there exists an equatorial symmetry of the spacetime with respect to the orbital plane. This symmetry is preserved in time, and so are as the spin directions and the orbital plane itself. The parameter space for these systems is then four dimensional, with two degrees of freedom needed in order to describe the spins and the other two for the masses. It can be however reduced to three dimensions when recalling that the total mass acts as a scale parameter, and introducing the mass ratio $q = \frac{m_1}{m_2} \geq 1$. The loss of the orbital angular momentum $\mathbf{L}$ will be completely due to the emission of gravitational waves, varying on the inspiral timescale. Moreover, the change of total angular momentum $\mathbf{J} = \mathbf{L} + \mathbf{S_1} + \mathbf{S_2}$ will be determined by the emission of gravitational waves. In this case, the standard spherical harmonic decomposition (2.2.3) and the phase-amplitude representation of the modes (2.2.5) simplifies the mode descriptions, since the variation of the phase and amplitude can be approximated as simple functions.

For non-precessing systems, the energy is predominantly emitted in the direction of the orbital angular momentum $\mathbf{L}$, which points orthogonal to the orbital plane. This can be seen using the first-order calculations developed in the previous section based on Newtonian orbital dynamics and the Einstein's quadrupole formula (see Equation (1.1.17)). It is then natural to define the z-axis of the inertial frame in the direction of $\mathbf{L}$ due to the symmetry of these systems. In this frame, it turns out that modes with lower values of $|m|$ have weaker amplitude, which shows the natural hierarchy of mode amplitudes. The $(l = 2, m = \pm 2)$ spherical harmonics of the wave are the dominant modes, then the modes $(l, m = \pm 1)$ vanish if the two black holes can be exchanged by symmetry and $m = 0$ is a non-oscillating mode related to memory effects, see e.g. [104]. Other features of non-precessing systems also yield simplifications. For instance, the system is invariant under reflection across the orbital plane or the plane x-y in our set of coordinates, which reads as

$$h_{lm}(t) = (-1)^l (h_{l-m}(t))^*, \tag{3.1.1}$$

where h^* denotes the complex conjugate. One can find a deduction in Appendix C in

Ref. [105]. Hence, this property implies that we can focus only on the modes with $m > 0$, and compute the ones with $m < 0$ from Eq. 3.1.1.

3.2 Precessing Binaries

The more general case is however much more challenging. Black hole binary systems with one or both components having spins not orthogonal to the orbital plane (misaligned spins) are referred to as *precessing systems*. The number of degrees of freedom increases notably and eight parameters are needed to characterize the system (six for the spins and two for the masses), or seven when considering the mass ratio. Moreover, all the symmetries present for non-precessing systems are broken, and the orbital plane is no longer preserved, but it rather shows a complicated precession motion, as do the spins. In this case, there is no natural z-axis because all the modes with the same value of l are mixed. This implies that there is no natural amplitude hierarchy of the modes as it happened for non-precessing systems and hence, the symmetry property in Equation (3.1.1) does not hold for precessing systems.

Precessing systems are thus characterized by the spin vectors of one or both components of the binary not being aligned with the orbital angular momentum, or equivalently, not being orthogonal to the orbital plane. This provokes a precession of $\mathbf{S}(t)$ and $\mathbf{L}(t)$ in time, and hence, the orbital plane itself shows a time-dependent variation. An example of a precessing binary motion can be seen in Figure 3.1. The time variation of the orbital plane leads to an amplitude modulation of the waveform, since gravitational waves are preferably radiated in the direction orthogonal to this plane. This modulation then complicates the production of analytic precessing binary waveform models. As we will see below, the GW signal can be greatly simplified in an appropriate non-inertial frame.

3.2.1 Post-Newtonian description of precession

As mentioned in Chapter 2, the post-Newtonian approximation [54] permits to describe the evolution of binary systems in terms of a point particle Hamiltonian and in fact, the spins of the black holes play an essential role in the orbital dynamics and gravitational wave emission. The spin effects can be split into two contributions at highest order, the spin-orbit (SO), which is the dominant effect, and the spin-spin (SS) interaction (see e.g. [106] or [5] for a further discussion of these two terms). For a qualitative description of precession one can focus on the leading order spin-orbit Hamiltonian,

$$H_{SO} = 2\frac{\mathbf{S_{eff}} \cdot \mathbf{L}}{R^3}, \tag{3.2.1}$$

where R is the separation between both black holes and the effective spin $\mathbf{S_{eff}}$ is defined as

$$\mathbf{S_{eff}} = \left(1 + \frac{3}{4}\frac{m_2}{m_1}\mathbf{S_1}\right) + \left(1 + \frac{3}{4}\frac{m_1}{m_2}\mathbf{S_2}\right), \tag{3.2.2}$$

where $S_i = m_i^2 \chi_i$ are the dimensionful spins and χ_i, the dimensionless component spins. Equation (3.2.1) shows that the potential energy depends on the aligned spin components, i.e. the components parallel to the orbital angular momentum. The sign of the scalar product will determine the type of interaction between the bodies, either attractive if $\mathbf{S_{eff}}$ and $\mathbf{L}$ are anti-aligned ($\mathbf{S_{eff}} \cdot \mathbf{L} < 0$) or repulsive if they are aligned ($\mathbf{S_{eff}} \cdot \mathbf{L} > 0$). In

case of attractive interaction, then the objects will inspiral together faster, emitting less gravitational waves, whereas for aligned spins, the objects will revolve each other during more time, and hence, will emit more gravitational radiation.

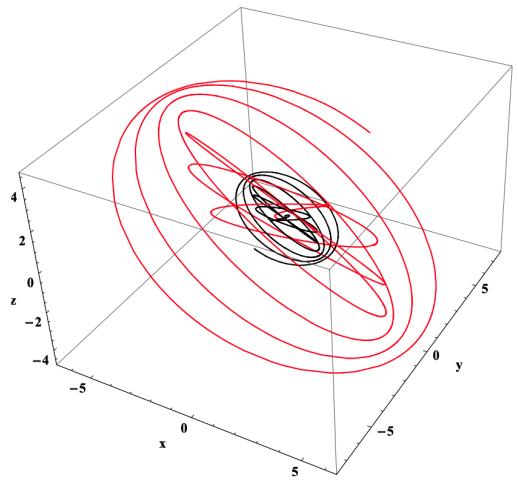

Figure 3.1: Motion of a precessing black hole binary of with mass ratio $q = 3$. The red line corresponds to the motion of the smaller black hole and the black one of the larger. Credit: [6].

The Post-Newtonian approximation for the spin-orbit interaction also permits to derive the time evolution of the black hole total spin

$$\dot{\mathbf{S}}_{\mathbf{SO}} = -\frac{2}{R^3}\mathbf{S}_{\mathbf{eff}} \times \mathbf{L}. \tag{3.2.3}$$

This last equation manifests the effects that have been discussed for non-precessing and precessing systems: if the black hole spins are parallel to the orbital angular momentum and the time evolution of the total spin vanishes, then the total spin is a preserved quantity up to leading PN order. On the other hand, the orthogonal spin components of a precessing binary lead to a non vanishing cross product with the orbital angular momentum, and hence the total spin presents a variation in time. The magnitude of the precession depends however both on the magnitude of the total spin $\mathbf{S}$ and the relative orientation of $\mathbf{S}$ and $\mathbf{L}$, so if any of these is small in comparison with $\mathbf{L}$, then the modulations can be neglected.

The orbital angular momentum can also be split to leading post-Newtonian order as [106]

$$\mathbf{L} = \mathbf{L_N} + \mathbf{L_{PN}} + \mathbf{L_{SO}}, \tag{3.2.4}$$

where $\mathbf{L_N} = \mu(\mathbf{r}\times\mathbf{v})$ is the Newtonian orbital angular momentum, and the other quantities are

$$\begin{aligned}
\mathbf{L_{PN}} &= \mathbf{L_N}\left[\frac{1}{2}v^2(1-3\eta) + (3+\eta)\frac{M}{r}\right], \\
\mathbf{L_{SO}} &= \frac{\mu}{M}\left[\frac{M}{r}\mathbf{n}\times\left(\mathbf{n}\times\left(3\mathbf{S} + \delta M\left(\frac{\mathbf{S_1}}{M_2} - \frac{\mathbf{S_2}}{M_1}\right)\right)\right) - \frac{1}{2}\mathbf{v}\times\left(\mathbf{S} + \delta M\left(\frac{\mathbf{S_1}}{M_2} - \frac{\mathbf{S_2}}{M_1}\right)\right)\right],
\end{aligned} \tag{3.2.5}$$

where $\delta = \sqrt{1-4\eta}$ and $\eta = q/(1+q^2)$ is the symmetric mass ratio. The evolution of the orbital angular momentum up to 2PN order is [107]

$$\begin{aligned}
\dot{\mathbf{L}} = &\left[\left(2 + \frac{3}{2}q\right) - \frac{3}{2}\frac{v}{\eta}\left[(\mathbf{S_2} + q\mathbf{S_1})\cdot\hat{\mathbf{L}}\right]\right]v^6(\mathbf{S_1}\times\hat{\mathbf{L}}) \\
&+ \left[\left(2 + \frac{3}{2q}\right) - \frac{3}{2}\frac{v}{\eta}\left[(\mathbf{S_1} + \frac{1}{q}\mathbf{S_2})\cdot\hat{\mathbf{L}}\right]\right]v^6(\mathbf{S_2}\times\hat{\mathbf{L}}) \\
&+ \mathcal{O}(v^7).
\end{aligned} \tag{3.2.6}$$

These post-Newtonian terms are introduced into the equations of motion, which has significant implications on the binary evolution and thus in the waveform itself. The effects in the binary evolution can be seen in Figure 3.1.

The description of precessing waveform models has proven difficult: the incorporation of misaligned spins includes new terms in the PN equations at highest order, which makes it difficult to solve them analytically to obtain phenomenological descriptions. Moreover, the large dimensionality of the problem (7 degrees of freedom instead of 3 in non-precessing binaries) makes it more challenging to sample in order to perform numerical relativity simulations, which are computationally very expensive. The previous post-Newtonian results have shown that the orthogonal components of the spins affect neither the emission of gravitational waves nor the inspiral evolution (3.2.1), but only contribute to the precession of the total spin (3.2.3) and the orbital angular momentum (3.2.6). This feature can be exploited in order to look for an efficient way to describe precessing waveforms, together with the natural separation among the different timescales present in the evolution of precessing systems. The fact that the acceleration due to orbital motion dominates in front of the precessing motion permits to consider that the power radiated due to precession can be neglected in the inspiral. Hence, this permits to work in a coordinate time-dependent frame that is adapted to the precessing motion and rotated relative to a fixed inertial frame, so the resulting "co-precessing" waveform is similar to the one produced by the corresponding aligned spin binary system [6].

3.3 "Twisting up" procedure

Non-precessing systems are characterized by two time scales: the time scale of the orbital motion, which can be considered approximately circular, and also the inspiral time scale of the radial motion, which is much slower. Due to the significant difference in the timescales, the radiation of gravitational waves is mostly due to the orbital motion. When considering misaligned systems, there is the new time scale mentioned before, the precessing time scale, which lies in between the other two. Nevertheless, it is much slower than the orbital time scale, at least during the inspiral, so this effect also contributes relatively little to the loss of energy due to gravitational wave emission. Indeed, a good approximation during the inspiral can be obtained by neglecting the power emitted due to the radial motion, and one can thus assume that the inspiral rate of a precessing system can be approximated by its analogue aligned spin system. Rather, the main effect is the amplitude and phase modulation, which can be determined by considering an approximate map between precessing and non-precessing systems [6]: in a non-inertial frame which co-rotates with the orbital plane, the resulting waveform should look similar to a non-precessing one. Then, the precessing waveform can be obtained mapping a non-precessing one, procedure commonly referred to as "twisting up" the non-precessing signal [108].

It turns out [6] that the modes in the co-precessing frame, the "co-precessing" modes, show very similar features compared to the ones of a non-precessing waveform, such as the reflection across the orbital plane (3.1.1). The time-dependent rotation between the co-precessing frame and the inertial frame in which the data analysis is performed can be computed from the post-Newtonian approximations [108]. This has given rise to several phenomenological waveform models for precessing waveforms, which are now standard tools in gravitational wave astronomy. All these models follow the same idea: to perform a rotation of an appropriate non-precessing waveform into the inertial frame in which the data is analyzed. The time dependent rotation is usually described by the three Euler angles (EA), which are commonly obtained from either the direct numerical solution of the post-Newtonian equations or approximations in terms of analytic solutions, using

orbital averaging [109, 110] or the multiple scale analysis (MSA) [111]. In order to find the suitable “co-precessing frame” [6] in which to describe the waveform initially, one wants to maximize the amplitudes of the dominant modes of non-precessing systems, the $(l, m) = (2, \pm 2)$ modes, so-called “quadrupole modes”. This time-dependent frame, usually referred to as “quadrupole aligned frame”, has a non-static basis in which one needs to decompose the spherical harmonics of spin $s = -2$ in which the gravitational wave signal is decomposed (Equation (2.2.3)). This frame thus tracks the direction of the maximal gravitational radiation emission, which is orthogonal to the orbital plane. This direction is however not exactly the one of the orbital angular momentum as it happens for non-precessing systems, but it has turned out to be a good approximation in most cases.

Fixing the radiation axis however does not completely fix the frame, but there are ambiguities in rotations about that axis. In order to fix this freedom, Ref. [112] proposes the *minimal rotation condition*, so the frame becomes invariant under fixed rotations of the inertial frame. The fact that there is no preferred frame when dealing with precessing binaries implies that the numerical simulations might be presented in different frames. This condition then becomes indispensable when comparing gravitational waves from precessing binaries. In terms of the Euler angles, the minimal rotation condition reads as Equation (3.3.7). The effects of imposing this condition can be seen in Figure 3.2.

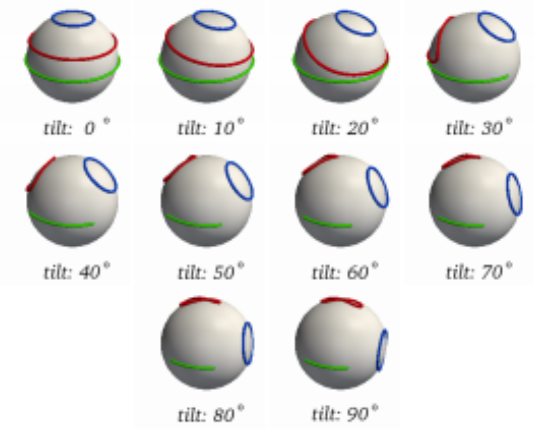

3.2.1: Rotation histories when imposing $\gamma = 0$.

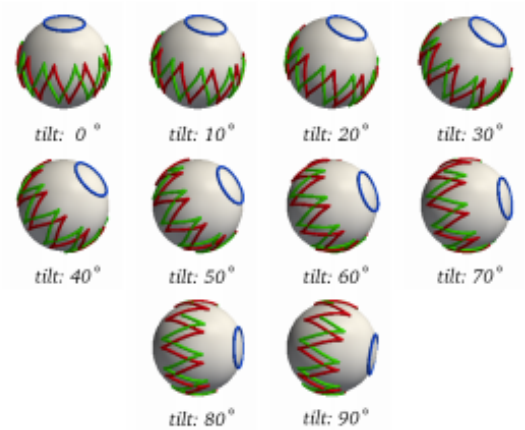

3.2.2: Rotation histories when imposing the minimal rotation condition.

Figure 3.2: Paths of the tips of the inertial axis x, y, z in red, blue and green respectively, when the radiation axis z is tilted the amount specified in the plot, when different conditions for γ are considered. Plots recovered from [112].

Figure 3.2 shows that rotation histories change considerably if a random choice of γ is considered, whereas the minimal rotation condition ensures that they are essentially invariant under fixed rotations of the inertial frame (see Section V B in [112]). The higher-mode amplitudes produced by the method are also consistent with those of non-precessing systems, which implies that the waveform is simplified, facilitating comparisons between analytic and numerical simulations.

The method thus relies on the definition of a time-dependent rotation between the non-inertial z-axis of the co-precessing and the one of the inertial frame. If we consider

the spherical harmonic decomposition of Equation (2.2.3) in the co-precessing frame, we need to define a new basis $Y^s_{lm}(\theta', \phi')$ for the rotated system at each moment in time (with θ' and ϕ' being the rotated coordinates). One then needs to find the spherical harmonic modes, whose complexity will greatly depend on the definition of the inertial frame chosen. Hence, even though there is no preferred (inertial) frame for precessing systems, it is one of the main keys in order to simplify the waveform. The spherical harmonic decomposition of the modes, Equation (2.2.3), also transforms simply under rotations, which is an essential feature to perform the procedure. Indeed, once the co-precessing modes $h^{\rm cop}_{lm'}$ are found, the modes in the inertial frame $h^{\rm I}_{lm}$ can be straightforwardly obtained as (as well as the inverse rotation)

$$\begin{aligned} h^{\rm I}_{lm}(t, \boldsymbol{\lambda}) &= \sum_{m'=-l}^{l} h^{\rm cop}_{lm'}(t, \boldsymbol{\lambda}) \mathcal{D}^{l}_{mm'}(\mathbf{R}(t)), \\ h^{\rm cop}_{lm'}(t, \boldsymbol{\lambda}) &= \sum_{m=-l}^{l} h^{\rm I}_{lm}(t, \boldsymbol{\lambda}) \mathcal{D}^{l*}_{mm'}(\mathbf{R}(t)), \end{aligned} \tag{3.3.1}$$

where $\mathcal{D}^{l}_{mm'}$ are the Wigner matrices and $\mathbf{R}$, the time-dependent rotation which transforms the co-precessing basis into the inertial one.

A variety of phenomenological waveform models for precessing waveforms have arisen from the fact that the twisting up procedure can be performed using post-Newtonian expansions, starting with the PhenomP model developed in Ref. [108]. These models have become essential tools in gravitational wave data analysis due to their computational efficiency, their capability to cover a large portion of the parameter space, and their simplicity, which has lead to robust code implementations.

The original PhenomP model [108] was based on the second phenomenological model for aligned spin waveforms, PhenomC [113] (PhenomA did not model spins and PhenomB was the first phenomenological model treating spins). An update, PhenomPv2 [114], adapted the model to the significantly more accurate PhenomD [89, 90] model for the co-precessing waveforms, and this version of the model has been used to analyse the first detection in 2015 [1], and has been routinely employed by the LIGO-Virgo collaboration to analyze events in the first three observation runs [2, 3]. More recently the fourth generation of aligned-spin phenomenological waveform models has been developed, IMRPhenomXHM [95, 96, 115], and based on this underlying non-precessing model, the latest version of a frequency domain precessing model, IMRPhenomXPHM [97]. The next Chapter will deal with the properties and limitations of the precessing models in the frequency domain, as well as the approach proposed by Marsat and Baker [8], which has been implemented in this project. There are also time domain models which follow the same procedure. For instance, the PhenomT family, developed by the UIB group, includes the IMRPhenomTPHM model [99, 100], built on the non-precessing model IMRPhenomTHM [98, 99]. These models have been implemented in the open source LIGO Algorithm Library (LAL) [116].

We will now proceed to describe in Subsection 3.3.1 the main differences between the co-precessing modes and the aligned-spin ones, and the limitations of the approximation. We will then introduce in Subsection 3.3.2 the main description used to perform the rotation of the co-precessing modes into the inertial modes, which is based on the Euler angles as a set of coordinates for $\mathbb{SO}(3)$. Finally, in Subsection 3.3.3 we will briefly discuss which are the natural frames used in the procedure, both the inertial and the definition of the co-precessing frame.

3.3.1 Co-precessing modes

The twisting-up procedure is based on the timescale separation of the orbital motion rate and the precession timescale. The fact that the orbital motion is much faster than the precession implies that this last effect does not contribute much to the radiation of gravitational waves. One can therefore assume that the radiated energy and angular momentum orthogonal to the orbital plane are identical to the non-precessing values. Indeed, NR simulations of precessing systems show that the final mass has only a weak dependence on precession (see for instance [117]) when comparing the results with fits of non-precessing systems. The previous argument is what gives rise to the main approximation of the twisting up procedure, which establishes that the spherical harmonic modes of the precessing waveform in the co-precessing frame $h^{\rm cop}_{lm}$ are approximately those generated by the aligned-spin system $h^{\rm AS}_{lm}$ (in the $\mathbf{L_0}$ frame, explained in Subsection 3.3.3)

$$h^{\rm cop}_{lm}(t, \boldsymbol{\lambda}) \approx h^{\rm AS}_{lm}(t, \boldsymbol{\lambda}). \tag{3.3.2}$$

One key aspect, which is not captured by this correspondence, is that the reflection across the orbital plane (3.1.1), which is valid for the aligned-spin modes, is no longer true for the co-precessing modes. This is however neglected in the current models, which assume in general that

$$h^{\rm cop}_{l-m}(t) = (-1)^l h^{\rm cop*}_{lm}(t). \tag{3.3.3}$$

This property can be translated to the Fourier domain applying the relation between Fourier transforms $\tilde{x^*}(f) = \tilde{x}(-f)^*$:

$$\tilde{h}^{\rm cop}_{l-m}(f) = (-1)^l \tilde{h}_{lm}(-f)^{\rm cop*}. \tag{3.3.4}$$

An additional simplification assumes that the co-precessing modes, as it happens for aligned spin waveforms, only have support for one side of the spectrum, which in our Fourier transform conventions (See Appendix A) reads

$$\begin{aligned} \tilde{h}^{\rm cop}_{lm}(f < 0) \approx 0 \text{ for } m < 0, \\ \tilde{h}^{\rm cop}_{lm}(f > 0) \approx 0 \text{ for } m > 0. \end{aligned} \tag{3.3.5}$$

Moreover, one can additionally assume that $\tilde{h}_{l0}(f) \approx 0$. Further discussion about the approximations performed in the twisting up procedure can be found in [118].

The main difference between the aligned-spin waveform and the co-precessing one is the final spin of the state. When considering precession, there is an addition of the individual spins and angular momentum which leads to a final spin state that differs from the non-precessing description. In Figure 2.3 we have seen that the quasi-normal mode emission during the ringdown depends both on the final mass and the final spin of the black hole remnant. Even though the final mass can be considered the same for precessing or non-precessing systems due to the difference of time scales, this approximate equality does not occur for the final spin. In order to obtain the co-precessing waveform, one cannot directly use the aligned-spin one, but needs to modify the ringdown region to account for the final spin of the precessing systems. Unlike for the final mass, there is no analytic expression to compute the final spin for precessing systems, so different approximations are used. A surrogate model for the final spin has been described in [117], which can be used for a limited range of mass ratios and black hole spins. A simpler estimate, but covering a larger parameter space, is the one used for the phenomenological

models IMRPhenomXPHM [97] and IMRPhenomTPHM [100]. This approach, which is described in Section IV.D in [97] and will be introduced in Section 4.2, is based on basic geometric arguments and the assumptions underlying the twisting-up. The main benefit of this simple approach is that it does not compromise the simplicity and wide application range of the phenomenological models.

3.3.2 Euler angle description

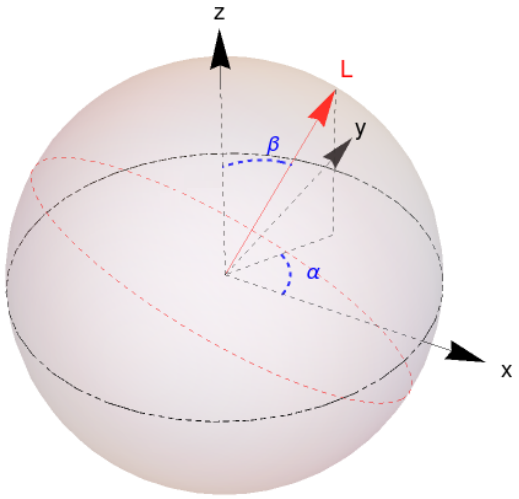

Figure 3.3: Definition of the Euler angles.

The Euler angles are the usual set of coordinates used to perform the rotation between the two frames characterized by the basis (x, y, z) and (x', y', z'). These three angles form one set of coordinates for the group of rotations about the origin, the so-called $\mathbb{SO}(3)$. The rotations in this set of coordinates are given by orthogonal 3×3 matrices, which depend on the three angles, with positive unit determinant. The group operation is the composition of rotations, which in terms of the Euler angles consists in matrix products. In this project we use the z_1-y'-z_2'' convention (intrinsic rotations), which corresponds to a first rotation of the angle α about the z-axis, a second rotation about the new y'-axis of the angle β and a third rotation of the angle γ around the z''-axis, where each $'$ denotes a change of coordinates. This is in fact equivalent to rotations in the opposite order about the initial axes, which remain fixed in this case: z_2-y-z_1. These are called extrinsic rotations. The convention used determines the axes evolution: in Figure 3.2.1 the y-axis is forced to remain on the x-y plane, whereas for a different choice of convention, such as the z-x-z used in e.g. [6], it would have been the x-axis. The first two Euler angles α and β are determined by construction (see Figure 3.3) and in the inertial frame $\{x, y, z\}$, they can be expressed as

$$\begin{aligned} \alpha &= \arctan(L_y, L_x) = \arctan \frac{L_x}{L_y}, \\ \cos\beta &= \mathbf{z} \cdot \mathbf{L} = L_z. \end{aligned} \tag{3.3.6}$$

The third angle is determined by imposing the minimal rotation condition [112] explained above in Figure 3.2:

$$\dot{\gamma} = -\dot{\alpha}\cos\beta. \tag{3.3.7}$$

Since this last equation only determines the derivative of γ, there exists a freedom in its initial value. Hence, one can choose to set $\gamma = 0$ at the reference time or frequency, which are related at lowest order by Equation (2.2.14).

The rotation needed to obtain the inertial modes from the co-precessing ones is specified in terms of the Wigner matrices [119], which can be expressed in terms of the Euler angles as a convenient set of coordinates. We can rewrite now Equation (3.3.1) in terms of these

angles:

$$
\begin{aligned}
h^{\rm I}_{lm}(t,\boldsymbol{\lambda}) &= \sum_{m'=-l}^{l} h^{\rm cop}_{lm'}(t,\boldsymbol{\lambda})\mathcal{D}^{l}_{mm'}(\alpha,\beta,\gamma),\\
h^{\rm cop}_{lm'}(t,\boldsymbol{\lambda}) &= \sum_{m=-l}^{l} h^{\rm I}_{lm}(t,\boldsymbol{\lambda})\mathcal{D}^{l*}_{mm'}(\alpha,\beta,\gamma),
\end{aligned}
\tag{3.3.8}
$$

With this last expression one can obtain the waveform associated to a precessing binary system from the co-precessing modes, which show approximately the feature in Eqs. (3.1.1) due to their similarity with those produced by a non-precessing system.

Explicit expressions for the Wigner matrices and their derivation can be found in [119], which in our convention is given by

$$
\begin{aligned}
\mathcal{D}^{l}_{mm'}(\alpha,\beta,\gamma) = &\sum_{k=\max[0,m-m']}^{\min[l+m,l-m']} \sqrt{(l+m)!(l-m)!(l+m')!(l-m')!}\\
&\times \frac{(-1)^k e^{i(m'\gamma+m\alpha)}}{k!(l+m-k)!(m'-m+k)!(l-m'-k)!}\left(\sin\frac{\beta}{2}\right)^{2k+m'-m}\left(\cos\frac{\beta}{2}\right)^{2l-2k-m'+m} =\\
&= e^{i(m'\gamma+m\alpha)} d^{l}_{mm'}(\beta),
\end{aligned}
\tag{3.3.9}
$$

where $d^{l}_{mm'}$ are the elements of Wigner's small d-matrix. These elements are real expansions of sin and cos functions of the angle β, following Equation (3.3.9). Some of the symmetries this matrix exhibits are

$$
d^{l}_{-m-m'}(\beta) = (-1)^{m-m'} d^{l}_{mm'}(\beta), \tag{3.3.10}
$$

$$
d^{l}_{mm'}(\beta) = (-1)^{m+m'} d^{l}_{m'm}(\beta), \tag{3.3.11}
$$

$$
d^{l}_{mm'}(\beta) = d^{l}_{m'm}(-\beta). \tag{3.3.12}
$$

We now provide some explicit expressions for the matrix elements that have been used in this project:

$$
\begin{aligned}
d^{2}_{22} &= \cos^4\frac{\beta}{2},\\
d^{2}_{12} &= 2\cos^3\frac{\beta}{2}\sin\frac{\beta}{2},\\
d^{2}_{02} &= \sqrt{6}\cos^2\frac{\beta}{2}\sin^2\frac{\beta}{2}.
\end{aligned}
$$

The Euler angles that perform the rotation to the inertial frame can be computed in many different ways. Focusing on the main idea of the twisting up procedure, the Euler angles can be computed by directly tracking the direction of maximum radiation emission [7]- this method is known as *quadrupole alignment*. These angles are thus computed directly from the waveform, and are obtained via geometric approaches. This method is useful to obtain the angles from a NR simulation, as it will be done in Section 5.2. For phenomenological waveform models in particular, this method is not optimal and analytical approximations are considered in order to improve computational efficiency. For waveform modelling it is then interesting to model these angles across the physical parameter space. We will now introduce the three descriptions that have been tested in this project to obtain the evolution of the three Euler angles.

3.3.2.1 Numerical evolution of the spin equations

As a first description of the Euler angle evolution, one could solve directly the orbital angular momentum evolution in PN theory (3.2.6) up to the desired order, together with the PN evolution of the individual black hole spins

$$\begin{aligned} \frac{d\mathbf{S}_1}{dt} &= \mathbf{\Omega}_1(v(t), q, \mathbf{S}_1, \mathbf{S}_2) \times \mathbf{S}_1, \\ \frac{d\mathbf{S}_2}{dt} &= \mathbf{\Omega}_1(v(t), q, \mathbf{S}_1, \mathbf{S}_2) \times \mathbf{S}_2. \end{aligned} \tag{3.3.13}$$

TOne can demonstrate from the post-Newtonian evolution equations at second PN order that the total angular momentum is preserved if the loss of energy due to gravitational radiation is neglected [106]. One can use this property in order to simplify the numerical resolution of the equations, since they are subject to the constraint

$$\dot{\mathbf{L}} = \dot{\mathbf{S}}_1 - \dot{\mathbf{S}}_2. \tag{3.3.14}$$

This approximation will hold until shortly before merger, since the inspiral timescale is much greater than the other timescales of the evolution. While this distribution of timescales holds, Eq. (3.3.14) only changes slowly due to the radiation reaction, which varies the "opening angle" between $\mathbf{J}$ and $\mathbf{L}$. Solving the equations (3.2.6) and (3.3.13) permits to determine the evolution of $\mathbf{L}(t)$, so one can obtain the Euler angle evolution needed to perform the twisting up from equations (3.3.6) and (3.3.7).

3.3.2.2 Next-to-next-to-leading order effective single spin

The next-to-next-to-leading order effective spin approximation [109, 110] introduces the triad $\mathbf{n}, \mathbf{L}, \boldsymbol{\lambda}$, being $\mathbf{n}$ the unit separation vector between the black holes and $\boldsymbol{\lambda}$ is defined such that it verifies $\boldsymbol{\lambda} = \mathbf{L} \times \mathbf{n}$. This approximation assumes only one spinning black hole (the larger one), so in our conventions where $m_1 > m_2$, then $\mathbf{S}_2 = 0$. The Euler angle evolution equations are then given by [97]

$$\begin{aligned} \dot{\alpha} &= -\frac{\bar{\omega}}{\sin\beta} \frac{J_n}{\sqrt{J_n^2 + J_\lambda^2}}, \\ \dot{\beta} &= \frac{J_\lambda}{\sqrt{J_n^2 + J_\lambda^2}}, \end{aligned} \tag{3.3.15}$$

where $\bar{\omega}$ is the precession frequency of the orbital plane, defined as $\dot{\mathbf{L}} = -\bar{\omega}\boldsymbol{\lambda}$, $\dot{\gamma}$ is given by the minimal rotation condition (3.3.7) and $J_{n,\lambda}$ are the components of the total angular momentum $\mathbf{J} = \mathbf{L} + \mathbf{S_1}$. Equations (3.3.15) and (3.3.7) are then solved next-to-next-to-leading order in the spin-orbit coupling [109], providing the time-dependent evolution of the three Euler angles. In this case, the spin degrees of freedom are included in an effective spin parameter

$$\chi_{\text{eff}} = \frac{m_1\chi_{1,L} + m_2\chi_{2,L}}{m_1 + m_2}, \tag{3.3.16}$$

and in a precessing spin parameter

$$\chi_p = \frac{1}{A_1 m_1^2} \max(A_1 S_1^\perp, A_2 S_2^\perp), \tag{3.3.17}$$

where $A_1 = 2 + 2/3q$ and $A_2 = (2 + 3q/2)$. This last quantity is the averaged total in-plane spin and is approximately conserved [91, 120].

3.3.2.3 Double-spin multiscale analysis (MSA)

A multiscale analysis [111] has been applied to the post-Newtonian equations of motion, exploiting the separation between timescales. During most of the binary evolution, it holds that $t_{\rm orb} \ll t_{\rm prec} \ll t_{\rm RR}$, where $t_{\rm orb}$ is the orbital timescale, $t_{\rm prec}$ the precessing one and $t_{\rm RR}$ the radiation reaction [121]. This method permits to split the precessing angles into different contributions which depend on the different timescales involved. For instance, the angle α can be split into

$$\alpha(t) = \alpha_{-1}(t) + \alpha_0(t), \tag{3.3.18}$$

where α_{-1} is the leading MSA order (Equation 66 in [111]) averaged over the precession timescale, and $\alpha_0(t)$ is the first order correction which includes information about the relative orientation between the black hole spins (Equation 67 in [111]). The angle β can then be found as the angle of the precession cone if the inertial **J**-frame is considered (Eq.8 of [111]):

$$\cos\beta = \frac{J^2 + L^2 - S^2}{2JL}. \tag{3.3.19}$$

3.3.3 Frame definitions

Unlike non-precessing systems, precessing binaries do not have a preferred inertial frame. The election of this frame determines the simplicity of the waveform. A particular fixed frame which simplifies the waveforms is the one defined by the total angular momentum of the system

$$\mathbf{J}(t) = \mathbf{L}(t) + \mathbf{S}_1(t) + \mathbf{S}_2(t) \tag{3.3.20}$$

at some reference time, so we set $\hat{z} = \hat{\mathbf{J}}(t_{\rm ref})$. This is referred to as the **J**-frame, in which the decomposed waveform will show a particularly simple form. In fact, the direction of **J** remains approximately constant during the evolution of the system, which makes it a suitable frame. Nevertheless, under certain conditions this frame may flip, a phenomenon known as *transitional precession* [7, 122, 123]. This type of precession occurs when the orbital angular momentum and the sum of the spin components have almost the same magnitude, but opposite directions, which implies that the total angular momentum is small. The orbital angular momentum scales proportional to the distance between both black holes, so initially, at very large separation the orbital angular momentum tends to infinity. During the binary evolution, the spin components are approximately kept constant, while during the emission of gravitational waves, orbital angular momentum is radiated. Hence, in an appropriate set of coordinates, at some reference time **J** will point along the positive z-axis. As the binary evolves, due to the emission of orbital angular momentum **J** will decrease until it crosses the orbital plane, where it changes the sign compared to its value at the reference time. This phenomenon can be seen in Figure 3.4.

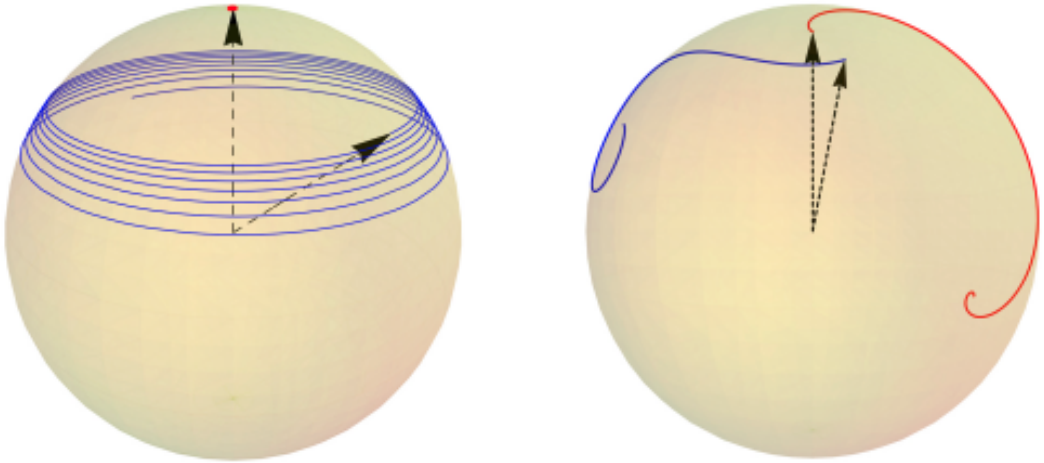

Figure 3.4: Evolution of the total angular momentum $\mathbf{J}(t)$ (in red) and of the orbital angular momentum $\mathbf{L}$(t) (in blue), where at the reference time $\mathbf{J}(t_{\rm ref})$ points along the z-axis. The left plot shows a case of simple precession, where the precession cone generated by $\mathbf{J}$ is much smaller than the evolution of $\mathbf{L}$, which shows the precession of the orbital plane. In this case it is clear that one can assume that the total angular momentum is preserved. The right plot, on the other hand, shows the same evolution, but in the case of transitional precession. In this case the direction of $\mathbf{J}$ is no longer preserved and during the binary evolution it moves away from its initial position and crosses the orbital plane, becoming negative. Credit: [7].

Another common frame is the one described by the orbital angular momentum $\mathbf{L}$, where in this case the z-axis is defined as the value of $\mathbf{L}$ at some reference time t_0. An alternative is to use instead the Newtonian orbital angular momentum $\mathbf{L_N}$, which points in the direction of the instantaneous angular frequency vector. An accurate approximation is to neglect the difference between $\mathbf{L_N}$ and $\mathbf{L}$ and use $\mathbf{L_N}$, since it is simpler to determine. This new frame is referred to as the $\mathbf{L_0}$-frame, which has the advantage that the spin components parallel and orthogonal to $\mathbf{L}$ are approximately preserved (see discussion in e.g. [124]). Therefore, this frame is preferred when defining the spin vectors for initial data sets in NR, since the spins will change little in time. This feature implies that the co-precessing waveform will exhibit the same features as the one produced by a system with the same parallel components of $\mathbf{S}$. This simplicity comes however at the price of a more complex description of the spherical harmonic modes. In any case, both frames are related by a global time-independent rotation, so one can compute the spherical harmonic modes in the $\mathbf{L_0}$ frame from the ones in the $\mathbf{J}$ frame as (considering the Euler angle description for the rotation)

$$h^{\mathbf{L_0}}_{lm}(t,\boldsymbol{\lambda}) = \sum_{m'=-l}^{l} \mathcal{D}^{l}_{mm'}(-\gamma_{\rm ref},-\beta_{\rm ref},-\alpha_{\rm ref}) h^{\mathbf{J}}_{lm'}(t,\boldsymbol{\lambda}). \tag{3.3.21}$$

If we align the z-axis of the inertial frame in the chosen direction, either $\mathbf{L}(t_{\rm ref})$ or $\mathbf{J}(t_{\rm ref})$, then the choice of the other axes becomes arbitrary. For instance, one can define the x-axis as the direction between the larger and smaller black holes at a reference time $t_{\rm ref}$, so $\hat{\mathbf{x}} = \mathbf{r}_1(t_{\rm ref}) - \mathbf{r}_2(t_{\rm ref})$. Finally, the y-axis can be constructed by applying orthogonality with the triad and the right-hand-side rule.

On the other hand, since the co-precessing frame tracks the orbital plane, the non-inertial z'-axis will be defined by the direction of $\mathbf{L}$ (or approximately $\mathbf{L_N}$). This vector is parametrized by the spherical Euler angles (α, β) in the inertial frame, as seen in Figure 3.3. The rotation freedom around that axis is also fixed by an arbitrary choice. In this project we will set $\mathbf{x}' = \mathbf{L_x}$, which is the same convention used in Ref. [114].

CHAPTER 4

Fourier Domain description of precession

As we have seen in Section 1.3, the noise characterization is naturally performed in the Fourier domain, which is also the natural domain for matched filter methods. Hence, it is more efficient and convenient to directly deal with models in the Fourier domain, in order to avoid the noise associated to Fourier transforms of time domain models. Fourier domain waveforms are then essential tools for data analysis methods based on matched filtering. Specifically, the use of phenomenological frequency domain models has had important implications for applications in Bayesian analysis, since low computational cost is needed in order to evaluate the waveforms. Nevertheless, both time and Fourier domain models provide crucial information.

Current phenomenological models use closed form expressions for the modes, and in order to get these analytical expressions of the twisted modes, the *Stationary Phase Approximation* (SPA) [9] has been employed, which is based on the cancellation of sinusoids of rapidly oscillation phase and can be used to compute Fourier transforms of gravitational wave signals. A more detailed explanation of this approximation can be found in Section 4.1. This method is however not well suited for the merger and ringdown. For high-mass black hole events such as GW190521 [27], models that rely on this approximation may not provide accurate results, since only the problematic stages are in the sensitive frequency range of the detectors. Time domain models, however, do not depend on the SPA and hence provide a more accurate description of the late binary evolution, even though they imply more computational cost. As an attempt to go further the SPA approximation, a formalism called *shifted uniform assymptotics* (SUA) was introduced in Refs. [125, 126], although it still relies on the SPA for the underlying precessing waveform and hence, it is limited to the inspiralling phase. Another disadvantage of the Fourier domain representation of precession is that a complete evolution of the Euler angles has not been yet achieved. Whereas in the time domain the Euler angles during ringdown can be easily computed from the quasi-normal modes of the remaining final Kerr black hole [127], in the Fourier domain a closed form expression has not been found based on black hole perturbation theory.

Even with these limitations, precessing phenomenological models in the Fourier domain have become essential tools for gravitational wave analysis. This is then the main motivation of the project: going beyond these approximations can imply an improvement on previous phenomenological frequency domain waveforms for next run O4. It will also address some of the current uncertainties about the following steps for these models, such as the real

limitations of the SPA and the prospect of calibrating them to NR. The method we will implement, based on Ref. [8], does not rely on the SPA approximation, but directly looks for a transfer function in the frequency domain employing the time domain modulation, a mathematical function which models the precessing waveform. In particular, we will compare this procedure to the most recent precessing model in the Fourier domain of the IMRPhenom family, IMRPhenomXPHM [97].

This Chapter will be distributed as follows: first we will give a brief overview on the SPA approximation, followed by a description of IMRPhenomXPHM and the key feature we consider for the Marsat and Baker model: the final state which determines the co-precessing modes. Finally, we will describe the approach we follow here.

4.1 Stationary Phase Approximation (SPA)

The Stationary Phase Approximation (SPA) [128] relies on the cancellation of sinusoids with rapidly varying phase. This idea is based on the fact that when adding sinusoids with the same phase, they will add constructively, whereas if the phases change as the frequency evolves, they will add incoherently. This last statement implies that they will vary between constructive and destructive addition. If we consider the following function $I(k)$,

$$I(k) = \int_{\mathbb{R}} g(x) e^{ik\mu(x)dx}, \tag{4.1.1}$$

where $g(x), \mu(x)$ are real-valued functions and k is large real parameter, then the rate of oscillation of the exponential term will be large where $\mu(x)$ does not vanish. Hence, in such cases the exponential term will not contribute to the integral if the oscillation rate of $g(x)$ is lower, since the areas of the positive and negative globes will approximately cancel. In the opposite case in which $k \cdot \mu(x)$ is small, then the exponential term will have a value of approximately 1 and hence the area of those regions will be determined by the width of the region and the amplitude of the real valued function $g(x)$. This shows that $I(k)$ can be estimated by evaluating the integral only in those regions where $k \cdot \mu(x)$ is small, i.e. where the exponential term oscillates slowly: $\frac{d\mu(x)}{dx} \approx 0$. These are the *stationary points* of $\mu(x)$, and the integral over the vicinity of these points is the main contribution to the total result. Hence, this method provides useful estimates of integrals of oscillating functions. Common integrals that appear in quantum field theory can be approximated by the method of the stationary phase in the limit of small $\hbar$.

The mathematical formulation of the SPA for 1-dimensional functions establishes that, being Σ the set of critical points of a function μ, i.e. points that satisfy $\nabla\mu = 0$, if g has compact support or decays exponentially and k is a sufficiently large and real number, then it holds that

$$\int_{\mathbb{R}} g(x) e^{ik\mu(x)} dx = \sum_{x_0 \in \Sigma} g(x_0) e^{ik\mu(x_0) + \text{sign}(\mu''(x_0))i\pi/4} \left(\frac{2\pi}{k|\mu''(x_0)|} \right)^{1/2} + O(k^{-1/2}). \tag{4.1.2}$$

This method can be extended to Fourier analysis. When computing the Fourier transform of a 1-dimensional complex-valued function $h(t)$, which can be expressed in terms of an amplitude and a phase $h(t) = |h(t)|e^{i\Phi(t)}$, the Fourier transform in our conventions is given by Eq. (A.0.1), so

$$\tilde{h}(f) = \int_{\mathbb{R}} |h(t)| e^{i\Phi(t)} e^{-2i\pi ft} dt = \int_{\mathbb{R}} |h(t)| e^{i(\Phi(t) - 2\pi ft)} dt. \tag{4.1.3}$$

We can now rewrite this last expression in terms of Eq. (4.1.2) by defining

$$\mu(t) = \frac{1}{f}\Phi(t) - 2\pi t, \tag{4.1.4}$$

so one obtains

$$\tilde{h}(f) = \int_{\mathbb{R}} |h(t)| e^{if\mu(t)} dt. \tag{4.1.5}$$

Thus, one can apply the result in Equation (4.1.2) to obtain the Fourier transform of a function $h(t)$. The stationary points satisfy $\frac{d\mu}{dt} = \frac{d\Phi}{dt}\frac{1}{f} - 2\pi = 0$, so they will be given by the times that verify that $\frac{d\Phi}{dt} = 2\pi f$. The approximation will be valid when the oscillation rate of the amplitude $|h(t)|$ is lower than the oscillation of the exponential term, i.e. if $\frac{d|h(t)|}{dt} \ll \frac{d\Phi}{dt}\frac{1}{f} - 2\pi$.

This approach to compute Fourier transforms of oscillating functions can be used to determine the frequency representation of precessing waveforms. However, this method will be only valid during the inspiral for precessing systems. The precession timescale can be despised during the inspiral if compared with the orbital rate, but this approximation is no longer hold during the merger-ringdown. Therefore, one can not assume that the SPA approach will be valid for computing the transfer function during the complete evolution when considering precessing systems.

4.2 IMRPhenomXPHM

Several models have been developed in the framework of precession, and some of them are described in the Fourier domain. Despite the limitations previously mentioned, these models have become fruitful tools for gravitational wave astronomy due to their speed and robustness. In this Section we will focus on IMRPhenomXPHM [97], explaining its main features as well as a more detailed description of the co-precessing modes.

IMRPhenomXPHM is the precessing extension of IMRPhenomXHM [96], a phenomenological frequency-domain model extended to the leading subdominant harmonics, including the $(l, |m|) = (2,2), (2,1), (3,3), (4,4)$ modes and also the *mode mixing* associated to the $l = 3, |m| = 2$ harmonics (see Section 2.2.1). The construction of the precessing model is based on the twisting up approximation described in Section 3.3, the map between the non-precessing aligned system and the precessing one using the Euler angle rotation through Wigner Matrices (3.3.8). For the angles, the method uses both the MSA description and the NNLO described in Sections 3.3.2.3 and 3.3.2.2 in the previous Chapter, parameterized in frequency. Moreover, in order to perform the Fourier transform of Equation (3.3.8), which rotates the co-precessing modes to the inertial ones, the SPA approximation (4.1.2) is used. The expressions for the modes are derived in Appendix E in [97]:

$$\begin{aligned}
\tilde{h}^{\mathrm{I}}_{lm}(f>0) &= \sum_{m'>0}^{l} e^{-im'\epsilon\left(\frac{2\pi f}{m'}\right)} e^{-im\alpha\left(\frac{2\pi f}{m'}\right)} d^{l}_{m-m'}\left(\beta\left(\frac{2\pi f}{m'}\right)\right) \tilde{h}^{\mathrm{cop}}_{l-m'}(f), \\
\tilde{h}^{\mathrm{I}}_{lm}(f<0) &= \sum_{m'>0}^{l} e^{im'\epsilon\left(\frac{2\pi f}{m'}\right)} e^{im\alpha\left(-\frac{2\pi f}{m'}\right)} d^{l}_{m-m'}\left(\beta\left(\frac{-2\pi f}{m'}\right)\right) (-1)^{l} \tilde{h}^{\mathrm{cop}*}_{l-m'}(-f).
\end{aligned} \tag{4.2.1}$$

According to our convention for the Fourier transformation (see Appendix A), which is also the convention used by the LIGO-Virgo collaboration, positive frequencies in the time

domain (e.g. for negative m modes of non-precessing waveforms, see discussion around Eq. (2.2.5)) are translated to support for positive frequencies in the Fourier domain, and negative frequencies in the time domain to support for negative frequencies in the Fourier domain. Unlike for non-precessing systems (see the discussion around Equation (3.3.5)), precessing waveforms show support for both positive *and* negative frequencies. Modes with $m < 0$ will however typically still have larger support for positive frequencies, whereas those with $m > 0$ will have more power in the negative frequency range. In Ref. [8], where the M&B method to go beyond the SPA has been developed, however uses a different convention for the Fourier transform, which maps positive frequencies in the time domain to support for negative frequencies in the Fourier domain. This choice has been made to compensate for complications arising from the choices made in the construction of the original PhenomP model [108].

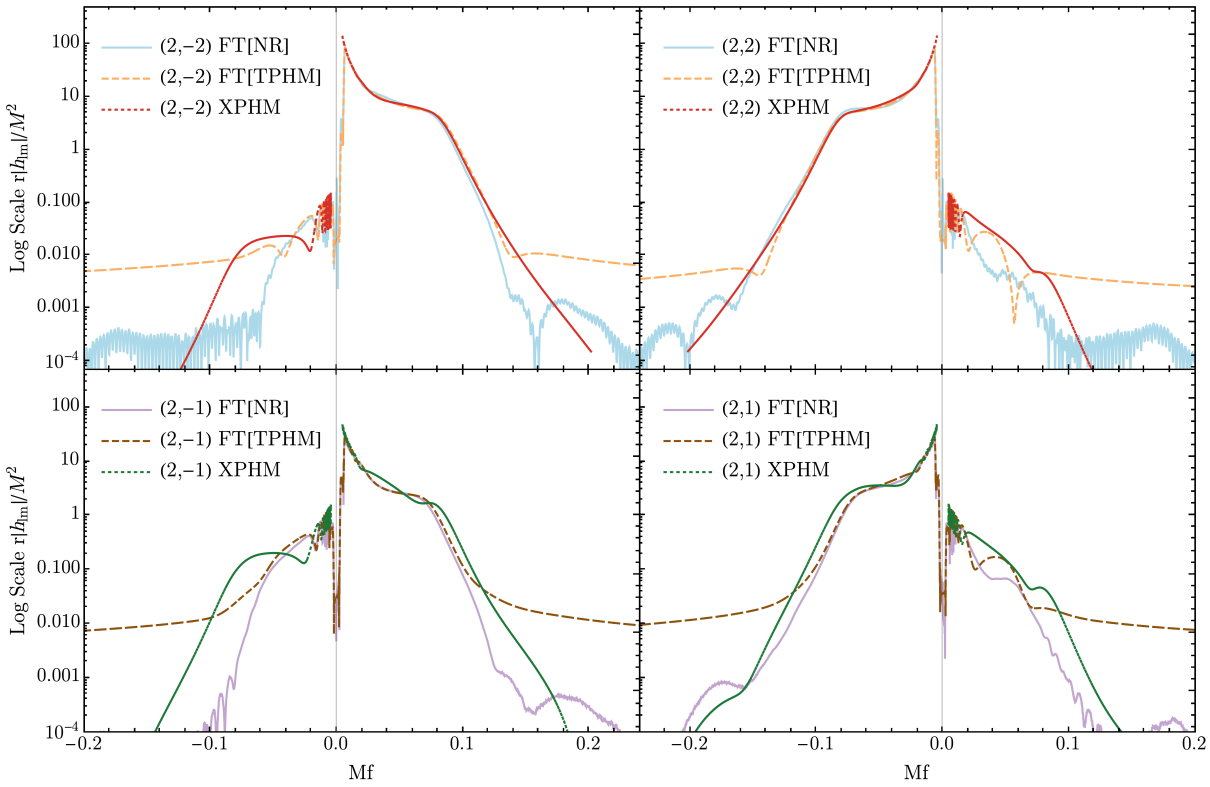

Figure 4.1: Frequency domain representation of the NR waveform SXS:BBH:0037 (see Table 5.1 for details on its properties). The modes are shown in the inertial J-frame, computed via the fast Fourier transform (FFT) for the NR simulation and IMRPhenomTPHM, and the ones for IMRPhenomXPHM are obtained via its LAL implementation. Further discussion on this plot can be found in Section 5.1.2.

The fact that precessing modes show support for both positive and negative frequencies also has implications for the ringdown region. For general mergers, both prograde and retrograde *spheroidal* modes will be excited (see the discussion around Eq. (2.2.6)), so the (l, m) *spherical* modes will carry excitations of these two quasinormal modes. Since the ringdown frequencies of the prograde and retrograde modes are different, the signal will show the phenomenon known as "beating": the effective frequency of the (l, m) *spherical* mode will be in between the $\omega^{\mathrm{RD}}_{lm}$ and $\omega^{\mathrm{RD}}_{l-m}$, with the precise value depending on the level of excitation of each QNM: if both $(l, m)_{\mathrm{QNM}}$ modes have the same amplitude, then the

frequency of the *spherical* modes will be the average of both QNM modes, and if one QNM mode is significantly more excited than the other then the effective frequency will correspond to the QNM frequency of that excitation. Figure 4.1 shows the behaviour along the complete range of frequencies of the Fast Fourier transform (FFT) of the NR waveform SXS:BBH:0037 [129] and its simulation using both IMRPhenomXPHM and the FFT of IMRPhenomTPHM.

Despite the inherent approximations, phenomenological frequency domain models which are not tuned to numerical relativity simulations, such as PhenomP, PhenomPv2 or IMRPhenomXPHM have been widely used in gravitational wave data analysis, and have in particular been used to analyze all gravitational wave events detected to date [2, 3]. Due to the failure of the SPA approximation for rapidly varying phases, as it happens in the merger/ringdown regime, the IMRPhenomX family is not recommended for very massive events where only a few cycles around that regime are observed. In a series of recent papers the UIB group has compared the performance of the frequency domain IMRPhenomXPHM and time domain IMRPhenomTPHM models for parameter estimation of interesting observed events, concretely the event GW190412 [130] with strong excitation of subdominant harmonics, a re-analysis of the first event catalog GWTC-1 [131], and of the high mass event GW190521 [52]. The expected inaccuracies of IMRPhenomX in this region of the parameter space have motivated the development of the time domain phenomenological waveform family IMRPhenomT [98–100]. In Refs. [131] and [52] we find that for high masses the IMRPhenomT family indeed provides a better fit to the observed data than IMRPhenomT. In the particular event GW190521, results using IMRPhenomX may lead to significant biases in the parameter estimation analysis. Indeed, even the original publication discussed a range of possible sources [28], and a high number of publications about this event have been released. Focusing on the results obtained in Ref. [52], Figure 4.2 shows the disagreement obtained for the *effective spin parameter* $\chi_{\rm eff}$ between IMRPhenomXPHM and IMRPhenomTPHM. For this event, which only lasted approximately 0.1 s, results obtained from the time domain family are expected to be more reliable. Indeed, only IMRPhenomXPHM has support for a large negative $\chi_{\rm eff}$, i.e. an anti-aligned system, whereas other models (not only IMRPhenomTPHM) show agreement for very low positive values (see Table III in Ref. [52]).

Results shown in Figure 4.2 can only be achieved if efficient and accurate waveform models are available. Parameter estimation runs are expensive due to the Bayesian inference: one needs to perform millions of evaluations in order to obtain converged posterior distribution such as those seen in Figure 4.2. For instance, in the reanalysis of GWTC1 [131] we performed 337 runs using different models of the IMRPhenomX and IMRPhenomT families in less than a week on the MareNostrum4 machine. Many more of these runs were performed for the GW190521 event [52]. Optimizing waveform models may thus have huge implications on these runs, which motivates their continuous improvement. Moreover, due to the natural description of the detector response in the frequency domain, parameter estimation analysis encourages the need to further improve current Fourier domain models and go beyond the SPA, so the merger/ringdown description is also well described. This is then the motivation of this work: we will implement the Fourier domain approach to model precession explained in Ref. [8], which does not rely on the stationary phase approximation. Section 4.3 expands on this procedure.

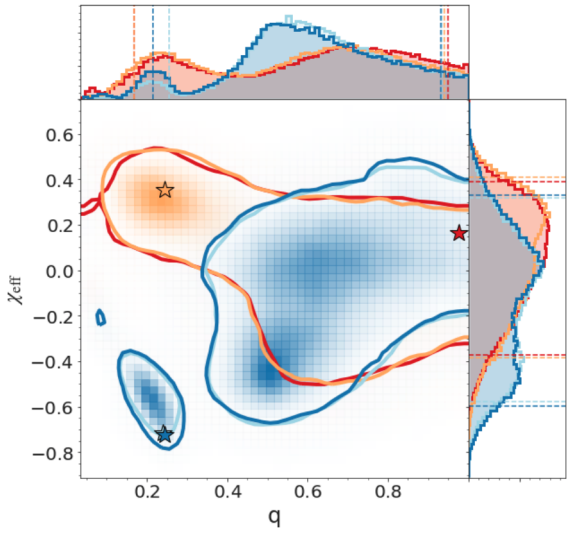

4.2.1: Mass ratio q and effective spin parameter $\chi_{\rm eff}$. Credit: Figure 2 in Ref. [52].

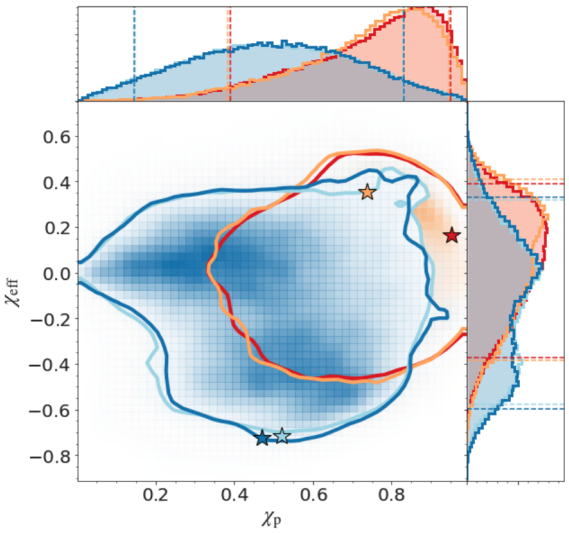

4.2.2: Precession spin parameter $\chi_{\rm p}$ and effective spin $\chi_{\rm eff}$. Credit: Figure 3 in Ref. [52].

Figure 4.2: Two-dimensional posterior distributions obtained with the default versions of IMRPhenomXPHM (MSA angles) in blueish colours and IMRPhenomTPHM (Numerical evolution of the spin equations), in reddish. In concrete, the two different colours for each model show two different methods, pBilby [132, 133] for the dark blue and orange, and LALInference [41] for the red and light blue.

Focusing again on the main features of IMRPhenomXPHM, the other element that requires the approximate map is the final spin modification of the remnant. Even though the final mass is only very weakly affected by the precession, since the radiation of gravitational waves is dominated by the orbital motion and not the precession, the final spin does change in the case of misaligned spins. This occurs due to the vector addition of the individual spins and the orbital angular momentum. The modeling of the co-precessing modes is a key feature of IMRPhenomXPHM, but will also be used in our implementation, so their explicit description will be given in the following subsection.

4.2.1 Modelling the final state

As previously mentioned, the main effect of precession on the final state is not on the mass, but on the final spin of the remnant. Hence, the co-precessing waveform is not the same as the one produced by the aligned system, but needs to be modified due to the vector addition of the black hole spins and the orbital angular momentum. The procedure in order to add this contribution is described in Section IV.D in [97], and is based on keeping the simplicity and domain of validity of phenomenological methods. Below we include the main points of the derivation.

The total angular momentum $\mathbf{J}$ is given by Equation (3.3.20): the sum of the individual spins $\mathbf{S_i}$ and the orbital angular momentum $\mathbf{L}$. The spin components are then split into their orthogonal and parallel components to the orbital angular momentum, $S_{i,\parallel} = \mathbf{S_i} \cdot \hat{\mathbf{L}}$ and $S_{i,\perp} = \mathbf{S_i} - S_{i,\parallel}\hat{\mathbf{L}}$, respectively, so one can define

$$S_{\parallel} = S_{1,\parallel} + S_{2,\parallel}, \tag{4.2.2}$$

$$\mathbf{S}_{\perp} = \mathbf{S_1}_{,\perp} + \mathbf{S_2}_{,\perp}. \tag{4.2.3}$$

The final spin $S_{\rm fin}$ is given then by

$$|S_{\rm fin}| = M_{\rm fin}^2 |a_{\rm fin}| = \sqrt{\mathbf{S}_\perp{}^2 + (S_\parallel + L_{\rm fin})^2}, \tag{4.2.4}$$

where $a_{\rm fin}$ is the final Kerr parameter and $L_{\rm fin}$ can be defined in terms of the final mass, spin and the final Kerr parameter of the corresponding non-precessing configuration $a_{\rm fin}^\parallel$

$$S_\parallel + L_{\rm fin} = M_{\rm fin}^2 a_{\rm fin}^\parallel. \tag{4.2.5}$$

The final mass of the remnant, which is only weakly affected by precession, and the final Kerr parameter $a_{\rm fin}^\parallel$ are computed from the non-precessing system, and depend on the symmetric mass ratio and the spin projections in the $\mathbf{L}$ direction [134]. Moreover, the twisting up approximation assumes for simplicity that the total spin magnitudes and the projections over $\mathbf{L}$ are preserved. Different approaches have been considered to estimate $\mathbf{S}_\perp$ and $S_\parallel$ for Eq. (4.2.4) and an extensive discussion is provided in Sec. IV.D in [97].

Here we will focus on the default version, since this is the one we will consider in this project. For $S_\parallel$ the easiest choice is to consider the non-precessing value due to the assumption of preservation during the twisting up, whereas for $\mathbf{S}_\perp$ one can consider the single-spin description that is used for the NNLO angles introduced in Subsection 3.3.2.2. This approximation is based on post-Newtonian expansions, setting the spin of the smallest black hole to 0 and restricting to spin-orbit interactions [109, 110]. In this approach, it is useful to introduce the *effective spin precession parameter* χ_p [124], which captures the main effect of precession. Based on the assumption that the magnitudes of the in-plane spins $S_{i,\perp}$ oscillate around a mean value, one can average over precession cycles to get the *average spin magnitude* S_P

$$S_p = \frac{1}{2}(A_1 S_{1,\perp} + A_2 S_{2,\perp} + |A_1 S_{1,\perp} - A_2 S_{2,\perp}|) = \max(A_1 S_{1,\perp}, A_2 S_{2,\perp}), \tag{4.2.6}$$

where $A_1 = 2 + 3/(2q)$ and $A_2 = 2 + 3q/2$. At high mass ratios, one can assign the precession to the larger black hole [124], so the *dimensionless effective parameter* is given by

$$\chi_p = \frac{S_p}{A_1 m_1^2}. \tag{4.2.7}$$

If we now include Equations (4.2.6) and (4.2.5) into Eq. (4.2.4), we obtain

$$|a_{\rm fin}| = \sqrt{\left(\chi_p \frac{m_1^2}{M_{\rm fin\parallel}^2}\right)^2 + a_{\rm fin}^\parallel{}^2} \rightarrow S_{\rm fin} = M_{\rm fin}^2 |a_{\rm fin}|. \tag{4.2.8}$$

We have now discussed the estimation of the final spin magnitude, but not the direction. The direction of the final spin will point approximately in the $\mathbf{J}$-direction in case of having a sufficiently small precession cone. The situation can however become challenging for high mass ratio systems, where the orbital angular momentum might become smaller than the sum of the spin components. This leads to the *transitional precession* phenomenon [7, 122, 123] discussed in the previous Chapter (see Figure 3.4), where $\mathbf{J}$ and $\mathbf{L}$ will have negative scalar product and hence the final total angular momentum (which corresponds to the direction of the final spin) will point in the opposite direction compared with its initial value. When the flip of $\mathbf{J}$ occurs, then the twisting-up becomes challenging: the post Newtonian expansions are based on assuming the total angular momentum approximately constant, as well as on the assumption of a precession cone small. In this situation one needs to proceed with caution and compare different approaches and models to conclude if the final result is reasonable. Future work is needed to fix this situation for all those models that depend on post-Newtonian theory.

4.3 Beyond the SPA: Marsat & Baker approach

Previously in this Chapter we have discussed the main advantages of considering waveform models in the Fourier domain for data analysis and also the current limitations of these models when considering precession. Performing the twisting up approximation (see Section 3.3) is a promising approach to model precession, but it is still a challenge how to translate the time-domain modulations created by the frame-rotation into a Fourier-domain transfer function. Previous attempts are based on the SPA and approximations to obtain analytical expressions for the Euler angles parameterized in frequency, as it has been done for instance in IMRPhenomXPHM. The method proposed by Marsat and Baker [8] seeks to overcome these limitations of frequency domain precessing models, and also to deal with the time-dependence of the response of LISA-type instruments to gravitational wave signals [135]. These instruments may accumulate data during months, as opposed to the chirping binaries detected by ground-based detectors, which at most take a few minutes. In this case, the time-domain modulation is due to the motion and change of orientation of the detector constellation along its orbit, which also induces a time delay in the waveform. In this project we will not focus on this application of the method, but it will be considered as a future plan.

The formalism in [8] exploits the separation of timescales for chirping waveforms and treats the problem directly in the Fourier domain, so it can become an efficient method to process signals affected by a time-domain modulation and delays due to both precession or LISA-type detectors. The main motivation of this project is then to reproduce this formalism, focusing only on the effects of precession and to assess its validity and the improvement this performance can imply on current models, and in concrete, on IMRPhenomXPHM. We will now describe the underlying theory of the method following [8].

Given a signal $h(t)$ with an applied time-dependent delay $d(t)$ and followed by a multiplicative modulation function $F(t)$, the final output or signal obtained by the detector $s(t)$ is given by

$$s(t) = F(t)h_d(t) = F(t)h(t + d(t)). \tag{4.3.1}$$

This method looks for an efficient way to compute its Fourier transform, $\tilde{s}(f)$, using a transfer function τ that includes the extra time dependence included in the modulation and the delay, such that

$$\tilde{s}(f) = \tau(f)\tilde{h}(f). \tag{4.3.2}$$

For the moment, we will only consider signals from precessing systems, so we can ignore the delays and assume exclusively the time-domain modulation. In this case, the modulations are given by Wigner matrices in terms of the Euler angles, so we have (see Equation (3.3.8))

$$h^{\mathrm{I}}_{lm}(t, \boldsymbol{\lambda}) = \sum_{m'=-l}^{l} h^{\mathrm{cop}}_{lm'}(t, \boldsymbol{\lambda})\mathcal{D}^{l}_{mm'}(\alpha, \beta, \gamma). \tag{4.3.3}$$

Hence, in this case the objective is to compute mode-by-mode transfer functions $\tau^{l}_{mm'}$, which are defined as

$$\mathrm{FT}[\mathcal{D}^{l}_{mm'}(\alpha, \beta, \gamma)h^{\mathrm{cop}}_{lm'}](f) = \tau^{l}_{mm'}(f)\tilde{h}^{\mathrm{cop}}_{lm'}(f). \tag{4.3.4}$$

The complete Fourier transformed signal is then given as the sum of all the contributions,

$$\tilde{h}^{I}_{lm}(f) = \sum_{m'=-l}^{l} \tau^{l}_{mm'}(f)\tilde{h}^{\mathrm{cop}}_{lm'}(f). \tag{4.3.5}$$

The gravitational wave modes decomposed in the spherical harmonic basis (see Eq. (2.2.3)) for non-precessing systems can be written in terms of their amplitude and phase, which are slowly varying functions of frequency

$$h_{lm}(f) = A_{lm}(f)e^{-i\psi_{lm}(f)}. \tag{4.3.6}$$

The amplitude and phase can thus be sampled on a coarse frequency grid, and this can also be extended to the transfer functions. In order to simplify the following discussion, we will focus on the individual transfer functions $\tau^l_{mm'}$. Equation (4.3.2) thus becomes

$$\tilde{s}^l_{mm'}(f) = \tau(f)^l_{mm'}\tilde{h}_{lm'}(f). \tag{4.3.7}$$

We will now first discuss how to compute a general transfer function $\tau(f)$, and to simplify this argument we will for the momentum suppress all mode indices.

If we consider the convolution theorem (A.2.2), we can now rewrite the Fourier transform of the signal $s(t)$ as a generalized convolution integral

$$\tilde{s}(f) = \int \mathrm{d}f'\ \tilde{F}(f')\tilde{h}(f - f'), \tag{4.3.8}$$

where the conventions for the Fourier transforms are those specified in Appendix A. Note that the conventions used in [8] are not the same we consider in this project, but with the signs flipped. The idea of the method is to seek an efficient way to compute the integral above, making use of the separation between timescales when considering precession. Since the time-domain modulation due to precession is much slower than the inspiral rate, one would expect that $\tilde{F}(f')$ has compact support, i.e. $f' \in |-f_{\max}, f_{\max}|$, where $f_{\max}$ is the maximal frequency for the modulation, roughly the inverse of its timescale. This implies that the integral in (4.3.8) is localized in frequency, so one can do a Taylor expansion of $\tilde{h}(f - f')$ around $\tilde{h}(f)$. One needs however to be careful and ensure that $\tilde{h}(f - f')$ does not vary too much on the range of f'. Doing this expansion at lower order for the amplitude-phase representation (4.3.6), one can recover a locality in time: the response can be approximated to an evaluation of the modulation at a signal-dependent time t_f. Keeping the Fourier-domain amplitude constant and expanding the Fourier domain phase ψ to first order, we get for Eq. (4.3.8) [8]

$$\tilde{s}(f) \approx \tilde{h}(f)\int \mathrm{d}f'\ \tilde{F}(f')\exp\left[if'\frac{\mathrm{d}\psi}{\mathrm{d}f}\right] = \tilde{h}(f)F\left(\frac{1}{2\pi}\frac{\mathrm{d}\psi}{\mathrm{d}f}\right), \tag{4.3.9}$$

where the last equality stands for the definition of the inverse Fourier transform (A.0.2). Thus, we can think of the transfer function as the evaluation of the modulation at a frequency-dependent effective time

$$t_f = \frac{1}{2\pi}\frac{\mathrm{d}\psi}{\mathrm{d}f}, \tag{4.3.10}$$

so one gets $\tilde{s}(f) = \tilde{h}(f)\tau(f) = \tilde{h}(f)F(t_f)$, which depends on the frequency implicitly through t_f. This correspondence between time and frequency is in fact a generalization of the one obtained through SPA [8], but in our case it is exclusively related to the Fourier domain waveform. On the contrary, the SPA correspondence is based on the relation of the frequency f to a time-domain frequency- the orbital frequency ω. Indeed, we will see that t_f is not monotonous and hence it would forbid an unambiguous time-domain

frequency as the SPA needs, whereas in our description t_f will be a well-behaved function if the phase is differentiable. Another advantage of Equation (4.3.10) is that it can be extended through merger and ringdown and does not fail where the SPA does not hold.

We can now go beyond the leading order for both the phase and the amplitude and compute their Taylor expansions:

$$\psi(f-f') = \psi(f) - 2\pi f' t_f + \sum_{p\geq 2} \frac{(-1)^p}{p!} f'^p \frac{\mathrm{d}^p \psi}{\mathrm{d}f^p}, \tag{4.3.11}$$

$$A(f-f') = A(f) + A(f) \sum_{q\geq} \frac{(-1)^q}{q!} f'^q \frac{1}{A} \frac{\mathrm{d}^q A}{\mathrm{d}f^q}. \tag{4.3.12}$$

One can obtain the transfer functions due to the phase and amplitude expansions by introducing the previous results in Equation (4.3.8) [8]

$$\tau_{\mathrm{phase}}(f) = \sum_{p\geq 0} \frac{(-i\epsilon)^p}{2^p p!} (T_f)^{2p} \frac{\mathrm{d}^{2p} F}{\mathrm{d}t^{2p}}(t_f), \tag{4.3.13}$$

$$\tau_{\mathrm{ampl}}(f) = \sum_{p\geq 0} \frac{1}{p!} (T_{A_p})^p \frac{\mathrm{d}^p F}{\mathrm{d}t^p}(t_f), \tag{4.3.14}$$

where ϵ is defined as $\epsilon = -\mathrm{sgn}(d^2\psi/df^2)$ and two new timescales have been introduced, which appear naturally when performing the Taylor expansions [8],

$$T_f^2 = \frac{1}{4\pi^2} \left| \frac{\mathrm{d}^2 \psi}{\mathrm{d}f^2} \right|, \tag{4.3.15}$$

$$(T_{A_p})^p = \frac{1}{(2\pi)^p} \frac{1}{A(f)} \left| \frac{\mathrm{d}^p A}{\mathrm{d}f^p} \right|. \tag{4.3.16}$$

We can now discuss the physical interpretation of the timescale T_f. The same way it happens for t_f, there is a correspondence with the SPA: if we apply the definition (4.3.15) to the inspiral, where the SPA holds, then it can be shown that [8]

$$T_f^{\mathrm{SPA}} = \frac{1}{\sqrt{2\dot{\omega}(t_f^{\mathrm{SPA}})}}. \tag{4.3.17}$$

The last equality implies that T_f corresponds to the radiation-reaction timescale [121] when the SPA is valid: the shorter T_f, the faster the binary will chirp to higher frequencies during the (quasi-circular) inspiral. Even though this result generalizes the SPA behaviour, the definition (4.3.15) only depends on the Fourier-domain waveform and does not need a time-domain frequency as ω. Moreover, this quantity can be extended though merger and ringdown where the SPA is not valid anymore.

Phase corrections can be included as an integral transform, so one can consider both the phase and amplitude corrections at the same time. This leads to an alternative interpretation of the phase corrections, which is the one used in this work. If we rewrite Eq. (4.3.9), expanding the phase up to second order and writing explicitly the Fourier transform of $F(t)$, we obtain

$$\begin{aligned} \tilde{s}(f) &\approx \tilde{h}(f) \int \mathrm{d}t\ F(t) \int \mathrm{d}f' e^{-i2\pi f'(t-t_f)} \exp\left[2i\pi^2 \epsilon f'^2 T_f^2\right] = \\ &= \tilde{h}(f) \sqrt{\frac{1}{2\pi T_f^2}} \int \mathrm{d}t\ F(t) \exp\left[\frac{(t-t_f)^2}{2i\epsilon T_f^2}\right], \end{aligned} \tag{4.3.18}$$

where the second equality holds after solving the integral for f'. If we now define the Fresnel transform of a function F evaluated at some reference time t_0 and of timescale τ as [8]

$$\mathcal{F}_{\tau,\epsilon}[F](t_0) = \frac{e^{i\epsilon\pi/4}}{\sqrt{2\pi\tau}} \int dt \, \exp\left[\frac{-i\epsilon}{2}\left(\frac{t-t_0}{\tau}\right)^2\right] F(t) = \begin{cases} \mathcal{F}_{\tau,1}[F](t_0), \text{ if } \epsilon = 1, \\ \mathcal{F}_{\tau,1}[F^*](t_0)^*, \text{ if } \epsilon = -1, \end{cases} \tag{4.3.19}$$

then we can rewrite Equation (4.3.18) as in Equation (4.3.2), defining the new transfer function

$$\tau_{\text{phase}} = \mathcal{F}_{T_f,\epsilon}[F](t_f). \tag{4.3.20}$$

The Fresnel transform (4.3.19) is then localized: the part of the integral centered around t_0 will contribute the most. The parameter τ determines how local the transform is, so if τ is small, then the fast oscillations away from t_0 are cancelled, whereas if τ is large, then the integral will have extended support. Focusing on the result obtained in Eq. (4.3.18), the radiation-reaction timescale T_f determines the locality of the Fresnel transform: for a faster-chirping signal the integral will be more focused, while for a slowly-chirping one, the integral will be more extended.

The result obtained for the transfer function when considering up to second order for the phase expansion can be related to the treatment of References [125, 126], where they extended the SPA in a new formalism called the Shifted Uniform Asymptotic expansion. Although their approach still relies on the SPA for the underlying signal, an intermediate result can be associated with the Fresnel transform obtained in Eq. (4.3.20): they proposed a quadrature rule as an approximation to the Fresnel transform (4.3.19) [126]

$$\mathcal{F}^N_{\tau,\epsilon}[F](t_0) = \frac{1}{2}\sum_{k=0}^{N} a^{\epsilon}_{N,k}(F(t_0+k\tau) - F(t_0-k\tau)), \tag{4.3.21}$$

where $a^{\epsilon}_{N,k}$ are the solution of an $N+1$ dimensional linear system

$$(-i\epsilon)^p(2p-1)!! = \sum_{k=0}^{N} a^{\epsilon}_{N,k} k^{2p} \text{ for } p = 0, ..., N. \tag{4.3.22}$$

In practice just a few terms are needed to have a converged result for the expansion and in this project we will consider $N_{\max} = 3$. This reformulation has the advantage that it is more numerically stable than computing directly the integral (4.3.19) directly, which is exchanged by the time evaluation of a smooth function.

Finally, one can now develop a new transfer function that includes both the phase and the amplitude corrections. If the Taylor expansions (4.3.11)-(4.3.12) are introduced in Equation (4.3.8), up to second order for the phase and all the terms for the amplitude, it is straightforward to show that Equation (4.3.8) can be rewritten as [8]

$$\tilde{s}(f) \approx \tilde{h}(f)\frac{e^{i\epsilon\pi/4}}{\sqrt{2\pi}T_f} \int \mathrm{d}t \, \exp\left[\frac{-i\epsilon}{2}\frac{(t-t_f)^2}{T_f^2}\right] \sum_{k\geq 0}^{A_{\max}} \frac{(-i)^k}{k!}(T_{A_k})^k \frac{\mathrm{d}^k F(t)}{\mathrm{d}t^k}. \tag{4.3.23}$$

Hence, comparing with Equation (4.3.2), we can define the final transfer function as

$$\begin{aligned} \tau(f) &= \sum_{k\geq 0}^{A_{\max}} \frac{(-i)^k}{k!}(T_{A_k})^k \mathcal{F}_{T_f,\epsilon}\left[\frac{\mathrm{d}^k}{\mathrm{d}t^k}F(t)\right](t_f) = \\ &= \sum_{k\geq 0}^{A_{\max}} \frac{(-i)^k}{k!}(T_{A_k})^k \mathcal{F}^N_{T_f,\epsilon}\left[\frac{\mathrm{d}^k}{\mathrm{d}t^k}F(t)\right](t_f), \end{aligned} \tag{4.3.24}$$

where the last equality holds after exchanging the Fresnel transfer integral (4.3.19) and the quadrature approximation (4.3.21) for $N \to \infty$. In practise, as already mentioned, the sum will be truncated after the $N = 3$ terms, and for the amplitude expansion only the few first of these terms are relevant. Indeed, in this project only the first three terms of the expansion will be considered, up to $A_{\max} = 2$, as it has been done in [8].

Note that in order to simplify the notation, we have dropped the indices of the transfer function, the signal h and the final output s, but they actually correspond to individual contributions for the different modes, following Eq. (4.3.7). Hence, in order to obtain the inertial modes of the precessing system through Equation (4.3.5), we need to calculate all the matrix elements $\tau^l_{mm'}$, which are explicitly given by

$$\tau^l_{mm'}(f) = \sum_{k\geq 0}^{A_{\max}} \frac{(-i)^k}{k!} (T_{A_k})^k \mathcal{F}^N_{T_f,\epsilon} \left[\frac{\mathrm{d}^k}{\mathrm{d}t^k} \mathcal{D}^l_{mm'}(t) \right] (t_f), \tag{4.3.25}$$

where A_k, T_f, t_f, ϵ are all functions that depend on the mode $h_{lm'}$. Hence, the inertial modes are given by

$$\tilde{h}^I_{lm}(f) = \sum_{m'=-l}^{l} \sum_{k\geq 0}^{A_{\max}} \frac{(-i)^k}{k!} (T_{A_k})^k \mathcal{F}^N_{T_f,\epsilon} \left[\frac{\mathrm{d}^k}{\mathrm{d}t^k} \mathcal{D}^l_{mm'}(t) \right] (t_f) \tilde{h}^{\mathrm{cop}}_{lm'}(f). \tag{4.3.26}$$

If we now consider the symmetries of the Wigner matrices (3.3.12) and the correspondence between the $(l, |m|)$ co-precessing modes (3.1.1), then one can cover exclusively the $m' < 0$ values so the inertial modes are given by

$$\begin{aligned} \tilde{h}^I_{lm}(f > 0) &= \sum_{m'<0}^{l} \tau^l_{mm'}(f) \tilde{h}^{\mathrm{cop}}_{lm'}(f), \\ \tilde{h}^{\mathrm{I}}_{lm}(f < 0) &= \sum_{m'<0}^{l} (-1)^{l+m+m'} \tau^{l*}_{-mm'}(-f) (\tilde{h}^{\mathrm{cop}}_{lm'})^*(-f). \end{aligned} \tag{4.3.27}$$

CHAPTER 5

Marsat & Baker implementation: Results

In the previous Chapter we have described a new approach to deal with precession in the Fourier domain, which does not rely on the SPA, and which has been proposed by Sylvain Marsat and John G. Baker in [8]. In the following, we will usually refer to this method as M&B. The main motivation of this work has been the need to improve current precession prescriptions in frequency domain models. Most of them perform the twisting up procedure employing the Stationary Phase Approximation, described in Section 4.1, which is not reliable during the last part of the binary evolution. Despite the limitations of the SPA, frequency domain models are standard tools in gravitational wave data analysis and have been essential to understand the sources of the detected events up to date. Since the data analysis is performed in the frequency domain, these models are more efficient than those developed in the time domain, which also encourages the development of improved and fast frequency domain models, using preferably closed-form expression. Going beyond the SPA is however a challenge, and different methodologies have been developed to try to surpass that approximation, such as the SUA [125] and the M&B approach [8]. The SUA exploits a hierarchy of different time scales, which is valid during the inspiral, and consequently applications of the SUA in the context of coalescing binaries have focused on the inspiral phase. The M&B method implemented here only depends on mathematical properties of Fourier transforms, and it is thus interesting to test whether it can be used to improve the waveform also during the merger and ringdown.

In the original paper [8], the method was not described in terms of the convention for the Fourier transform used by the LIGO-Virgo collaboration (see Appendix A), and so the first step in this work has been to reproduce their procedure according to the general conventions of the LVC, which has also been used to construct the latest generation of frequency domain models, in particular IMRPhenomXPHM [96]. After working out the M&B algorithm with consistent conventions, I developed a Mathematica implementation of the algorithm, using the variables and expansions described in Section 4.3. There was then a period of testing and code optimization before the final implementation which has been used to obtain the results shown in this Chapter. Results have been split into two cases: first, in analogy to the procedure followed by [8], I have used the M&B approach considering only the dominant harmonics $h^{\rm cop}_{22}$, $h^{\rm cop}_{2-2}$, and compared the results to what I denoted as IMRPhenomXP and IMRPhenomTP. Here IMRPhenomTP corresponds to performing the twisting up just for the $h^{\rm cop}_{2-2}(t)$ mode in Eq. (4.3.3), using the IMRPhenomTPHM prescriptions for the coprecessing modes and the Euler angles, which

will be indicated in each case. IMRPhenomXP is defined as Eq. (4.2.1) computing the sum just for $m' = -2$ and $f > 0$, using the coprecessing modes of IMRPhenomXPHM and the default version of the angles, which corresponds to the MSA angles parameterized as functions of frequency. The resulting waveforms TP and XP show the waveform in the inertial J-frame which comes from the positive frequency contributions of the $l = 2$ modes due to $\tilde{h}^{\rm cop}_{2\pm2}(t)$. I used this approximation for the three cases considered in Ref. [8], called $++$, $--$ and $\perp\perp$, which refer to the relative position of the spin vector with respect to the orbital angular momentum: aligned, antialigned or orthogonal (in-plane spins). I also recreated the event GW190521 using M&B due to the differences between IMRPhenomTPHM and IMRPhenomXPHM shown in Figure 4.2 and the results obtained for the cases $++$, $--$ and $\perp\perp$. Further discussion can be found in Section 5.1.2.

We will then consider the NR simulation shown in Figure 4.1 (SXS:BBH:0037) [129] and perform the M&B algorithm using also the higher modes of $l = 2$, $h^{\rm cop}_{21}$, $h^{\rm cop}_{2-1}$. We chose this simulation because it has considerable precession but still the evolution of the modes in the J-frame is well recovered by IMRPhenomTPHM. In this case, we compared the results to those obtained using IMRPhenomXPHM and IMRPhenomTPHM, which are also shown in Figure 4.1. A brief summary of the cases considered can be found in Table 5.1.

	Case $++$	**Case $--$**	**Case $\perp\perp$**	**GW190521**	**SXS:BBH:037**
q	4	4	4	5	3
$\boldsymbol{\chi}_1(f_{\rm ref})$	(0.34,0.34,0.82)	(0.34,0.34,-0.82)	(0.67,0.67,0)	(0.67,0,-0.54)	(-0.40,0.29,0)
$\boldsymbol{\chi}_2(f_{\rm ref})$	(0.34,0.34,0.82)	(0.34,0.34,-0.82)	(0.67,0.67,0)	(0.56,0,0)	(0,0,0)
$\chi_{\rm f}$	0.95	0.32	0.79	0.48	0.61
$f_{\rm in}$ (Hz)	20	20	20	5	46.7
$f_{\rm ref}$ (Hz)	20	20	20	20	46.7
M ($\rm M_\odot$)	20	20	20	170	20
$M\omega^{\rm QNM}_{22}$	0.78+i0.06	0.43+i0.09	0.59+i0.08	0.46+i0.09	0.51+i0.09
$M\omega^{\rm QNM}_{21}$	0.57+i0.06	0.40+i0.09	0.49+i0.08	0.43+i0.09	0.45+i0.09
HM	✗	✗	✗	✗	✓

Table 5.1: Properties of the cases considered in this work. The final spin χ_f has been computed for the first four cases via the IMRPhenomTPHM default implementation, while for the NR simulation the final spin corresponds to the one included in the metadata. "HM" stands for "Higher Modes", i.e. if for that case all the modes for $l = 2$ have been considered or just $(l = 2, m = \pm2)$.

The M&B algorithm has four inputs: the order of the amplitude expansion A, the order of the stencil quadrature N, the coprecessing IMRPhenomXPHM modes, and the time domain modulation we want to model. The modulation corresponds to the Wigner matrices evaluated for the Euler angles that rotate the waveform from the coprecessing frame to the inertial one, following Equation (4.3.3). For all the cases the results are shown in the inertial J-frame, the time domain evolution of the angles is obtained differently for all cases, and the methodology is specified for each one. Three different prescriptions for the angles are used: the MSA angles defined in Section 3.3.2.3, the angles obtained via numerical evolution of the spins equation (Sec. 3.3.2.1), and for the SXS:BBH:0037 simulation the angles have also been computed directly from the NR waveform using the *quadrupole alignment method*. The MSA angles and those obtained from the numerical spin equations have been obtained from the IMRPhenomTPHM [100] implementation in LAL [116]. One of the main limitations of the M&B algorithm, as we will see in the

results, is the need to compute high order derivatives for both the coprecessing waveform and the time domain angles, as seen in Eq. (4.3.26). Those are however not differentiable to more than second order, so while in general higher orders should be better, in practice we need to restrict to lower orders to obtain a smooth result. Indeed, the highest orders we consider in this project are $A = 2$ and $N = 3$. The main limitation occurs when using numerical angles, in our case both those obtained from IMRPhenomTPHM via the numerical evolution of the spin equations or the ones from the quadrupole alignment. In those cases, it has been necessary to apply a low pass filter in order to smooth the angles and thus, their derivatives. I used the Mathematica function `LowpassFilter`, which applies a low pass filter with a certain cutoff frequency. This frequency has been chosen to eliminate the noisy features of the angles, using a rough value which works for the entire evolution. Hence, whenever numerical angles have been used, a low pass filter has been applied previously to perform the M&B algorithm. In general, the numerical evolution of the IMRPhenomTPHM angles gives more accurate information about the ringdown description of the waveform, as we will see in Figures 5.15 and 5.16. However, the numerical angles can also show non-smooth and noisy features which are not well behaved in the M&B procedure. Hence, we have used that prescription if it was smooth enough to perform the algorithm, while in the other cases the analytical MSA angles have been used. We will now proceed to the discussion of the different cases shown in Table 5.1 and we will split the results depending on whether higher harmonics have been included or not.

5.1 Twisting up the dominant harmonics

In this Section we will discuss the results obtained using the M&B procedure considering only the dominant $\tilde{h}^{\rm cop}_{2\pm2}(t)$ mode, i.e. performing Eq. (4.3.27) only for $m' = -2$ and $f > 0$. We will then compare this results to the XP modes described below, which correspond to Eq. (4.2.1) for $m' = 2$ again for $f > 0$. We will only discuss the results for the positive frequencies due to the correspondence between between the $(l, \pm m)$ modes (see Figure 4.1). In order to determine the reliability of the two models, we do not need to known the true physical waveform, but rather we will use as a proxy the waveform obtained from the IMRPhenomT family, which we will refer to as IMRPhenomTP, as previously described: the contribution to the negative modes corresponds to rotate the $h^{\rm cop}_{2,-2}(t)$ using Eq. (4.3.3). We will first focus on the three cases that are treated in Ref. [8], cases $++,--$ and $\perp\perp$ in Table 5.1 and then discuss the results obtained for the simulation of the event GW190521 in Table 5.1.

5.1.1 Cases $++,--$ and $\perp\perp$

Figure 5.1 shows the evolution of the three Euler angles for the twisting up map between the coprecessing modes and those in the inertial J-frame. Note that we are plotting $\epsilon = -\gamma$, and ϵ is chosen for its closeness to the Euler angle α. Inserting these angles into Eq. (4.3.4) one can obtain the transfer functions using Eq. (4.3.27). From the dominant coprecessing modes (computed using IMRPhenomXPHM), one can calculate the timescales that the algorithm introduces, namely t_f, T_f and $(T_{A_p})^p$ in Eqs. (4.3.10),(4.3.15) and (4.3.16) respectively, with p up to the highest we consider for the amplitude expansion. In our case, we set $A_{\rm max} = 2$, and we show these functions in Figure 5.2. In Figure 5.2.2 we can already see the limitations of the M&B algorithm: second derivatives of the phase and

amplitude (T_f and T_{A_2}) show sharp features due to the underlying coprecessing waveform. Indeed, in this case they correspond to the transitions between the different analytical expressions the complete IMRPhenomXPHM waveform is built from, which are not differentiable up to second order due to the limitations of the phenomenological ansatz.

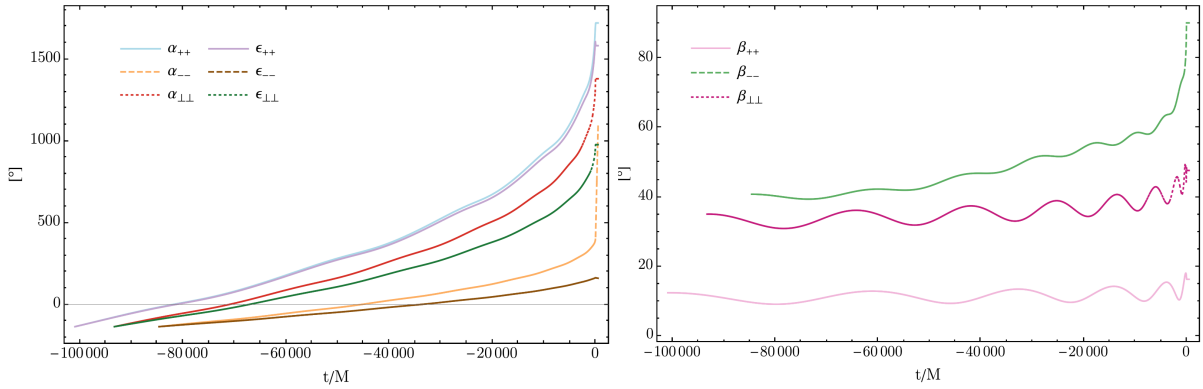

Figure 5.1: Euler angles used to perform the twisting up. For $--$ they have been computed from the numerical evolution of the spins equations, whereas for $++$ and $\perp\perp$ the MSA angles have been employed.

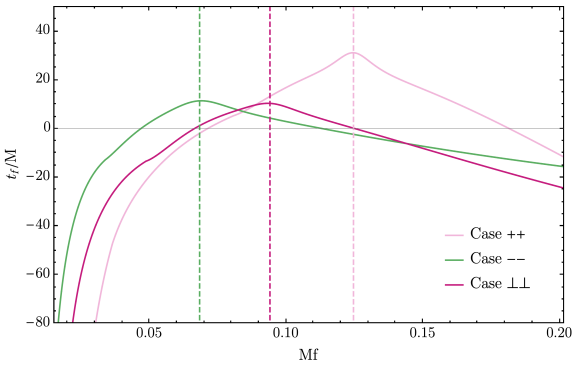

5.2.1: Timescale $t_f(\tilde{h}^{\rm cop}_{2-2}(f))$. The vertical lines correspond to the ringdown frequencies.

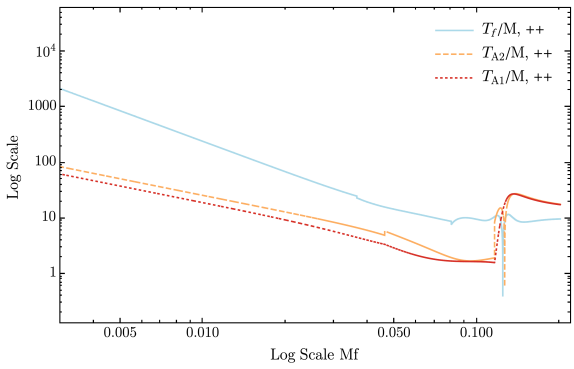

5.2.2: Time scales $T_{A_1}(\tilde{h}^{\rm cop}_{2-2}(f))$, $T_{A_2}(\tilde{h}^{\rm cop}_{2-2}(f))$ and $T_{A_f}(\tilde{h}^{\rm cop}_{2-2}(f))$ for the case $++$.

Figure 5.2: Representation of the different time scales defined in the M&B procedure for the $\tilde{h}^{\rm cop}_{2-2}(f)$ of IMRPhenomXPHM

Figures 5.3, 5.4 and 5.5 show the IMRPhenomXP and IMRPhenomTP modes we will compare with the M&B results, only for the positive frequency range. The plots also include the IMRPhenomXPHM and IMRPhenomTPHM modes, respectively, which contain all the contributions of the $l = 2$ modes in the coprecessing frame. Note that the difference between the positive modes of TPHM and TP may be large depending on the distribution of power in the positive and negative range of frequencies (see Figure 4.1). For instance, in Figure 5.3 we can see that most of the energy content of the $(2, -2)$ mode is in the positive frequency range, which means that the same happens for the $(2, 2)$ mode but for the negative frequencies. Hence, the contribution of the $(2, 2)$ content in the positive frequencies is negligible in the time domain, which leads to the difference in amplitude between IMRPhenomTP and IMRPhenomTPHM seen in that figure. On the other hand, in Figure 5.4 one can see that the contribution of all the modes in the frequency range is similar, and so are the amplitudes in the time domain. The case $\perp\perp$ in Figure 5.5 shows a similar behaviour to the $++$ modes in Figure 5.3. Including higher modes (HM) tend to include extra oscillations in the waveform, due to the contribution of the $h^{\rm cop}_{2\pm1}$ modes, which in general do not show the smooth features of the dominant ones.

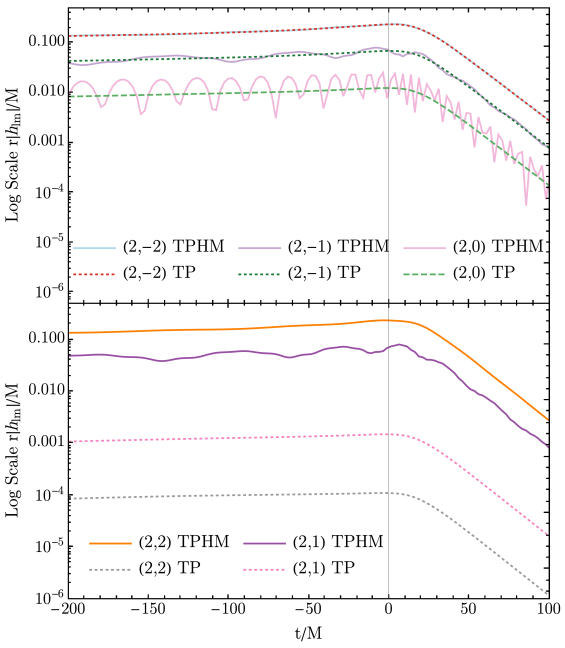

5.3.1: Comparison between TPHM/TP.

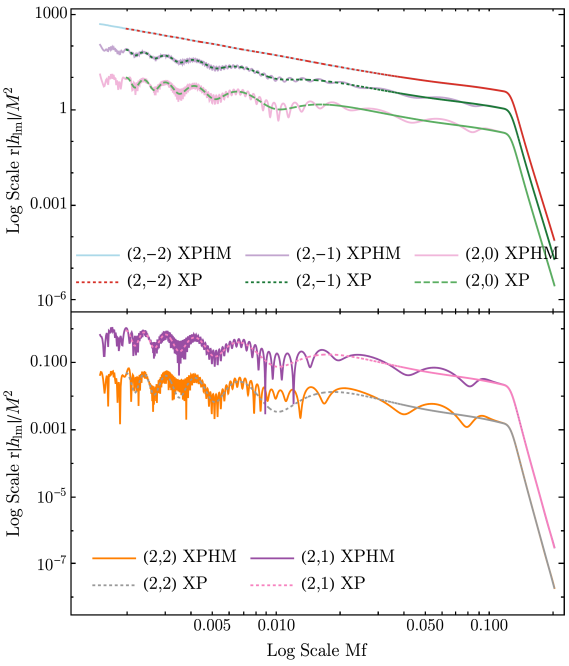

5.3.2: Comparison in the positive frequencies between XPHM/XP.

Figure 5.3: Comparison between the precessing modes in the inertial J-frame with the contribution of all the modes (TPHM/XPHM) and only the $(2, |2|)$ contribution (TP/XP) for the case ++ in Table 5.1.

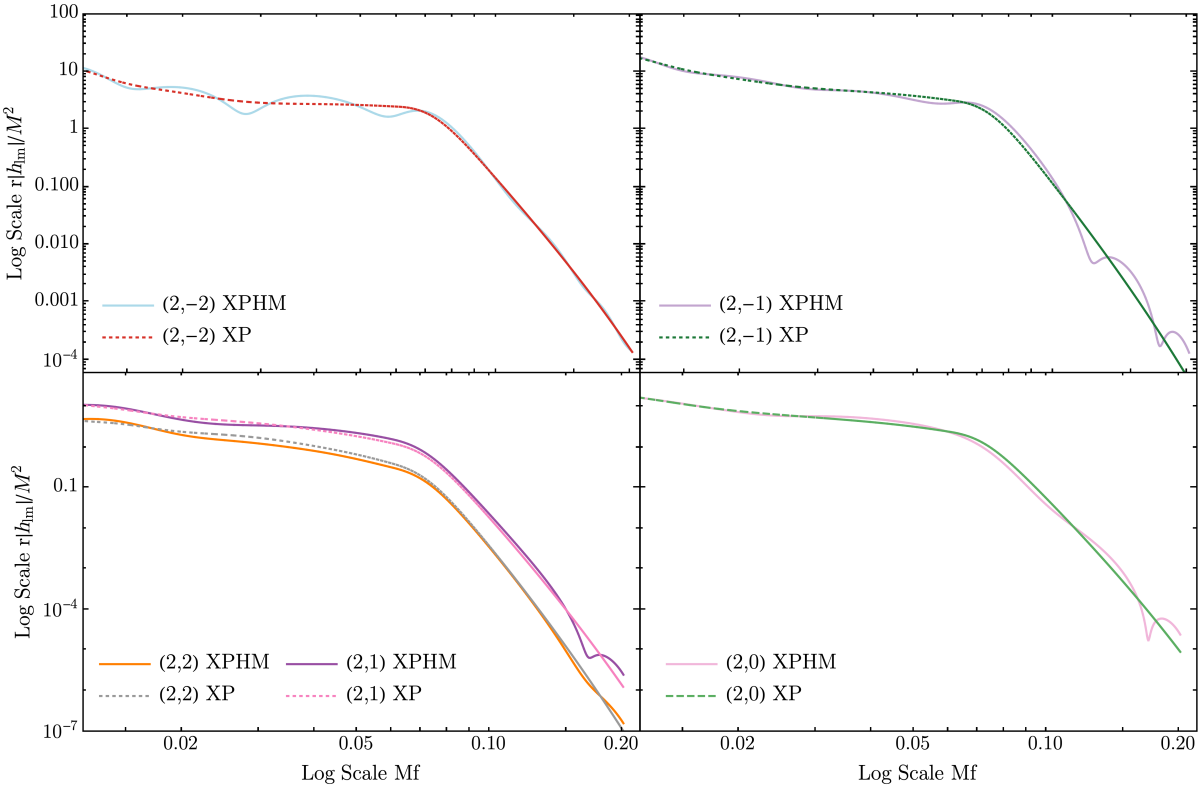

5.4.1: Comparison in the positive frequencies between XPHM/XP.

Figure 5.4: Comparison between the precessing modes in the inertial J-frame with the contribution of all the modes (TPHM/XPHM) and only the $(2, |2|)$ contribution (TP/XP) for the case −− in Table 5.1.

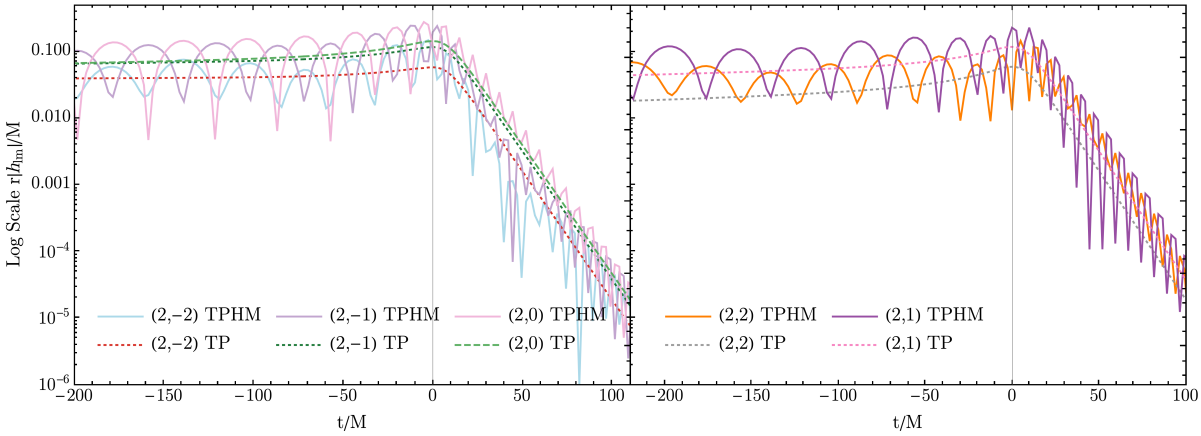

5.4.2: Comparison between TPHM/TP.

Figure 5.4: Continuation.

Note that Ref. [8] compares the results obtained via M&B with only the dominant coprecessing contribution with the FFT of a complete time domain waveform, which includes higher modes beyond the $(2, |2|)$. In this Section, where only the dominant modes are considered for the M&B algorithm, we will compare with the IMRPhenomXP and IMRPhenomTP waveforms described below, which only include the contribution of the modes in the positive frequency range. Only when all the $l = 2$ modes are considered for the twisting up I will compare with the full waveform, as done in Section 5.2

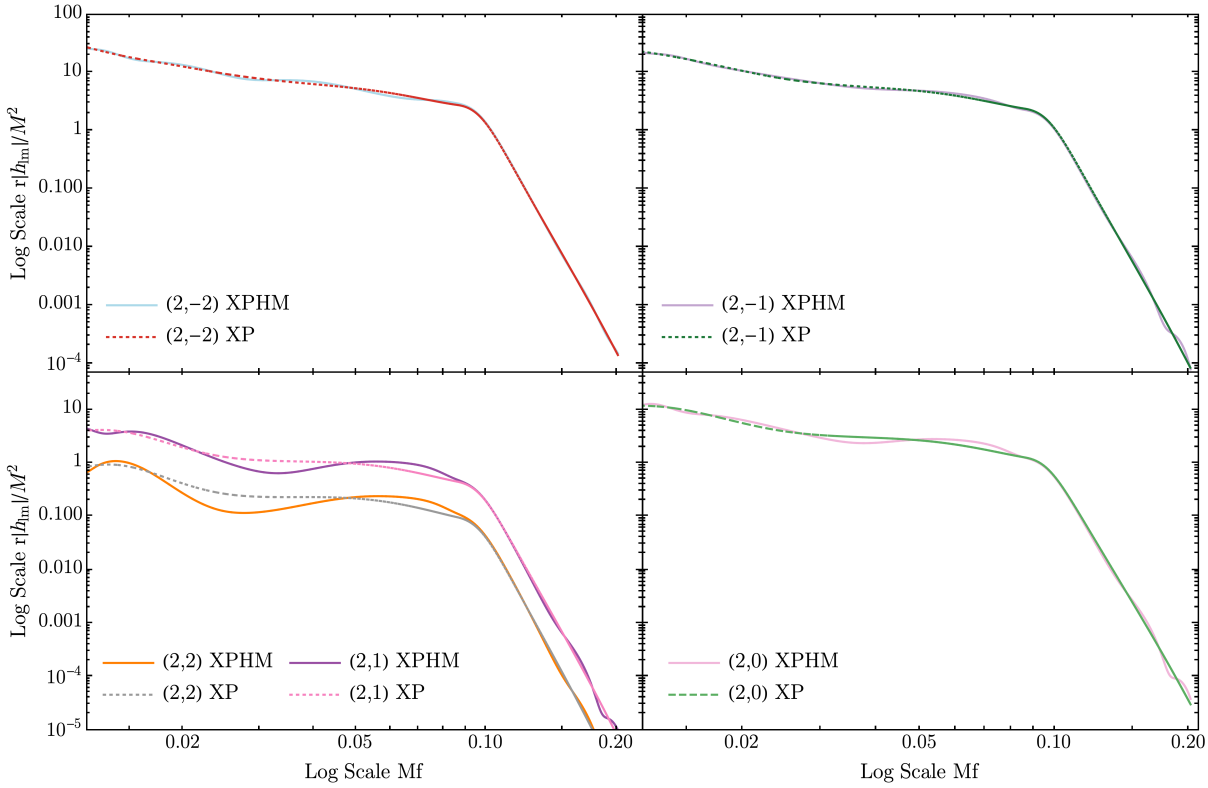

5.5.1: Comparison in the positive frequencies between XPHM/XP.

Figure 5.5: Comparison between the precessing modes in the inertial J-frame with the contribution of all the modes (TPHM/XPHM) and only the $(2, |2|)$ contribution (TP/XP) for the case $\perp\perp$ in Table 5.1.

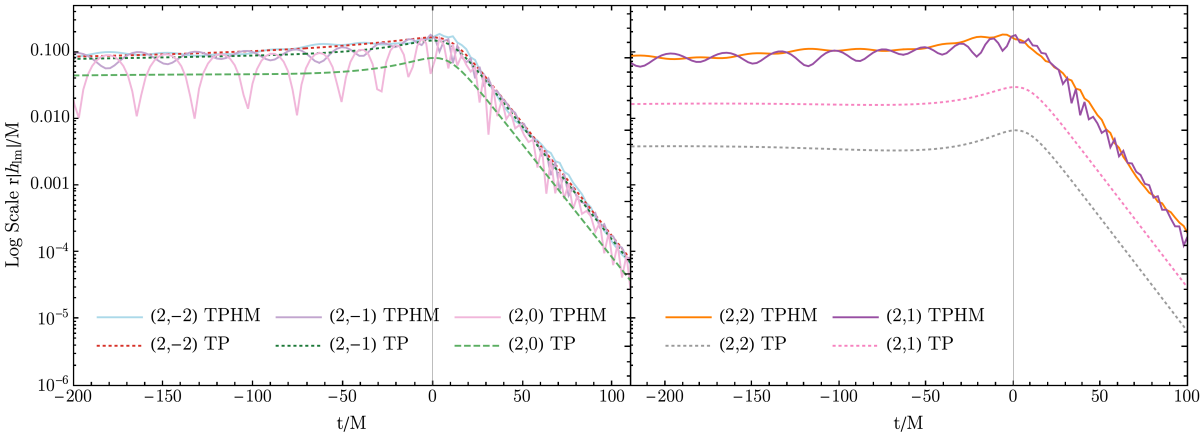

5.5.2: Comparison between TPHM/TP.

Figure 5.5: Continuation.

We can now discuss the results obtained using the M&B procedure. We will first consider the algorithm at the lowest order ($A = N = 0$), which would be analogous to the SPA (Figures 5.6, 5.7, 5.8), and then show the same results for $A = 2, = N = 3$ in Figures 5.6, 5.7, 5.8.

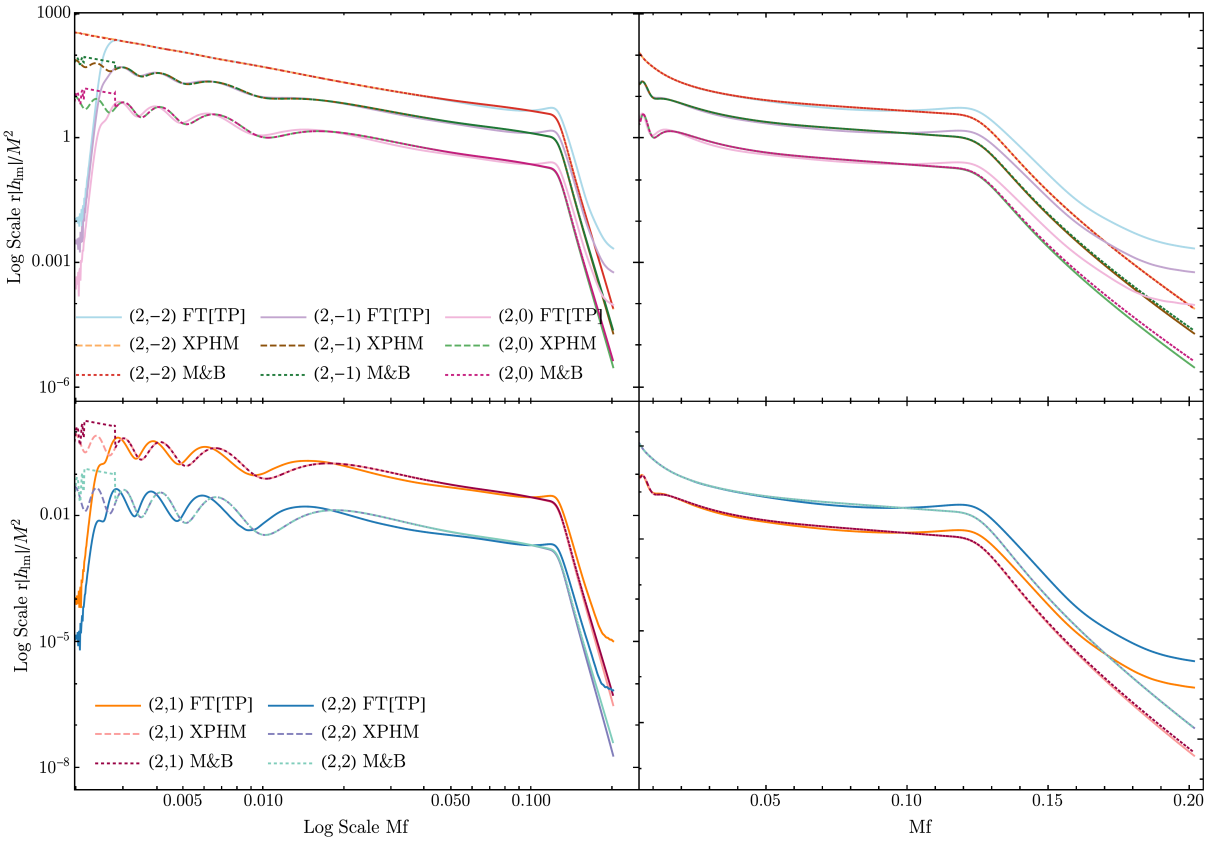

Figure 5.6: Comparison between the inertial J-modes for positive frequencies of TP, XP and M&B. The M&B algorithm has been applied at lowest order for both the amplitude and the stencil expansion (Case ++, $A = N = 0$).

For the lowest order results, the description of the Euler angles used (see Figure 5.1) determines the difference between IMRPhenomXP and M&B. For those cases where the

MSA angles have been used, which are ++ and ⊥⊥ in Figures 5.6 and 5.8, the results for IMRPhenomXP and M&B are very similar. This behaviour is the expected one, since they use the same angle description to perform the twisting up. However, for the case −−, since we used the numerical evolution of the angles to perform M&B, then M&B and IMRPhenomXP differ, and M&B being closer to IMRPhenomTP. Indeed, one of the limitations of most Fourier domain models is that the parametrization of the Euler angles as a function of frequency does not capture completely the underlying physics of the late binary stage, whereas M&B uses directly the time domain modulation.

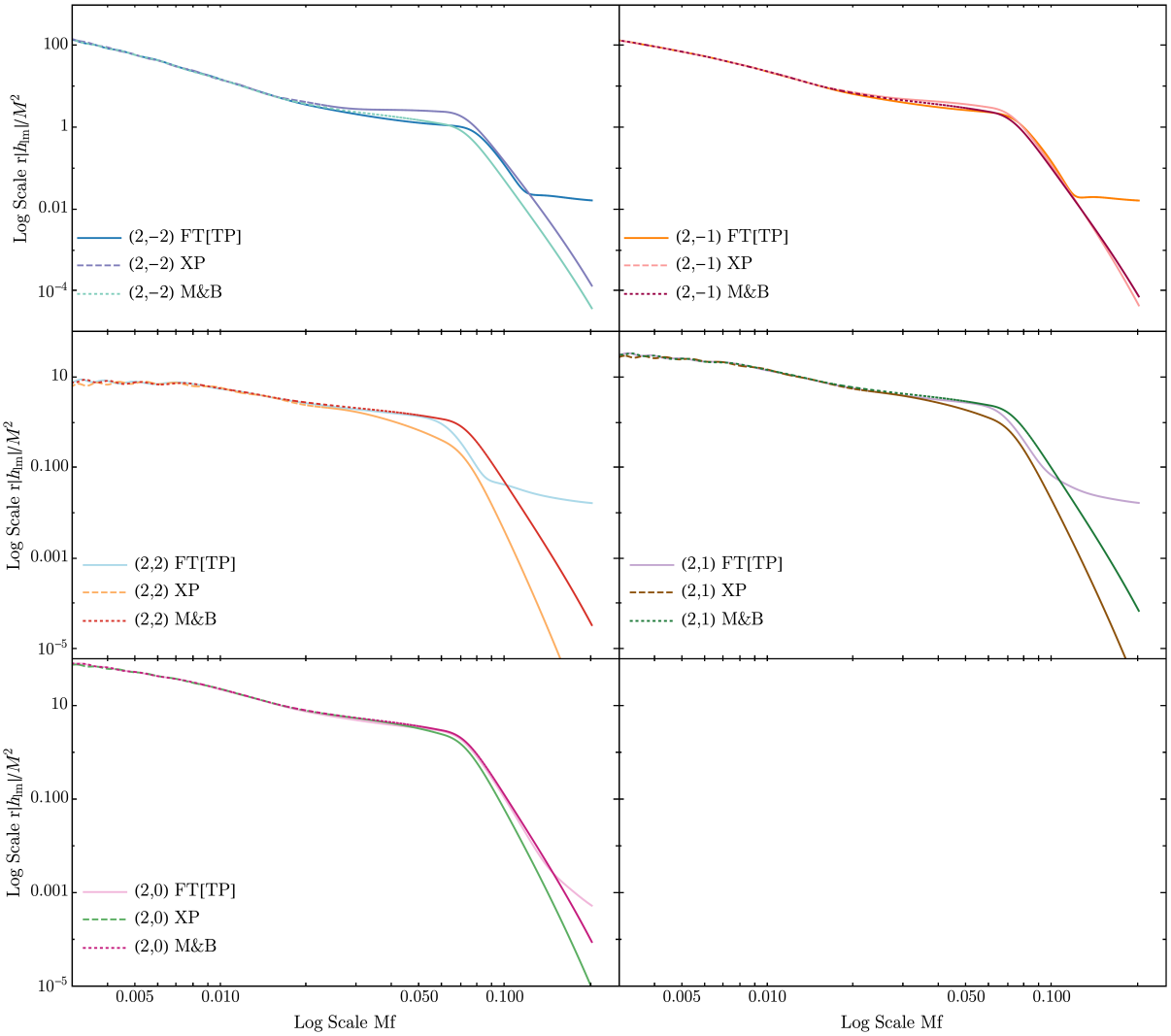

Figure 5.7: Comparison between the inertial J-modes for positive frequencies of TP, XP and M&B. The M&B algorithm has been applied at lowest order for both the amplitude and the stencil expansion (Case −−, $A = N = 0$).

The numerical evolution of the spin equations implemented in IMRPhenomTPHM captures better the precession of the orbital plane than the MSA angles, which suggests that the inertial modes are closer to the ones expected by NR. In that case, as we can see in Figure 5.7 the difference between IMRPhenomXP and IMRPhenomTP becomes very large in the early inspiral for most of the modes, whereas M&B, even at lowest order, recovers much better the expected waveform. The fact that the case −− shows a clear disagreement between IMRPhenomTP and IMRPhenomXP and that

M&B is closer to IMRPhenomTP has also encouraged to check the results of the M&B algorithm in the region of the parameter space relevant for the GW190521 event, where IMRPhenomXPHM showed support but IMRPhenomTPHM did not. Hence, these lowest order examples of the implementation imply that if one can achieve a reliable description of the time domain modulation, which is also differentiable up to a certain order, then M&B performs better than IMRPhenomXP, not because of the SPA, but because the time domain description of the angles contains more physical information.

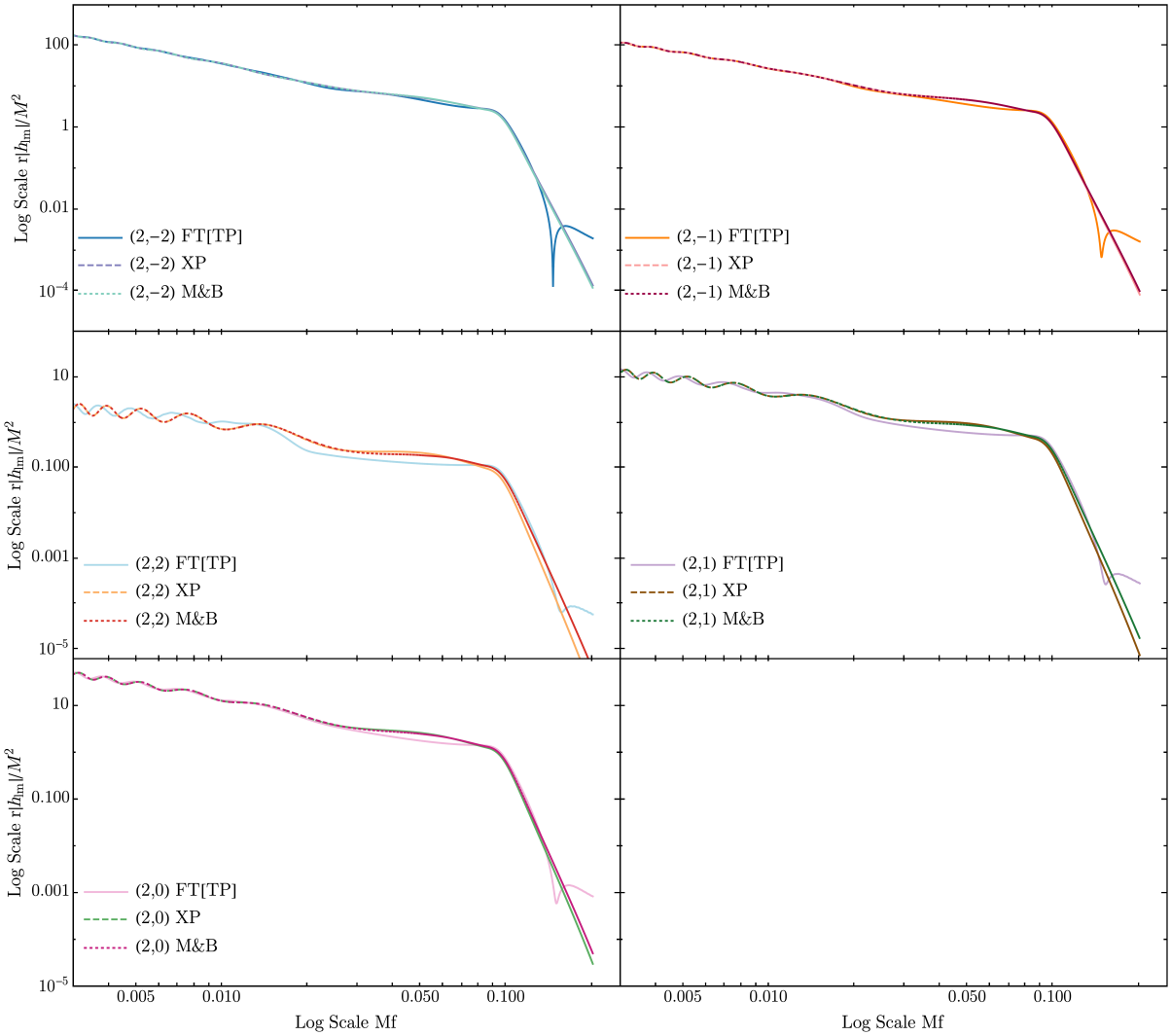

Figure 5.8: Comparison between the inertial J-modes for positive frequencies of TP, XP and M&B. The M&B algorithm has been applied at lowest order for both the amplitude and the stencil expansion (Case $\perp\perp$, $A = N = 0$).

Figures 5.9, 5.10 and 5.11 show the results obtained after applying the M&B algorithm at second order in the amplitude expansion ($A = 2$) and at the third order in the stencil coefficients ($N = 3$) for the cases $++$,$--$ and $\perp\perp$, respectively. Results in these cases not only depend on the angle prescription used, but also on the region of the parameter space, which complicates the assessment of the M&B algorithm. Focusing on Figure 5.9, while at lowest order IMRPhenomXP and M&B showed almost the same behaviour (Figure 5.6), when applying higher order terms M&B agrees better during the inspiral as well as at the higher frequencies slope with IMRPhenomTP. This agreement at

highest frequencies does however not imply that the ringdown is captured better, since the exponential decrease in the Fourier domain contains information about the entire evolution. Indeed, we will see that in the time domain plots in Figures 5.13, 5.12, 5.14. Nevertheless, the Case $\perp\perp$ at higher order in Figure 5.11 does not reflect an immediate improvement over IMRPhenomXP: while it seems to improve the smaller contributions in the positive frequencies (the positive m modes), some features of the dominant modes disagree with IMRPhenomTP more than IMRPhenomXP does. On the other hand, the case $--$ at higher order for the M&B algorithm in Figure 5.10 further improves what we could see in Figure 5.7: it remarkably recovers the time domain modulation included in the algorithm, which leads to the IMRPhenomTP waveform, and in this case the difference with IMRPhenomXP is very accentuated both for the low and high contributions.

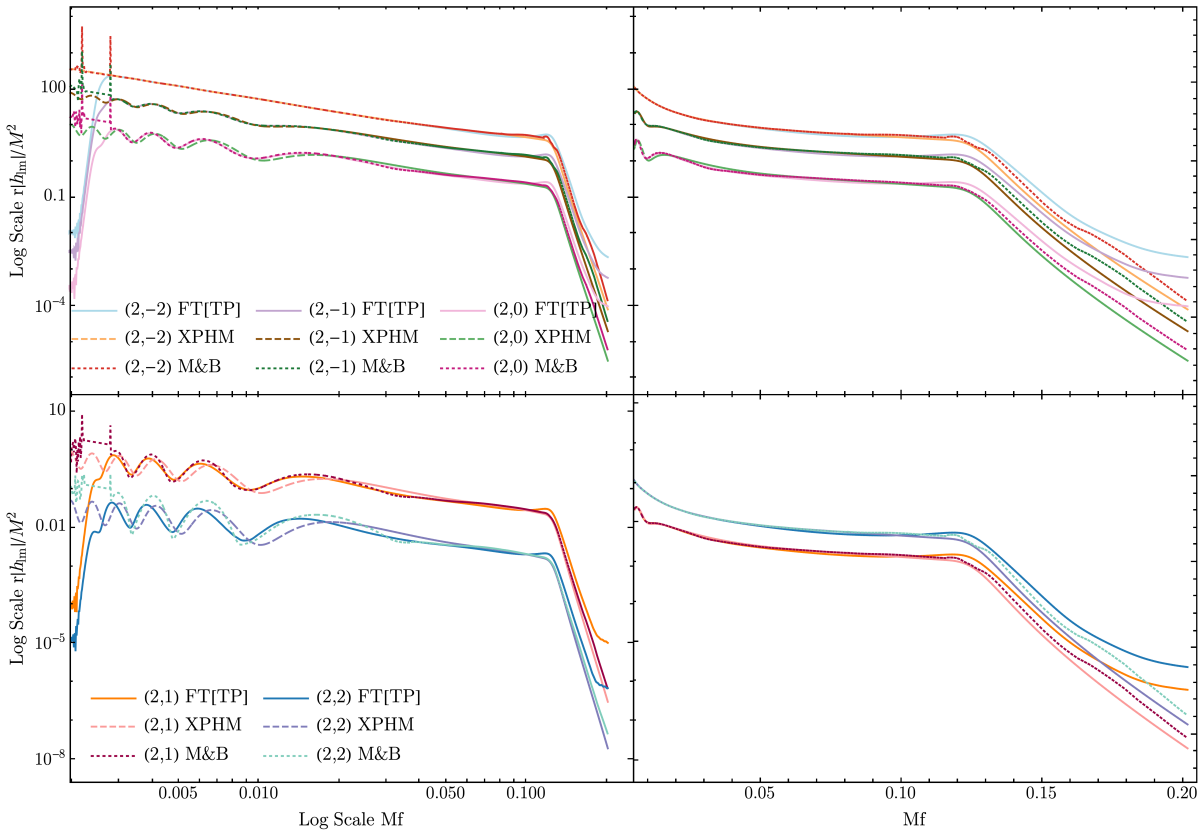

Figure 5.9: Comparison between the inertial J-modes in the positive range of frequencies for TP, XP and M&B. The M&B algorithm has been applied at at second order for the amplitude expansion $A = 2$ and considering three Stencil coefficients $N = 3$ (Case $++$, $A = 2, N = 3$).

We have therefore seen that in the frequency domain, for some of the cases it looks like the M&B algorithm at a sufficiently high order shows an enhancement over IMRPhenomXP, but at the same time in other regions of the parameter space, the performance does not suggest any perceptible improvement. In order to improve our understanding of how the M&B algorithm performs for the ringdown, we move from the Fourier domain to the time domain, where it shows a very simple morphology. Indeed, the SPA tends to fail during the last stage of the binary evolution, and we would be interested in seeing if this is improved with this new methodology. Even though the frequency domain comparison is useful to better understand the different contributions of Eq. (4.3.27) and

see the features of the frequency domain waveform, for a complete understanding a time domain inspection is needed. This comparison was not performed in Ref. [8], and the time domain results for the three cases are in Figures 5.12, 5.13 and 5.14.

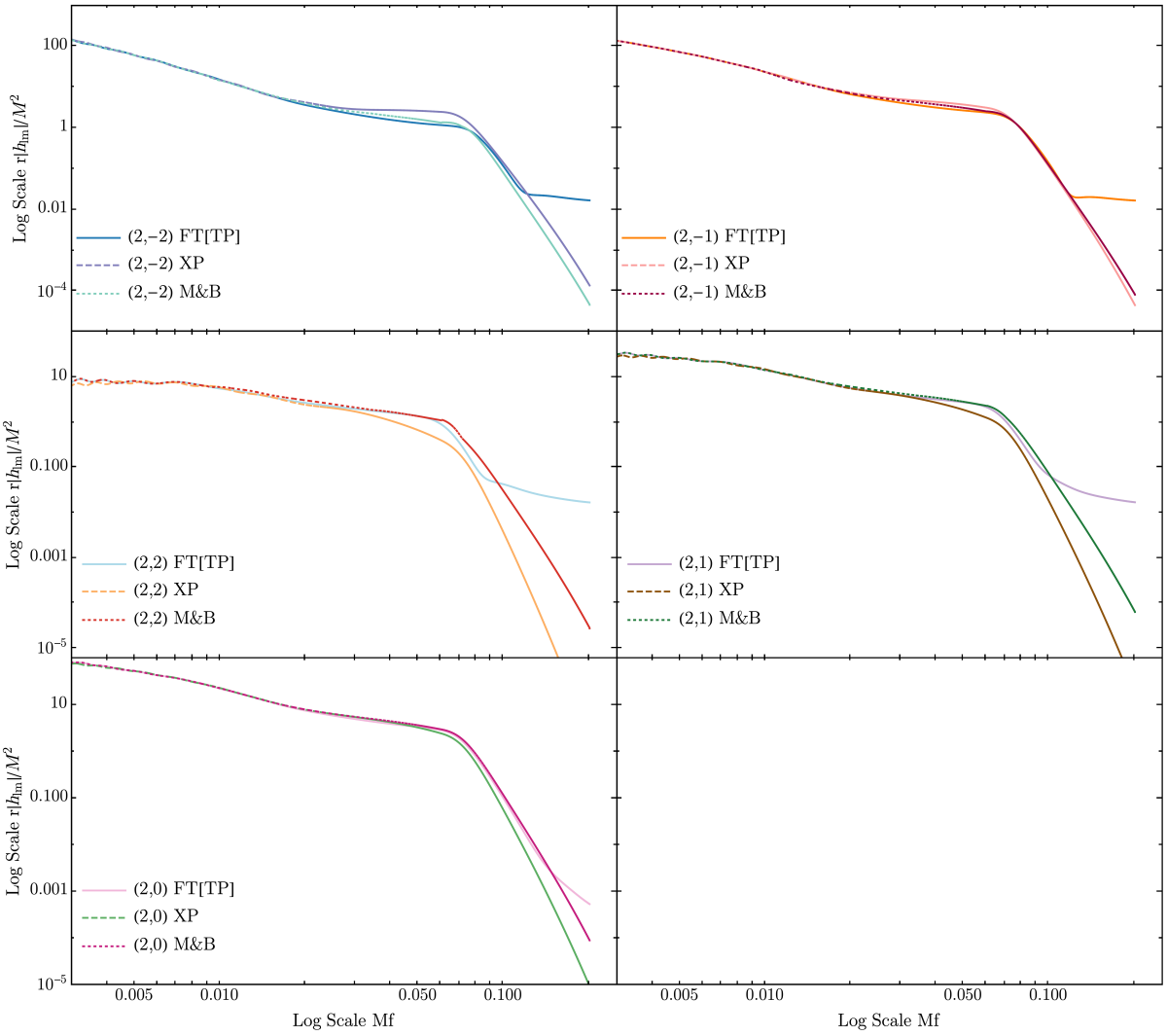

Figure 5.10: Comparison between the inertial J-modes in the positive range of frequencies for TP, XP and M&B. The M&B algorithm has been applied at at second order for the amplitude expansion $A = 2$ and considering three Stencil coefficients $N = 3$ (Case $--$ $A = 2, N = 3$).

In Figure 5.12 we see that the M&B amplitude agrees better with IMRPhenomTP than IMRPhenomXP for most of the waveform evolution up to merger except for the $(2, 2)$ mode, which is affected by the numerical limitations of the numerical derivatives due to its small amplitude. Even though this suggests an enhancement of M&B over IMRPhenomXP, the ringdown has not been modified, which is the main feature to improve in IMRPhenomXP. On the other hand, the phase it is indeed better recovered by M&B. In Figure 5.12.2, one can see that the theoretical ringdown frequency of the prograde $(2, 1)$ is not recovered by the $(2, 1)$ spherical modes, but they are recovering the ringdown frequency of the prograde $(2, 2)$ spheroidal mode. This phenomenon is not due to the beating effect mentioned in Section 4.2, but it is a problem of the MSA

angle description. In order to further develop on this effect see the discussions around Figures 5.15 and 5.16.

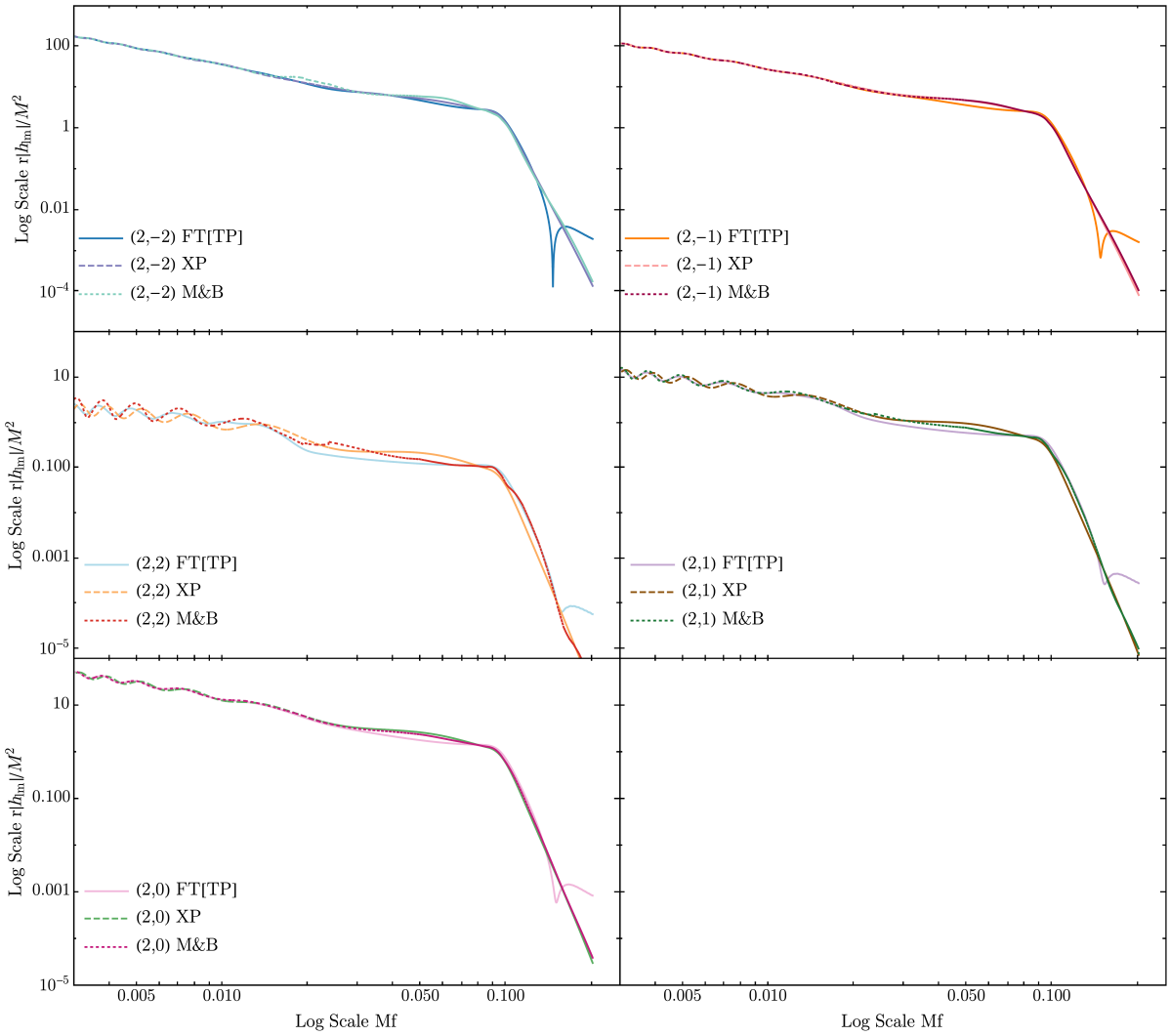

Figure 5.11: Comparison between the inertial J-modes in the positive range of frequencies for TP, XP and M&B. The M&B algorithm has been applied at at second order for the amplitude expansion $A = 2$ and considering three Stencil coefficients $N = 3$ (Case $\perp\perp$ $A = 2, N = 3$).

Nonetheless, the deficiencies of M&B in the Fourier domain for the case $\perp\perp$ shown in Figure 5.11 are transferred to the time domain description, as shown in Figure 5.14. Regarding the amplitude of the different modes, we can see that the performance of M&B for the dominant modes in the positive frequencies does not show any improvement over the SPA, even being worse in this particular case during the late inspiral of the dominant h^I_{2-2} mode. The phase does not seem to be affected by the procedure either, which concludes that the algorithm in this range of the parameter space is not improving IMRPhenomXP. The dependence on the parameter space of the method becomes one barrier to consider the implementation of the algorithm for more formal procedures.

Regarding the Case $--$, which showed the highest disagreement between M&B and IMRPhenomXP in the Fourier domain (Figure 5.10), with M&B closer to IMRPhenomTP, the same is also reflected in the time domain waveform. Indeed, the agreement between M&B and IMRPhenomTP for the mode amplitudes is remarkable

even at merger and the ringdown damping, whereas IMRPhenomXP shows the SPA deficiencies in the recovery of the merger/ringdown features. The phase is also better recovered by M&B than by IMRPhenomXP, specially for the $(2,-1)$ mode, but again we can see that its ringdown frequency does not coincide with the one expected theoretically, obtained through Figure 2.3. Moreover, in this case the differences can be seen both for the dominant and subdominant harmonics, while this case is using the more accurate prescription for the Euler angles. In fact, the problem in this case is due to the *beating* effect we have discussed in Sec. 4.2 and the discussion can be found again around Figures 5.15 and 5.16. The fact that this particular case of antialigned spins shows a clear disagreement between the two Fourier approaches encourages us to perform this same procedure for a simulation of the GW190521 event, done in the following Section 5.1.2. In Figure 4.2 we saw that the IMRPhenomXPHM and IMRPhenomTPHM models show disagreement regarding the effective spin parameter $\chi_{\rm eff}$ (3.3.16), where IMRPhenomXPHM has support for negative values (antialigned spins), but IMRPhenomTPHM does not. Hence, the fact that the $--$ case has shown a substantial difference between IMRPhenomXP and M&B motivates a simulation of the antialigned case where IMRPhenomXPHM has support but IMRPhenomTPHM does not, in order to see which is the behaviour of the M&B algorithm.

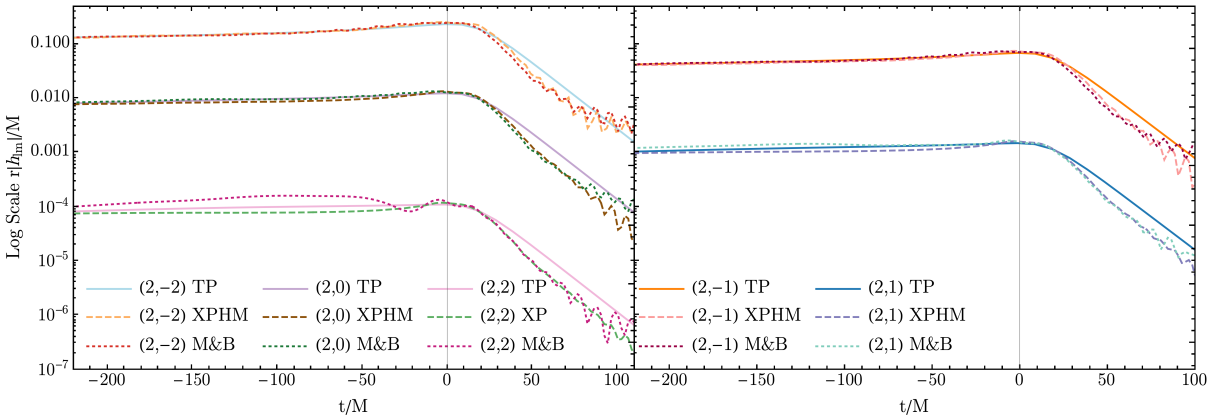

5.12.1: Amplitude.

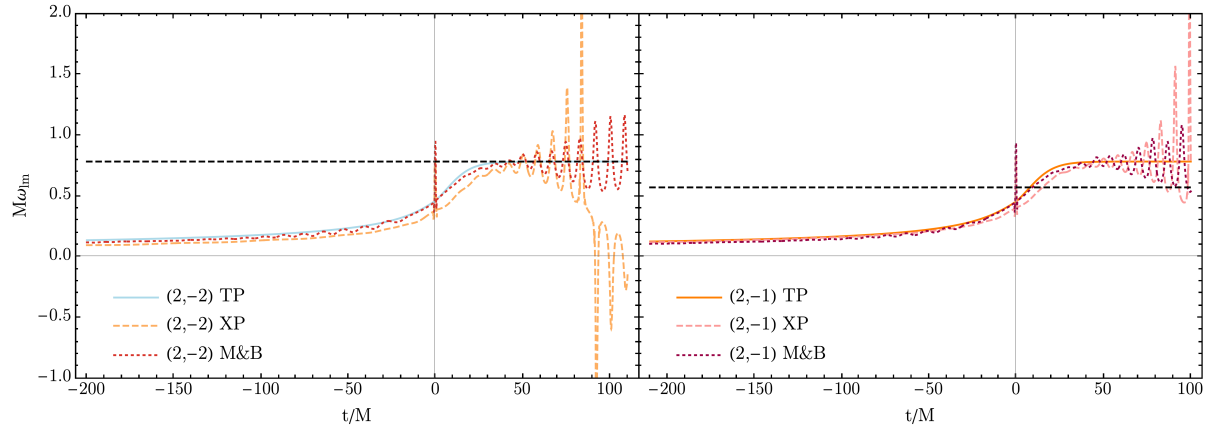

5.12.2: Phase derivative of the dominant modes. The dashed black lines correspond to the ringdown frequencies of the *prograde spheroidal modes* $\omega_{22}^{\rm RD}$ and $\omega_{21}^{\rm RD}$ in the left and right panels, respectively.

Figure 5.12: Comparison of the modes shown in Figure 5.9 in the time domain. For the modes of XP and M&B, a tapering window has been applied to the positive range of frequencies in order to compare exclusively that contribution to the complete waveform: the correspondence to TP. Case $++$ in Table 5.1.

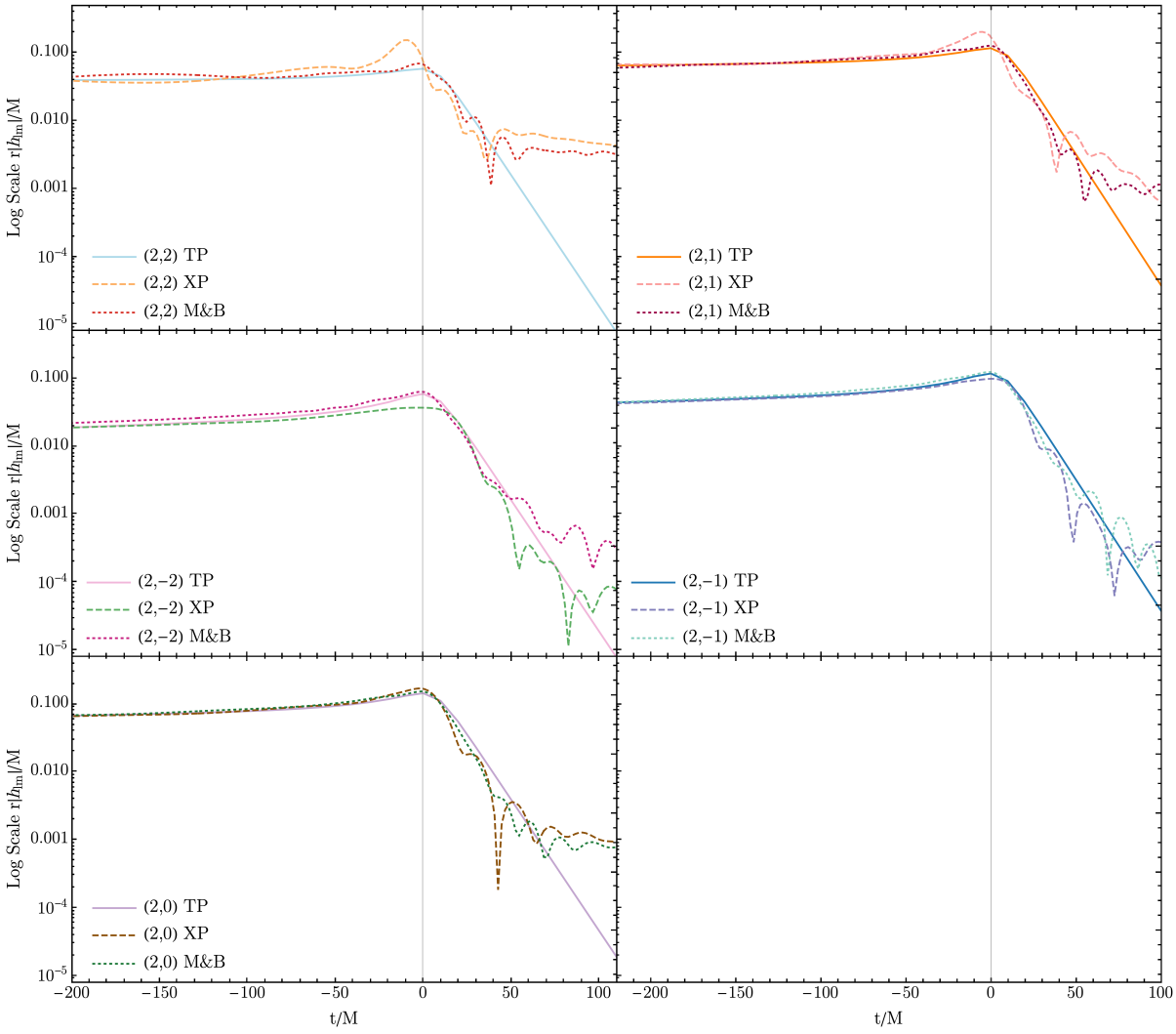

5.13.1: Amplitude.

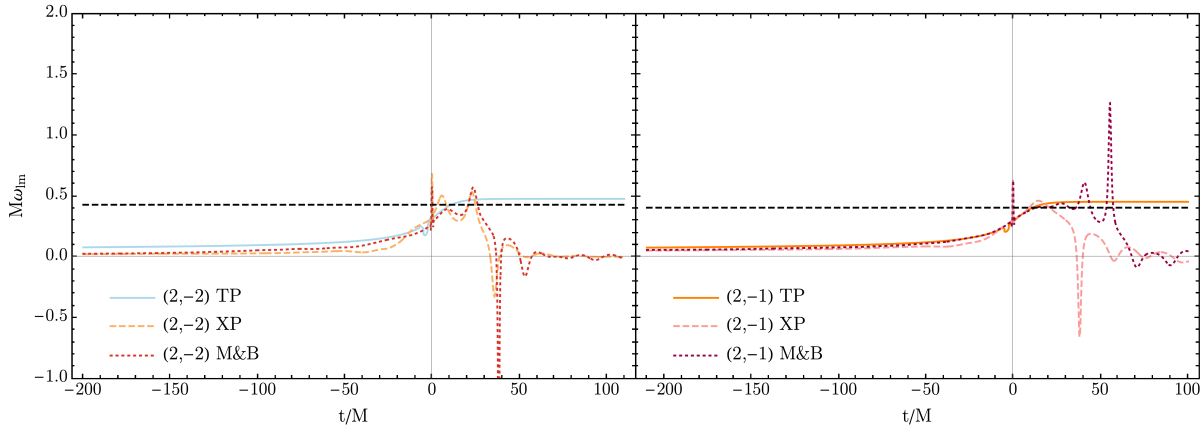

5.13.2: Phase derivative of the dominant modes. The dashed black lines correspond to the ringdown frequencies of the *prograde spheroidal modes* $\omega_{22}^{\mathrm{RD}}$ and $\omega_{21}^{\mathrm{RD}}$ in the left and right panels, respectively.

Figure 5.13: Comparison of the modes shown in Figure 5.10 in the time domain. For the modes of XP and M&B, a tapering window has been applied to the positive range of frequencies in order to compare exclusively that contribution to the complete waveform: the correspondence to TP. Case −− in Table 5.1.

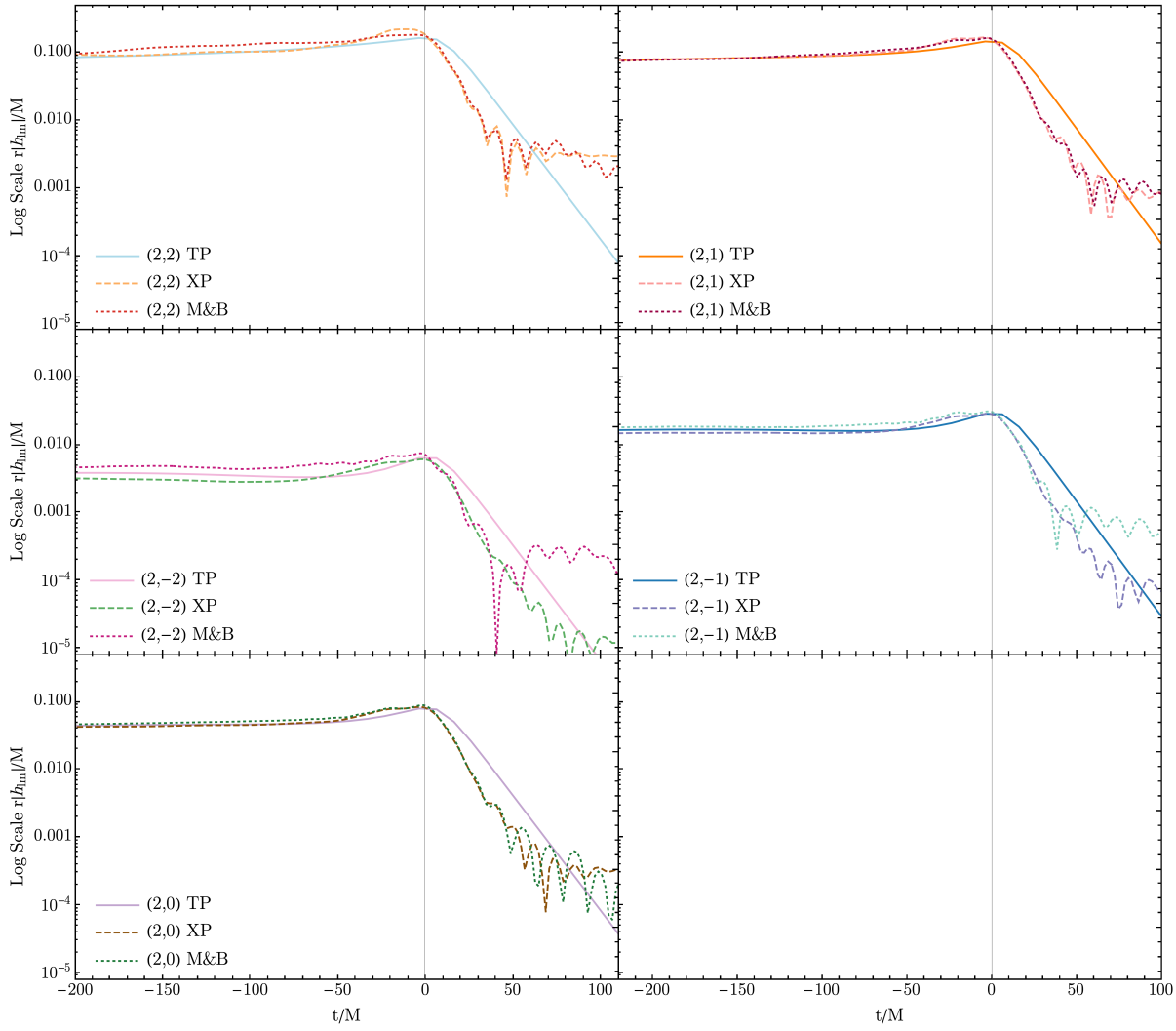

5.14.1: Amplitude.

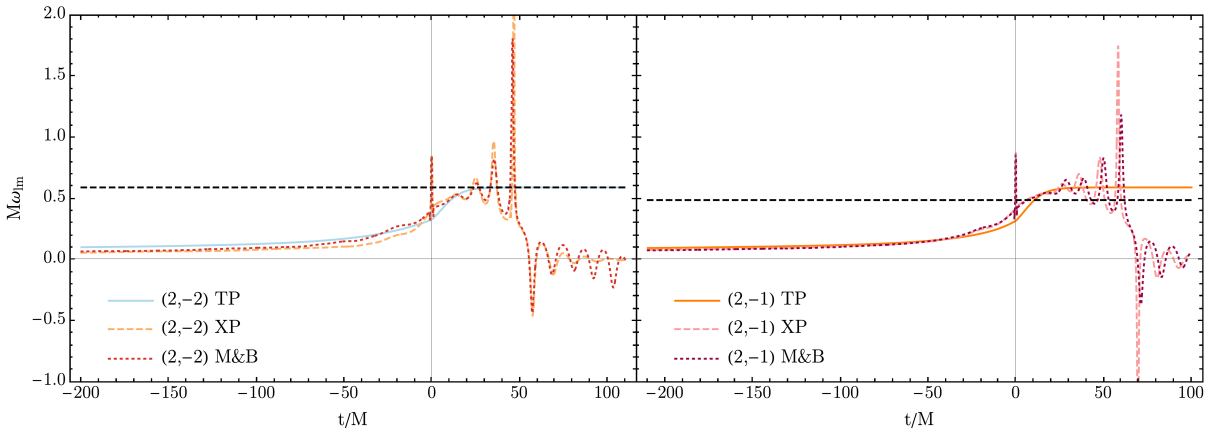

5.14.2: Phase derivative of the dominant modes. The dashed black lines correspond to the ringdown frequencies of the *prograde spheroidal modes* $\omega_{22}^{\mathrm{RD}}$ and $\omega_{21}^{\mathrm{RD}}$ in the left and right panels, respectively.

Figure 5.14: Comparison of the modes shown in Figure 5.11 in the time domain. For the modes of XP and M&B, a tapering window has been applied to the positive range of frequencies in order to compare exclusively that contribution to the complete waveform: the correspondence to TP. Case $\perp\perp$ in Table 5.1.

In the previous time domain Figures 5.12-5.14 we have seen that the spherical modes are not recovering the ringdown frequencies of the prograde modes. These quasinormal modes are excited due to the aligned component of the final spin, whereas the retrograde modes are excited due to the antialigned component. Hence, depending on the value of the β angle during the ringdown, one or both of these modes will get excited. If β is close to 0, then only the prograde modes will be excited, for $\beta \approx \pi$, the retrograde, and a mix of them for $\beta \approx \pi/2$. Looking at the Euler angles' evolution for the three cases (Figure 5.1), we see that β in the case $--$ achieves a value close to $\pi/2$ at the ringdown, which implies that in this case the *spherical modes* may suffer from beating, and show a ringdown frequency close to the mean between the prograde and retrograde frequencies. However, the ringdown frequency of the $(2,-1)$ mode in the case $++$ was not recovering the $(2,1)$ prograde frequency, while in Fig. 5.1 we can see that β takes only positive and low values, which is consistent with the excitation of only the prograde quasinormal modes. Let's discuss now these two cases in detail.

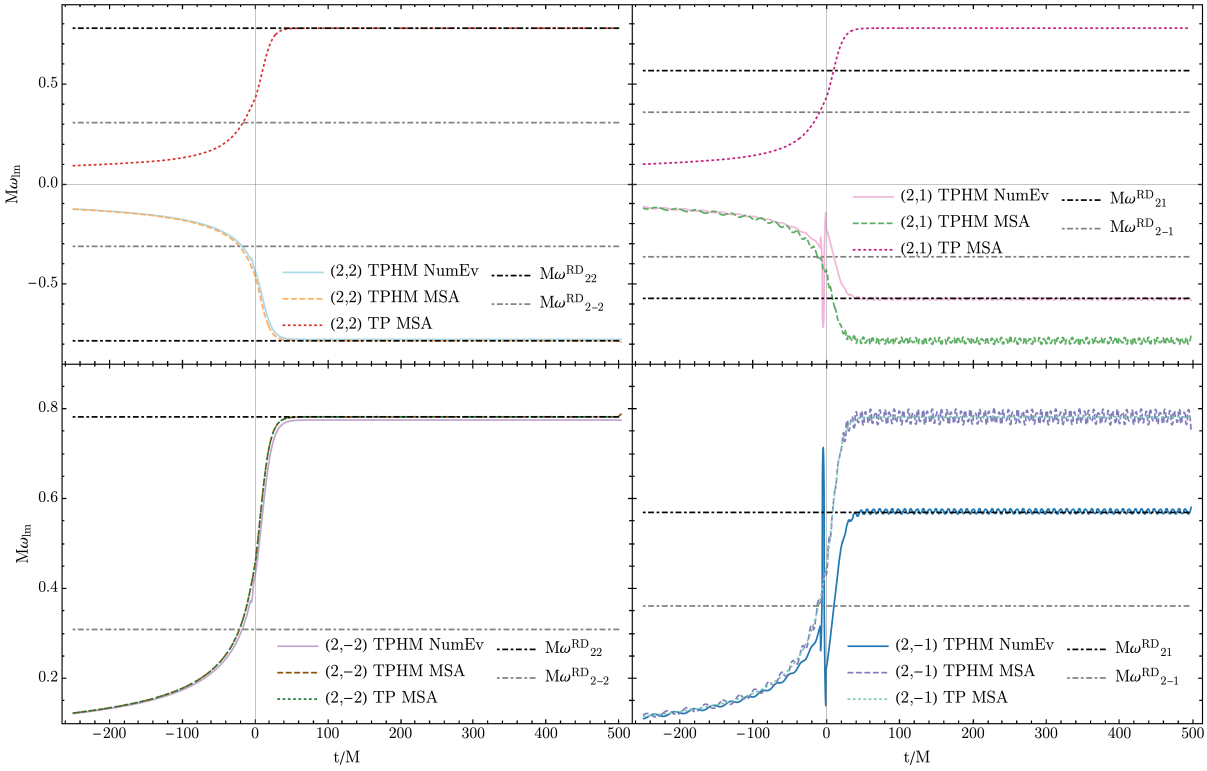

Figure 5.15: Frequencies of the spherical harmonic modes for the case $++$, using IMRPhenomTPHM, which includes the dominant contributions, with the MSA angles (the prescription used for the case $++$), using IMRPhenomTP, which is the contribution of the positive frequency range waveform, and IMRPhenomTPHM using the numerical angles, which is a more reliable prescription. The horizontal lines are the ringdown frequencies of both the prograde and retrograde quasinormal frequencies.

In Figure 5.15 we can see the comparison between the frequencies of the IMRPhenomTPHM modes computed by the MSA angles, which have been used in this case, the IMRPhenomTP used for the comparison, and finally the numerical angles obtained from the direct evolution of the spin equations. Note that IMRPhenomTP only includes the contribution of the $h^{\rm cop}_{2-2}$ mode in the coprecessing frame, which corresponds to a very small

contribution to the $(2, m > 0)$ modes. Hence, the frequency of the IMRPhenomTP modes have always the same sign as the $h^{\rm cop}_{2-2}$, which is positive, and takes the same absolute value for the ringdown frequency than the corresponding $(2, m > 0)$ mode. As previously mentioned, the numerical angles have more physical information than the MSA angles, but they have also a more challenging evolution, which is not optimal for the M&B procedure. However, as can be seen in the right panels of Figure 5.15, this prescription does recover the ringdown frequency of the $(2, 1)$ prograde mode, which is what we expected from the β evolution. Therefore, the MSA angles are not reproducing the physical information of one of the modes, but it is compensated by a smooth evolution of the frequency at merger. We used then these angles because in this Section we wanted to test the performance of M&B for a given set of angles, independently of their reliability but instead promoting its smooth evolution. This is not however the case for the case $--$, as can be seen in Figure 5.16.

In Figure 5.16 we have included again the IMRPhenomTPHM and IMRPhenomTP modes computed with the Euler angles used in this case, which are the ones obtained from the spin evolution equations, and then the IMRPhenomTPHM computed from the MSA angles, in order to see the performance of smoother angles. As we pointed out above, in this case the β angle takes a value close but higher than $\pi/2$, which implies that both the prograde and retrograde modes are excited, and hence, there is beating between these two ringdown frequencies. A value higher than $\pi/2$ implies that the spin flips over and hence, the frequencies also change the sign. This effect is only seen however in the IMRPhenomTPHM modes computed from the numerical angles: IMRPhenomTP corresponds to a unique contribution of the IMRPhenomTPHM complete modes, whereas the MSA angles do not contain the underlying physics during the latest stage of the binary. Unlike for Figure 5.15, one can not determine the ringdown frequencies of the (l, m) modes directly from Figure 5.16.1 due to the strong beating effect between the prograde and retrograde frequencies. Focusing on the modes computed from the numerical angles, we can determine their ringdown frequency by looking directly at the phase slope during the ringdown. Once we have adjusted the $(l, \pm m)$ mode phases so they all have positive slope during the ringdown and phase equal to 0 at merger, we can see in Figure 5.16.2 the effect we expected: the frequencies of the $(l, \pm m)$ spherical modes have the same ringdown frequency, which corresponds to a value in between the prograde and retrograde components of the quasinormal modes excited. For the $(2, |2|)$ modes it turns out that the slope is approximately the mean value of the prograde and retrograde contribution, which means that both modes have been equally excited, while the $(2, |1|)$ modes show a ringdown frequency closer to the prograde contribution, but still in between both contributions.

This discussion can be now extended to the other cases we treat in this work, and the difference between the ringdown frequencies of the prograde modes and the spherical harmonic modes can be due to three factors. First, it can be from the failure of the angle prescription used, associated to the MSA angles. In the second place it may happen because of the phenomenon of beating, which is particularly relevant for configurations with negative spins. Finally, one should take into account that here IMRPhenomTP corresponds to only one contribution of the complete sum of the IMRPhenomTPHM modes. Hence, the phase associated to that mode may not recover the final value, when all the contributions have been added.

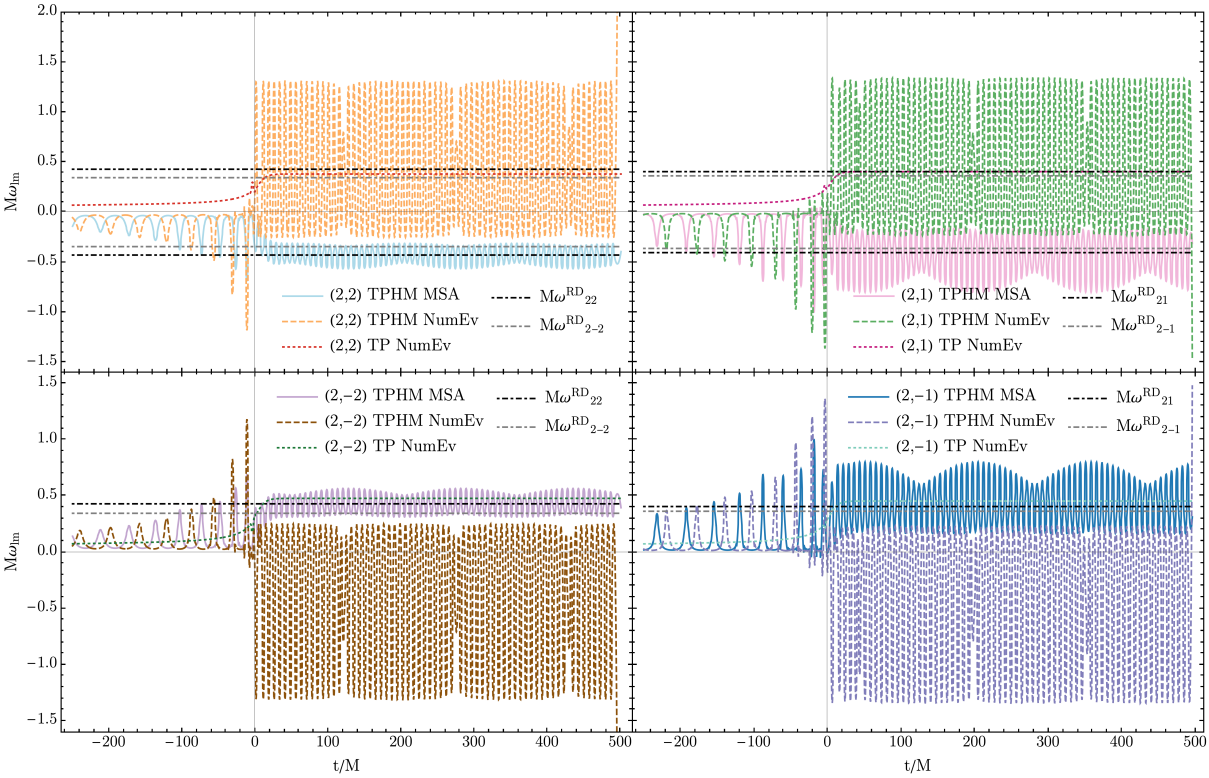

5.16.1: Frequencies of the spherical harmonic modes for the case $++$, using IMRPhenomTPHM, which includes the dominant contributions, with the numerical angles (the prescription used for the case $--$), using IMRPhenomTP, which is the contribution of the positive frequency range waveform, and IMRPhenomTPHM using the MSA angles, which show a smoother evolution. The horizontal lines are the ringdown frequencies of both the prograde and retrograde quasinormal frequencies. The numerical evolution of the angles show a flip at merger because the angle β becomes higher than $\pi/2$.

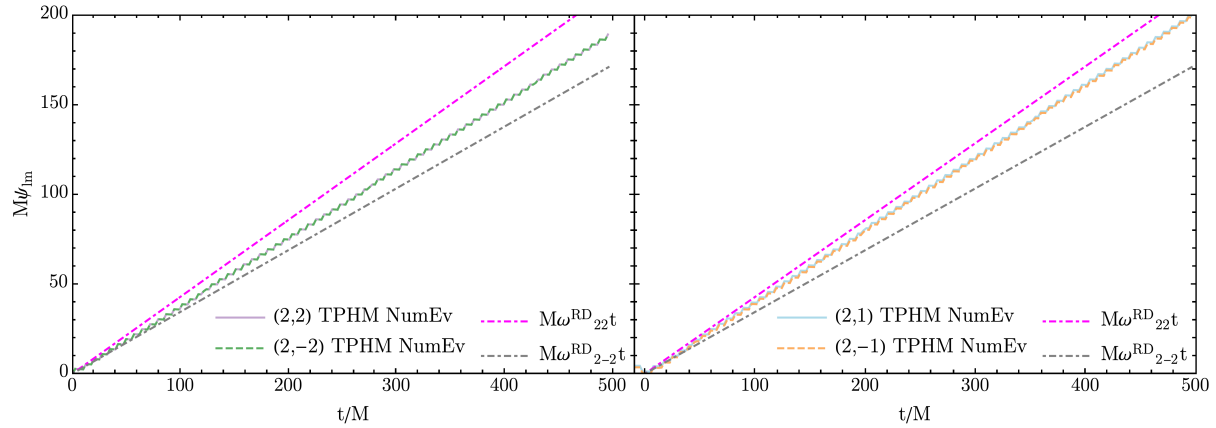

5.16.2: Plot to determine directly the ringdown frequencies of the IMRPhenomTPHM using the numerical angles in Figure 5.16.1 as the slope of the mode phase during the ringdown stage. The phase for the (l, m) spherical modes has been modified in order to have positive slope and have null phase at the merger time. Note that the slopes for the $(l, \pm m)$ modes overlap. In this plot we can see the "beating" phenomenon.

Figure 5.16: Further discussion of the frequencies of the harmonic modes in the case $--$.

5.1.2 GW190521

According to Figure 4.2, for massive binaries where only the last cycles around merger can be observed, the inaccuracies of the SPA may lead to biases in parameter estimation. For this cases, it is expected that time domain models that do not depend on this approximation provide more accurate results. The masses and spins chosen to represent values consistent with GW190521 in Table 5.1 correspond to $\chi_{\rm eff} = -0.43$ and $\chi_p = 0.67$, which fall in the more likely range for IMRPhenomXPHM but not for IMRPhenomTPHM, as seen in Figure 4.2 or Table III in Ref. [52], our extensive comparison paper.

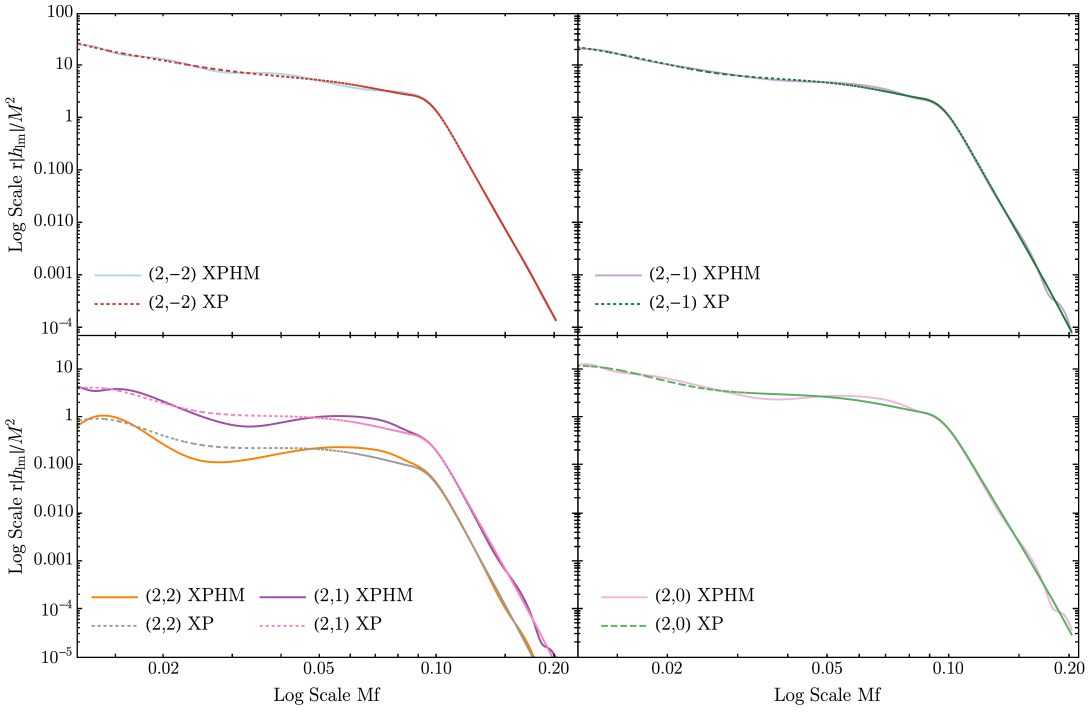

5.17.1: Comparison in the positive frequencies between XPHM/XP.

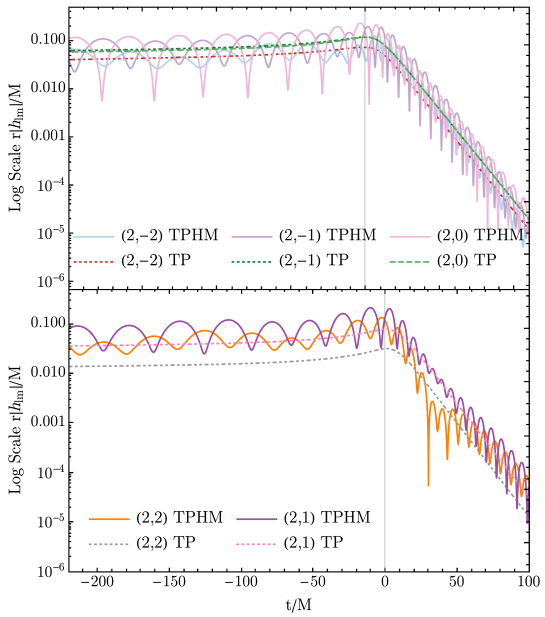

5.17.2: Comparison between TPHM and TP.

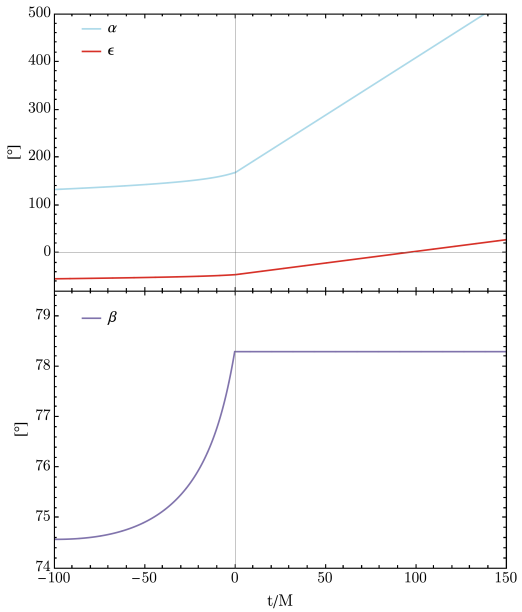

5.17.3: Angles obtained via the numerical evolution of the spin equations.

Figure 5.17: Simulation of the GW190521 event, case GW190521 in Table 5.1.

Following the same structure as in Section 5.1.1, Figure 5.17 shows the evolution of the Euler angles used to perform the twisting up and the comparison between including the higher mode contribution or not in both the time and frequency domain. In the bottom paner of Figure 5.17.3, it can be seen one of the caveats of the numerical evolution of the β angle during the ringdown, which saturates at a constant value. This will be revisited in future upgrades of the model [100]. We can now perform M&B at lowest order and using $A = 2$ and $N = 3$, results shown in Figures 5.18 and 5.19 respectively.

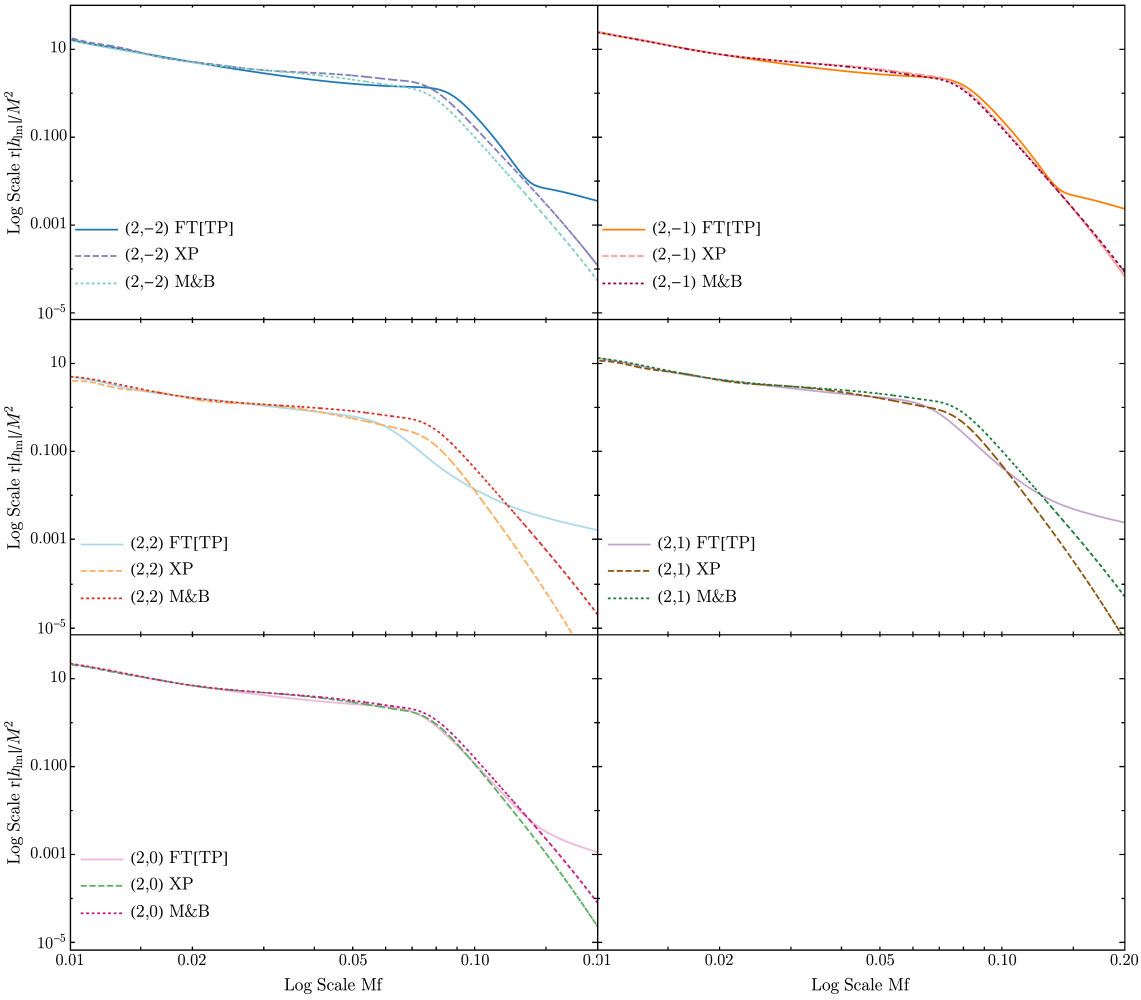

Figure 5.18: Comparison between the inertial J-modes for positive frequencies of TP, XP and M&B. The M&B algorithm has been applied at lowest order for both the amplitude and the stencil expansion (Case GW190521 $A = N = 0$).

Whereas Figure 5.18 suggests that IMRPhenomXP is closer to IMRPhenomTP than the results from the M&B algorithm, results shown in Figure 5.19 are indeed similar to those obtained for $--$ in Figure 5.10. Except for the lowest contribution (the $(2, 2)$ mode in the positive range of frequencies), the M&B procedure recovers better IMRPhenomTP both during the inspiral and the final slope. Moreover, this agreement is magnified if we compare the methods in the time domain, in Figure 5.20. Although far from perfect, the match between M&B and IMRPhenomTP becomes much better than it does for IMRPhenomXP, especially for the merger peak and the following ringdown, which is the main problematic part for the SPA. The same behaviour can be seen in the phase derivative plots: M&B is recovering IMRPhenomTP, whereas IMRPhenomXP does

not. Although one cannot make a strong statement just using this rough comparison, it seems to suggest that in these cases, where only the last few cycles are detected, IMRPhenomXPHM can indeed lead to inaccuracies in the parameter estimation due to the underlying SPA, which fails at this stage.

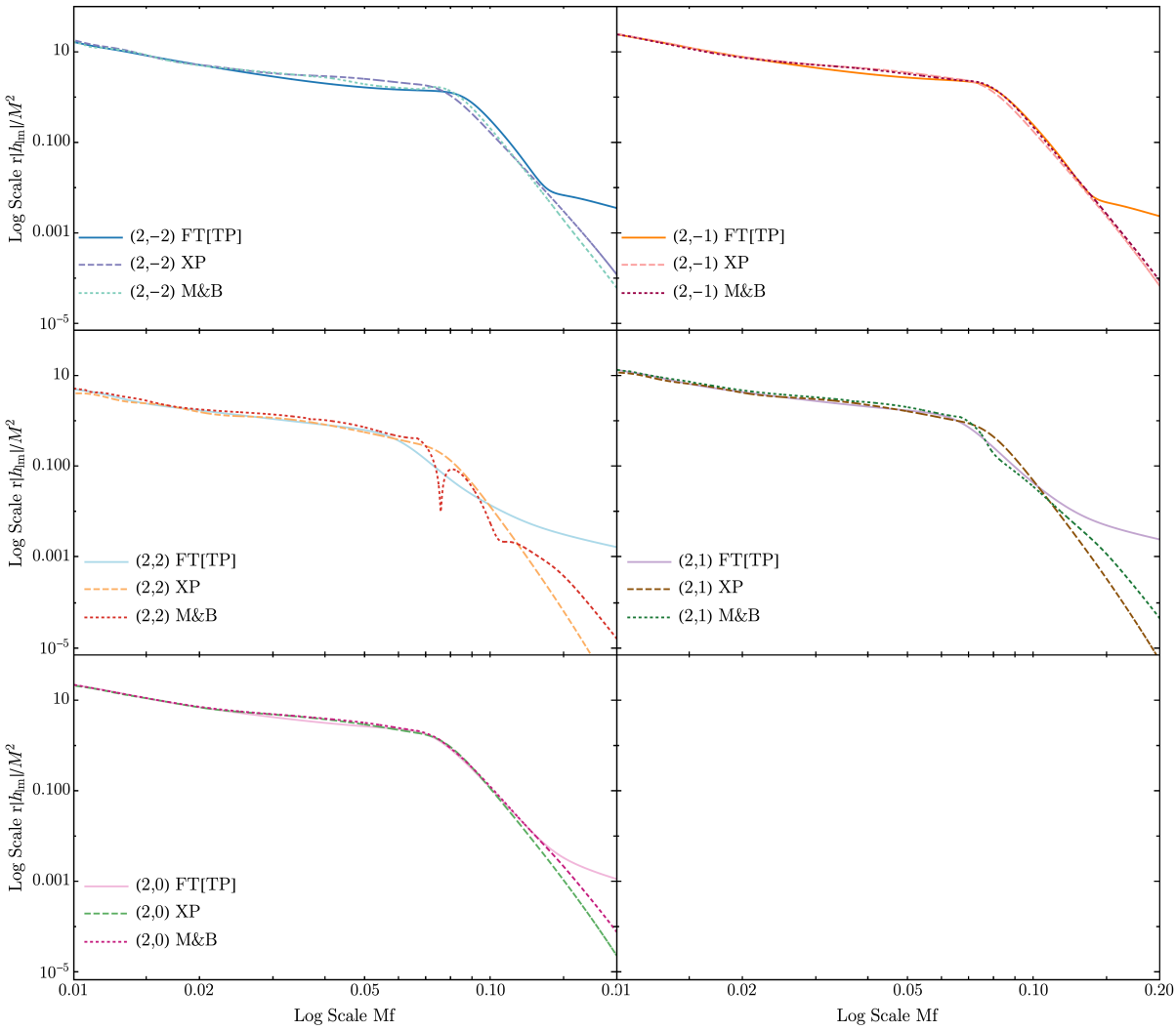

Figure 5.19: Comparison between the inertial J-modes in the positive range of frequencies for TP, XP and M&B. The M&B algorithm has been applied at at second order for the amplitude expansion $A = 2$ and considering three Stencil coefficients $N = 3$ (Case GW190521 $A = 2, N = 3$).

Once we have discussed the behaviour of the M&B algorithm for the simplest case in which only the dominant harmonics and their contribution in the positive frequencies are considered, we can now proceed to test it when considering higher modes. This way, it is reasonable to compare the M&B results with the complete models IMRPhenomXPHM and IMRPhenomTPHM, and determine their accuracy when reproducing a NR simulation. This has been done in Section 5.2.

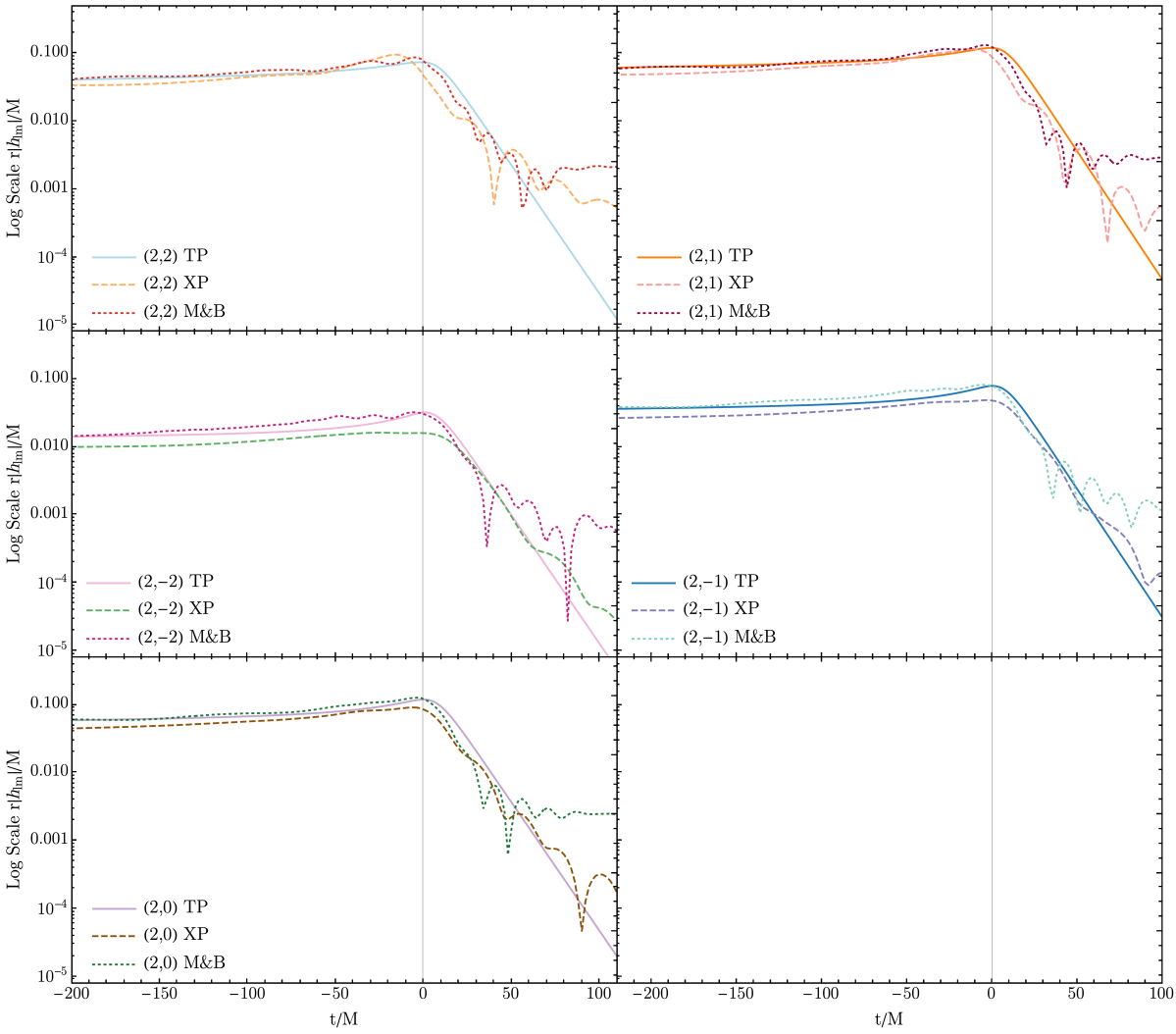

5.20.1: Amplitude.

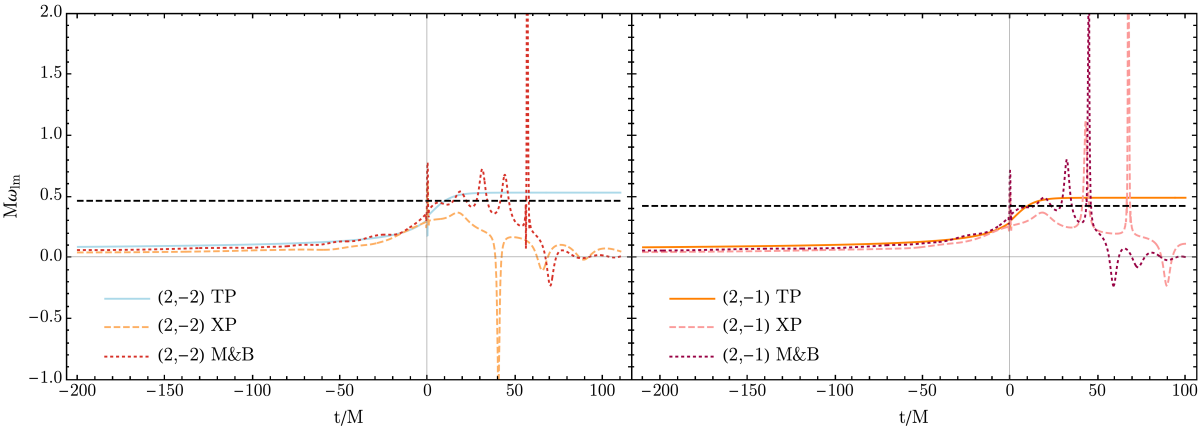

5.20.2: Phase derivative of the dominant modes. The dashed black lines correspond to the ringdown frequencies of the *prograde spheroidal modes* $\omega_{22}^{\mathrm{RD}}$ and $\omega_{21}^{\mathrm{RD}}$ in the left and right panels, respectively.

Figure 5.20: Comparison of the modes shown in Figure 5.19 in the time domain. For the modes of XP and M&B, a tapering window has been applied to the positive range of frequencies in order to compare exclusively that contribution to the complete waveform: the correspondence to TP. Case GW190521.

5.2 Full twisting up: SXS:BBH:0037

In this last Section we will include the results obtained using the M&B algorithm taking into account the contribution of the higher modes in the coprecessing frame for $l = 2$, i.e. we will perform the sum Eq. (4.3.27) for $m' = -1, -2$. Results will be compared with IMRPhenomXPHM and IMRPhenomTPHM for the simulation of the NR waveform SXS:BBH:0037 [129], whose parameters can be found in Table 5.1. Figure 5.21.2 shows the Euler angles used to obtain the modes in the inertial J-frame both for the NR waveform and TPHM, which are compared in Figure 5.21.1. Note that in the time domain, the positive and negative modes look very similar in this case both for IMRPhenomTPHM and NR: whereas the phenomenological models do not consider asymmetries between the $(l, \pm m)$, NR simulations do, although in this case they can be practically neglected. Due to the very weak and noisy contribution of the $(2, 0)$ mode we will not take it into account here for comparisons.

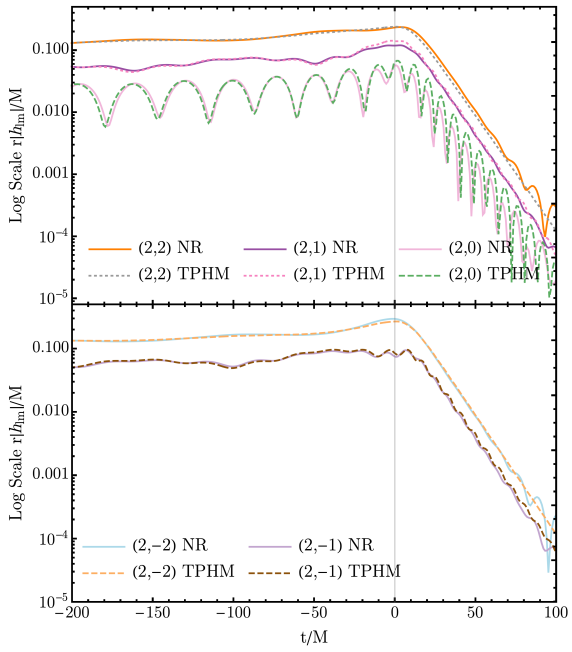

5.21.1: Time domain modes in the inertial J-frame of the NR precessing simulation SXS:BBH:0037 and its representation through IMRPhenomTPHM.

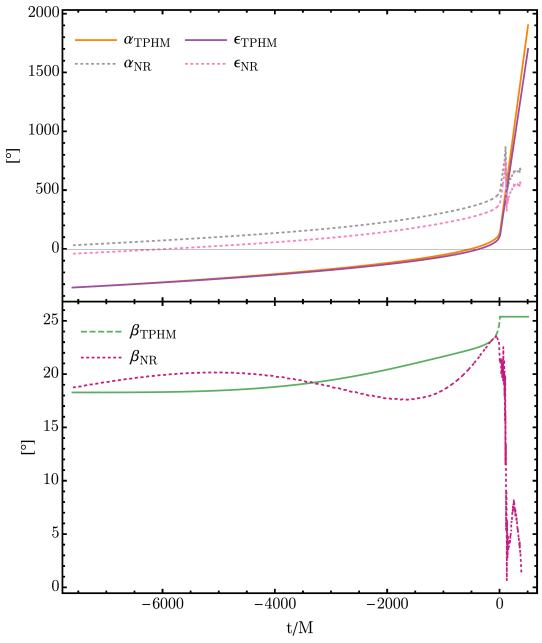

5.21.2: Comparison of the three Euler angles. NR: computed by quadrupole alignment. TPHM: computed by the evolution of the spin equations.

Figure 5.21: Simulation of the NR event SXS:BBH:0037. The angles shown in Fig. 5.21.2 rotate the co-precessing waveform to the waveform in the inertial J-frame shown in Figure 5.21.1.

The frequency domain comparison of the direct FFT of the modes shown in Figure 5.21.1 together with the IMRPhenomXPHM modes can be found in Figure 4.1. Note that there we included the support of the different modes for all the range of frequencies, showing the correspondence between $(l, \pm m)$ modes. We can see that except for the dominant contribution of the $(2, |2|)$ modes, IMRPhenomXPHM showed disagreement with the FFT of the time domain waveforms. We will now show the results after performing the M&B algorithm using the two angles prescriptions shown in Figure 5.21.2. Figures 5.22 and 5.23 show the results in the Fourier domain obtained using the IMRPhenomTPHM angles and the NR computed from the quadrupole alignment, respectively.

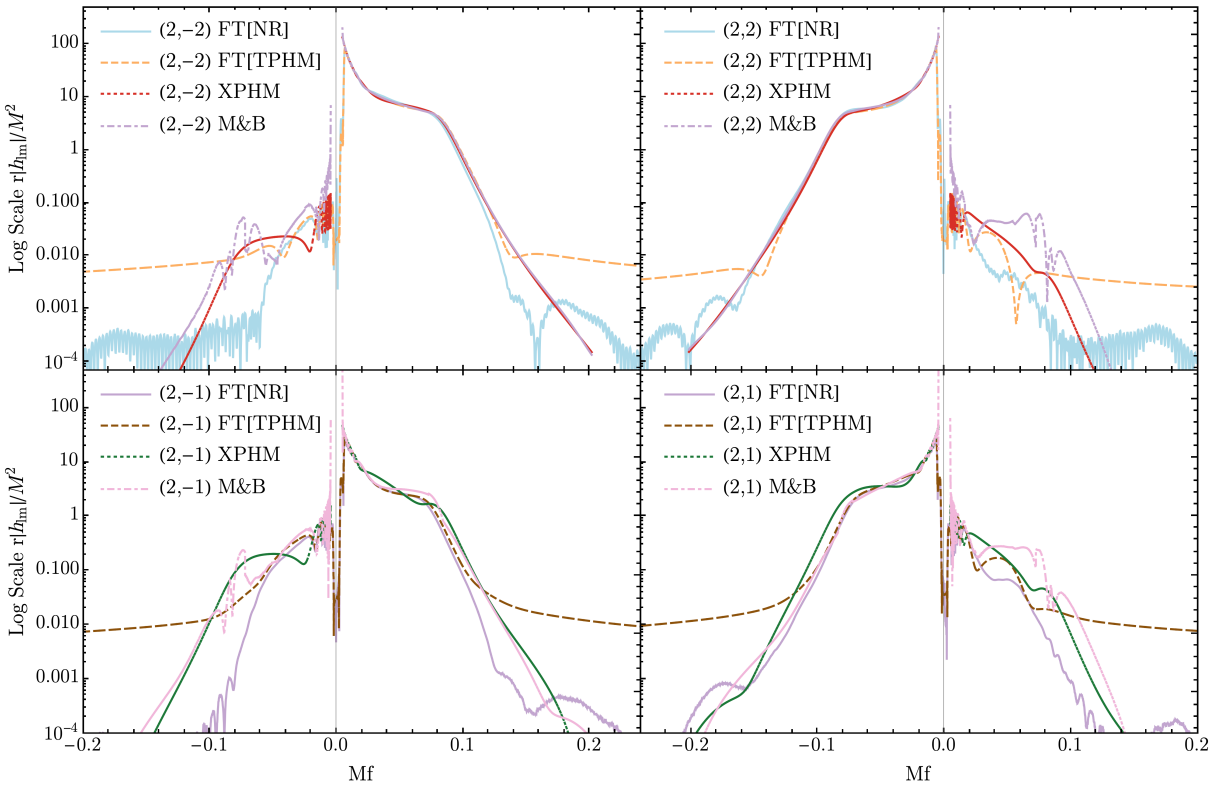

5.22.1: Complete representation of the waveform.

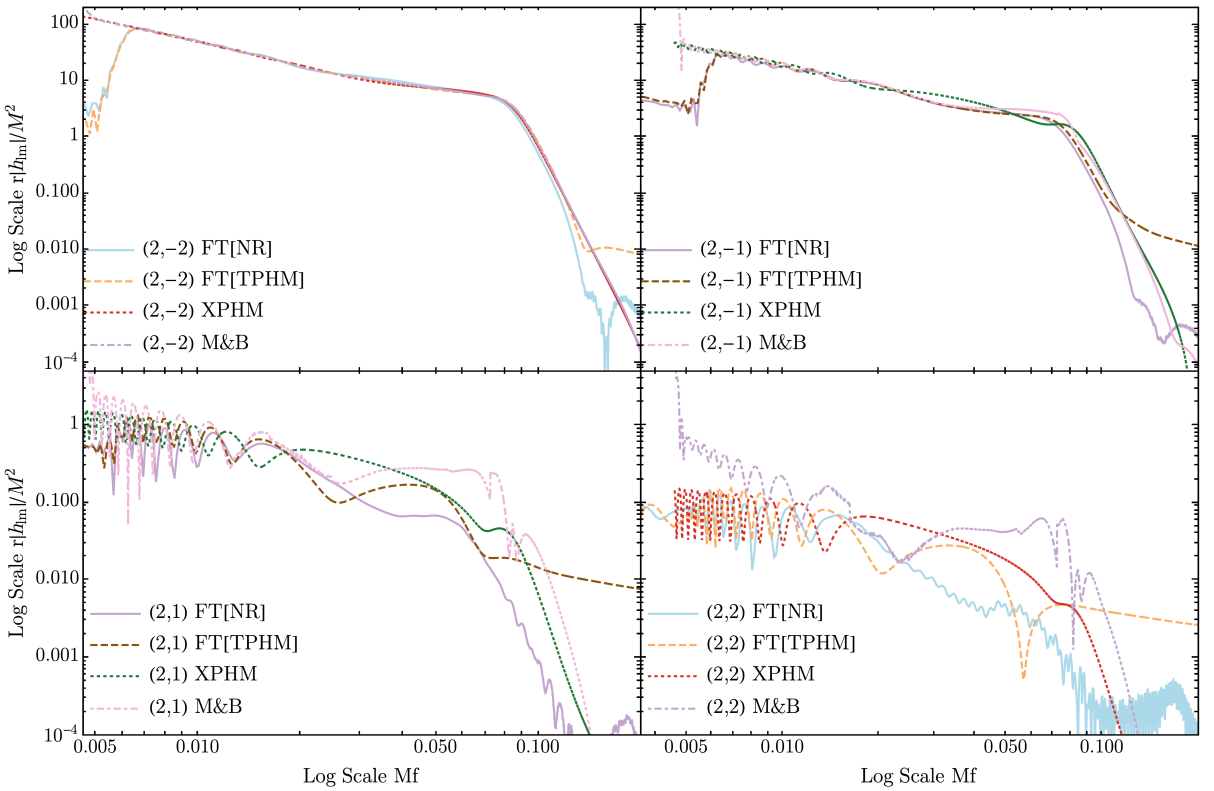

5.22.2: Log log scale representation of the positive range of frequencies for all the modes.

Figure 5.22: Results obtained through the M&B implementation with $N = 3$ and $A = 2$ using the IMRPhenomTPHM angles shown in Figure 5.21.2. The plots include the results obtained via the FFT of the NR and the IMRPhenomTPHM waveforms and also the IMRPhenomXPHM waveform for all the range of frequencies.

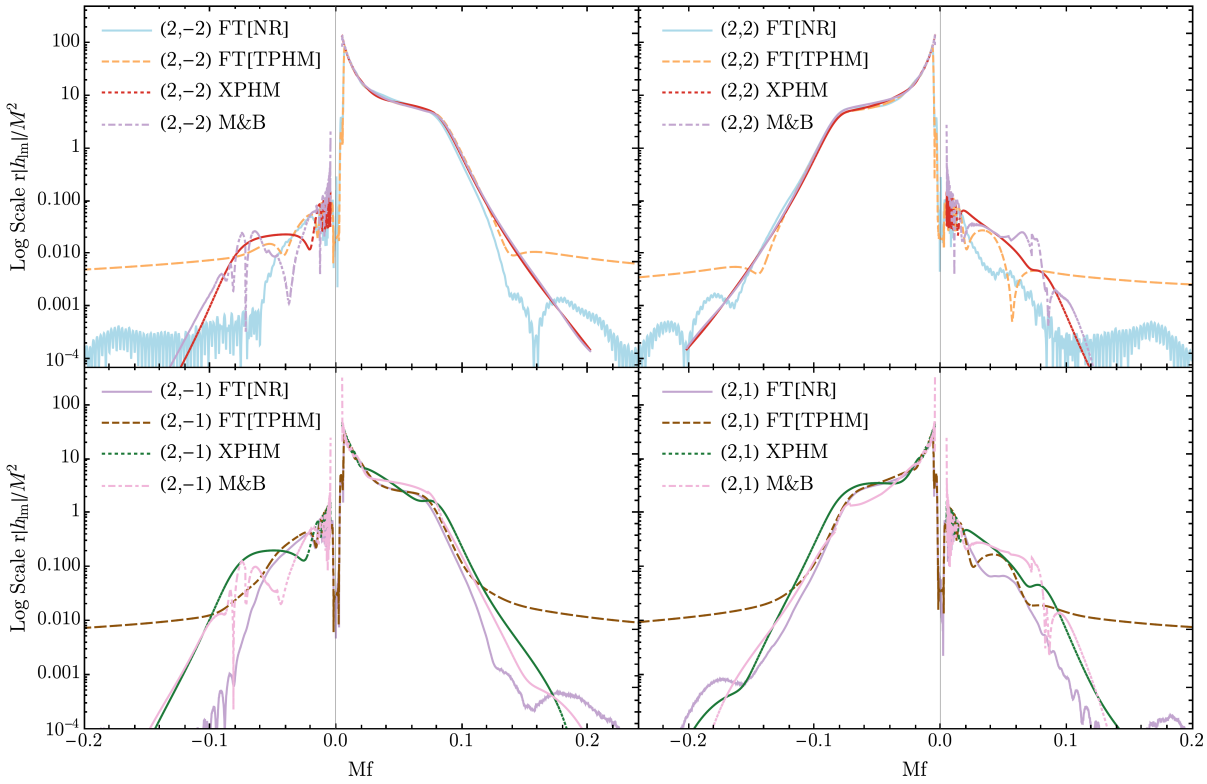

5.23.1: Complete representation of the waveform.

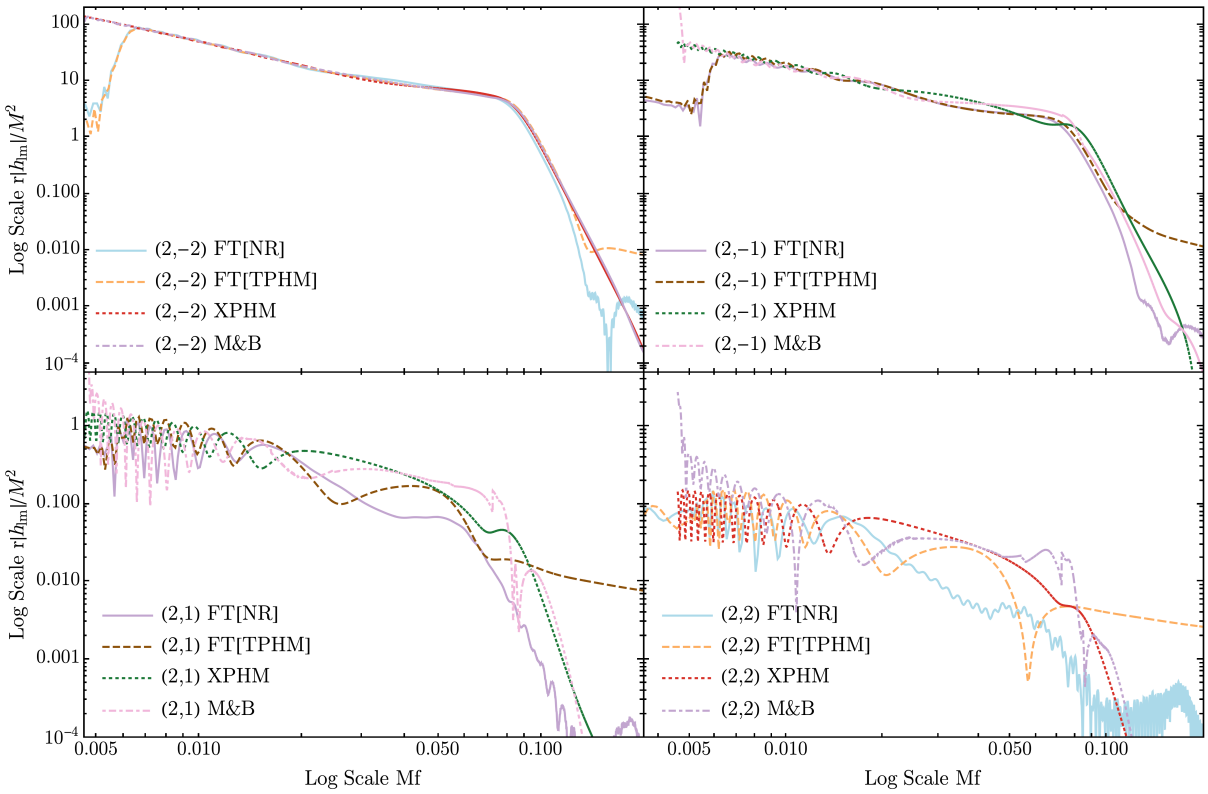

5.23.2: Log log scale representation of the positive range of frequencies for all the modes.

Figure 5.23: Results obtained through the M&B implementation with $N = 3$ and $A = 2$ using the NR angles shown in Figure 5.21.2. The plots include the results obtained via the FFT of the NR and the IMRPhenomTPHM waveforms and also the IMRPhenomXPHM waveform for all the range of frequencies.

Figures 5.22 and 5.23 show very similar results, although the M&B approach for the TPHM angles is less noisy due to the complete geometric description of the quadrupole alignment method for the NR angles. However, we can see in both plots that the stronger contributions (in the positive frequencies for $m < 0$ modes and in the negative range for $m > 0$) are better recovered by the M&B algorithm. Indeed, even though IMRPhenomXPHM already captures the $(2, |2|)$ modes, which are the dominant ones, it fails for the $(2, |1|)$ modes, while M&B recovers a more accurate result during the complete evolution. Regarding the weaker contributions of the modes (negative frequencies for $m < 0$ modes and positive for $m > 0$) it is difficult to determine the enhancement of M&B. Although at lower frequencies it does capture better the evolution than IMRPhenomXPHM, the results are too noisy to conclude if it implies an improvement or not. Moreover, those contributions are at the limit of the noise associated with the FFT, which makes it harder to make any statement. In any case, the different models show the same order of magnitude, which is already remarkable due to the very low amplitude. In Figures 5.22.2 and 5.23.2 one can see the details in a log-log plot of the different mode contributions in the positive frequency range. We can now discuss the results in the time domain, shown in Figures 5.24 and 5.25 for the TPHM and NR angles, respectively.

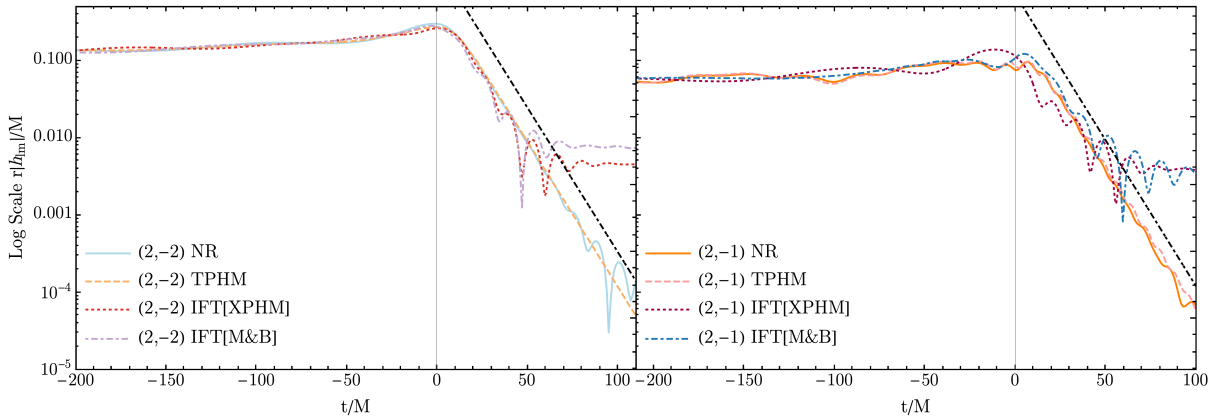

5.24.1: Amplitude. The black dot-dashed lines correspond to the damping frequency of the $(2, 2)$ and $(2, 1)$ spheroidal modes.

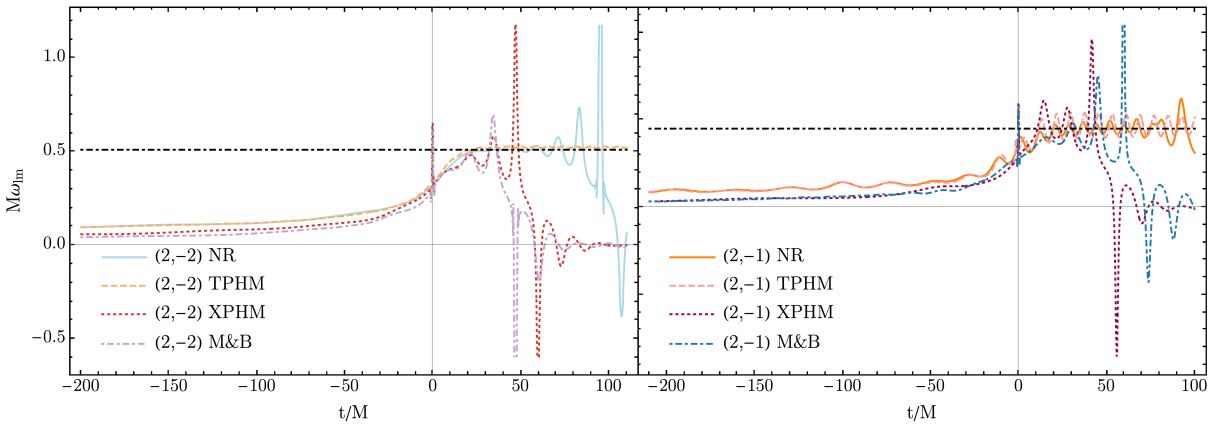

5.24.2: Phase derivative of the dominant modes. The dashed black lines correspond to the ringdown frequencies of the *prograde spheroidal modes* $\omega_{22}^{\mathrm{RD}}$ and $\omega_{21}^{\mathrm{RD}}$ in the left and right panels, respectively.

Figure 5.24: Time domain representation of the negative modes shown in Figure 5.22. The inverse Fourier transform for IMRPhenomXPHM and M&B has been computed only for the positive frequencies, since the negative contribution can be neglected.

Due to the symmetry between the $(l, |m|)$ modes in the time domain, as seen in Figure 5.21.1, and the very weak contribution in the negative frequencies of the $(l, -m)$ modes (Figures 5.22 and 5.23), the time domain modes for IMRPhenomXPHM and M&B have been obtained applying an inverse Fourier transform to the $(2, -2)$ and $(2, -1)$ modes in the positive frequency range. Figures 5.24 and 5.25 show the same features seen in the Fourier domain comparisons: even though the difference between IMRPhenomXPHM and M&B for the dominant $(2, -2)$ mode is not noticeable, the effect on the higher harmonic $(2, -1)$ of the M&B algorithm with respect to the SPA seems to modify the waveform in the right direction, and hence it captures with higher agreement both the merger and ringdown damping.

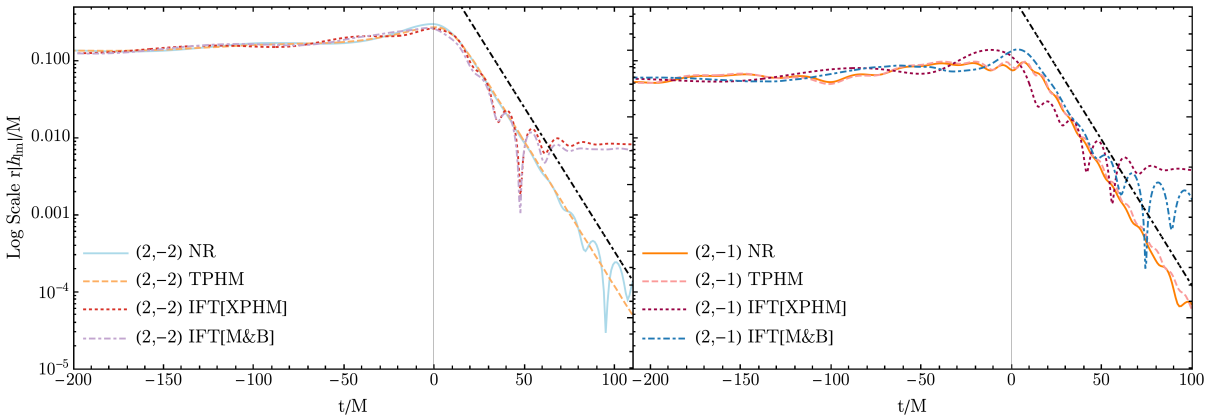

5.25.1: Amplitude. The black dot-dashed lines correspond to the damping frequency of the $(2, 2)$ and $(2, 1)$ spheroidal modes.

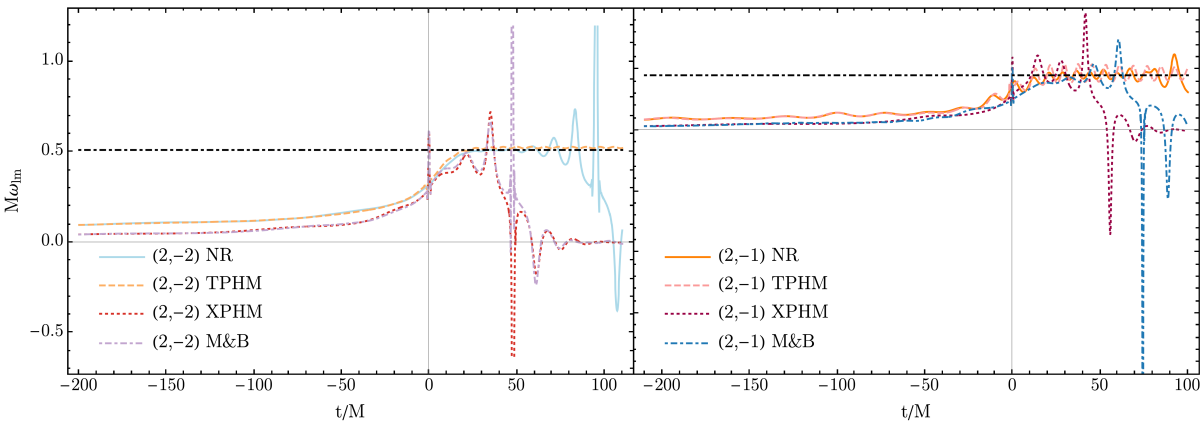

5.25.2: Phase derivative of the dominant modes. The dashed black lines correspond to the ringdown frequencies of the *prograde spheroidal modes* $\omega_{22}^{\mathrm{RD}}$ and $\omega_{21}^{\mathrm{RD}}$ in the left and right panels, respectively.

Figure 5.25: Time domain representation of the negative modes shown in Figure 5.23. The inverse Fourier transform for IMRPhenomXPHM and M&B has been computed only for the positive frequencies, since the negative contribution can be neglected.

CHAPTER 6

Conclusions

Waveform modelling has become a major effort of the gravitational wave research community. Accurate models of the signals are essential tools to determine the source parameters of the detected events, which have increased considerably after the improvements of the detectors' sensitivity. Parameter estimation is based on Bayesian analysis, which requires millions of evaluations to determine posterior distributions of the source parameters, and computationally efficient models are thus required to perform this procedure. The UIB group has pioneered the development of phenomenological waveform models, which consist of closed-form expressions based on analytical ansätze calibrated to numerical relativity waveforms, typically developed in the time domain. Most recently, it has lead the construction of the phenomenological frequency domain family IMRPhenomX [57, 89–97], and has developed the first phenomenological time domain family IMRPhenomT [98–100].

Since the noise characterization and the detector's response are described in the frequency domain, frequency domain models are preferred for data analysis. However, these models rely on several approximations, which tend to fail in some regions of the parameter space. In order to achieve analytical expressions in the Fourier domain, previous work has employed the SPA described in Section 4.1, which fails for rapidly changing phases. Although the inspiral evolution of binaries does have slowly varying phase, this does not happen for the latest stages, where the SPA would not be applicable. For non-precessing systems, this can be fixed by calibrating the last orbits to numerical relativity data, since there this smaller parameter space has already been covered well by numerical relativity simulations, apart from the more extreme regions of high mass ratios and very large black hole spins. For precessing binaries, which are the main topic of this project, we have seen that the binary evolution is affected by a time domain modulation. This effect does not modify the radiated energy, but modulates the amplitude of the signal. A promising approach to deal with this modulation is to construct a non-inertial rotation from the co-precessing signal, which can be approximated by the corresponding aligned-spin waveform, to the inertial one [6]. This description is naturally formulated in the time domain, and it is still a challenge to translate it to the frequency domain. Current approaches use the SPA, which again fails at late stages of the coalescence due to the limitations of the approximation. Indeed, these limitations have encouraged the development of time domain models, which do not suffer from these drawbacks. Regarding the phenomenological models, IMRPhenomT was developed to overcome the limitations of the IMRPhenomX family, which is not recommended for high mass events where the detectors are only sensitive to the problematic phases where the SPA fails. A comparison

of the performance of these two models can be found in two of the latest publications of the UIB group: the reanalysis of the GWTC1 catalog [131] and of the GW190521 event [52]. These studies support both the advantages and failures of IMRPhenomX, preferring IMRPhenomT only for events with high masses.

Despite these approximations, frequency domain models, and concretely the IMRPhenomX family, have been widely used in gravitational wave data analysis with surprisingly good performance and very low computational cost. Therefore, as an attempt to maintain the simplicity of the IMRPhenomX family, this project was motivated by seeking an alternative way to deal with precession that would not require of a very complicated approach. If one could surpass the limitations of the SPA without involving complex procedures, then it would be possible to reduce the urgency to provide a good coverage of the precessing parameter space by NR simulations. For precessing systems the parameter space has four dimensions more than the non-precessing parameter space, which makes it much more difficult and computationally expensive to cover it. Following this idea, in this work I implemented the procedure explained in Ref. [8] to deal with precession, which does not rely on the SPA. Once the method was translated to the usual LVC conventions of Fourier transforms (specified in Appendix A), we have tested its performance in different regions of the parameter space and compared its results with IMRPhenomX, IMRPhenomT and in the last Section 5.2, we also compared it with a NR simulation. This has shown that the M&B procedure does imply an improvement over the underlying SPA of IMRPhenomXPHM, but only for some regions in the parameter space. For instance, in Sec. 5.1 we have seen that for anti-aligned spin systems (case $--$ and GW190521 in Table 5.1), the M&B results are considerably better. This enhancement can also be seen in the NR comparison in Section 5.2 for the higher $h_{2\pm1}$ harmonics. Actually, the results we obtained do not suggest that the M&B algorithm does not work properly, but mostly that IMRPhenomXPHM performs reasonably well despite the approximations.

A key element of the analysis in this work has been to not only separately analyze different spherical harmonic mode contributions as is commonly done, but also to separately investigate positive and negative frequency contributions to the waveform, which are associated with different transfer functions. In order to understand the ringdown behaviour we compared the frequency domain description with the time domain description, and we have seen identified beating between prograde and retrograde excitations in one of the binary systems we have analyzed in detail.

Perhaps the most important conclusions to draw from this project concern the perspectives for the next steps in modelling precession in the frequency domain, and concretely for how the IMRPhenomXPHM model can be improved. Given not only the large computational cost of exploring the precessing parameter space with numerical relativity simulations, but also the required resources in terms of researchers, the strategy here has been to first extend analytical methods as much as possible, and develop further tools and techniques to analyze precessing waveforms. What has been found is that in practice, the M&B method is limited by the need to take high order derivatives and by operating on the inertial frame waveforms, which are more complex than waveforms in the inertial frame, resulting in a complicated behaviour across the parameter space. This fact makes it seem unlikely that the method can be applied successfully before further improvements have been made to the time domain models, such as a development of more accurate and in particular smoother descriptions for the Euler angles. The most promising avenue forward thus seems to be the calibration of IMRPhenomXPHM to numerical

relativity. Given that IMRPhenomXPHM already provides a good description of the inspiral, such a calibration can focus on the merger and ringdown. Regarding the ringdown, we have seen that beating between the prograde and retrograde excitations can modify the ringdown frequency, and thus a first step should be to take this beating into account and focus on modelling only the beating frequency. Such an improvement could be expected to already significantly reduce the parameter bias for massive events like GW190521. We have also seen that this beating is particularly relevant for configurations with negative spins.

The M&B algorithm does however introduce a completely different and interesting approach to precession, and now that it has been coded up with Fourier transform conventions that are consistent with IMRPhenomXPHM and other work within the LVC, we will be able to test it as the underlying co-precessing modes and angles are improved, and then evaluate again if an efficient computational implementation of the method would be worth it, possible to improve the late inspiral phase of post-Newtonian descriptions, where the accuracy of the SPA is already reduced.

Appendices

APPENDIX A

Fourier Domain Representation

The Fourier transform $\tilde{x}(t)$ of a time series $x(t)$ consists of decomposing it into its sine and cosine representation, according to

$$\tilde{x}(f) = \frac{1}{\sqrt{2\pi}} \int_{-\infty}^{\infty} dt x(t) e^{-i2\pi ft}. \tag{A.0.1}$$

The inverse Fourier transform is then given by

$$x(t) = \frac{1}{\sqrt{2\pi}} \int_{-\infty}^{\infty} df \tilde{x}(f) e^{i2\pi ft}. \tag{A.0.2}$$

The parameter f has dimensions of $1/t$, and it is interpreted as a frequency. In general, the inverse Fourier transform $\tilde{x}(f)$ is a complex function of the frequency, which has the property

$$\tilde{x}(-f) = \tilde{x}^*(f) \text{ if } x(t) \in \mathbb{R}. \tag{A.0.3}$$

In gravitational wave data analysis it is typical to work with data sets that correspond to a constant sampling frequency, so that the observed data is an equally spaced time series as in Eq. (1.3.1). Hence, we need to define the *discrete Fourier transform* (DFT), the operation in Equation (A.0.1) but appropriate for a finite set of discretely-sampled points. The DFT of the discrete samples $x_j = x(t_0 + \Delta j), j = 0, ..., N-1$ is defined, in our conventions, as

$$\tilde{x}(f_k) = \tilde{x}_k = \Delta t \sum_{j=0}^{N-1} x_j e^{-i2\pi jk/N}, \tag{A.0.4}$$

where $f_k = k\Delta f = \frac{k}{N\Delta t}$, with $k = -n/2, -N/2+1, ..., N/2-1$. The inverse discrete Fourier transform (IDFT) is then defined as

$$x(t_j) = x_j = \frac{1}{\Delta t N} \sum_{k=-N/2}^{N/2-1} \tilde{x}_k e^{-i2\pi jk/N}. \tag{A.0.5}$$

The DFT and IDFT assume that the signal is periodic with period $N\Delta t$. However, the rate at which we sample the signal determines if the finite set of samples can reconstruct the complete signal, and it is given by the Sampling Theorem[136]:

Theorem A.0.1 (**Sampling Theorem**). *If a continuous time signal contains no frequency components higher than the so called Nyquist frequency f_{Ny}, then it can be completely determined by uniform samples taken at a rate f_s twice the Nyquist frequency or higher:*

$$\text{If } \tilde{x}(f) = 0 \text{ for } |f| \geq f_{Ny} \Rightarrow \ f_s \geq 2f_{Ny} \text{ or } \Delta t \leq \frac{1}{2f_{Ny}}. \tag{A.0.6}$$

A.1 Parseval's Theorem and the Power Spectral Density

Parseval's theorem establishes the relation between the integrals of the absolute squares of $x(t)$ and its Fourier transform $\tilde{x}(f)$, which is usually called the energy present in the signal

$$E = \int_{-\infty}^{\infty} dt|x(t)|^2 = \int_{-\infty}^{\infty} dt|\tilde{x}(f)|^2. \tag{A.1.1}$$

We define $E_x(f) = |\tilde{x}(f)|^2$ as the *Energy Spectral Density* of the signal. In general, the total energy E is confined if x is a square-integrable function. This is however not true for finite sets of data such as our case, where the total energy becomes infinity. In those cases it is thus useful to define a well-defined quantity, the total power P, as

$$P = \lim_{T\to\infty} \frac{1}{T} \int_{-T/2}^{T/2} dt|x(t)|^2 = \int_{-\infty}^{\infty} df P_x(f) = \int_0^{\infty} S_x(f), \tag{A.1.2}$$

where the *Power Spectral Density* (PSD) $P_x(f)$ is defined as

$$P_x(f) = \lim_{T\to\infty} \frac{1}{T} \int_{-\infty}^{\infty} \left| \int_{-T/2}^{T/2} dt x(t) e^{-i2\pi ft} \right|^2 = \lim_{T\to\infty} \frac{1}{T} \left|\tilde{x}_T(f)\right|^2, \tag{A.1.3}$$

where $\tilde{x}_T(f)$ denotes the Fourier transform of $x(t)$ between $-T/2$ and $T/2$.

The second equality in Equation (A.1.2) holds by applying Parseval's Theorem (A.1.1) and the definition of the Fourier transform (A.0.1). If the integral is over the positive frequencies, then the *One-Sided Power Spectral Density* $S_x(f) = 2P_x(f)$, and the definition requires a factor 2 in Equation (A.1.3).

A.2 Convolution Theorem

The convolution of an input signal $x(t)$ and the system impulse response $K(t)$ in a *linear system* is defined in the time domain as

$$(x * K)(t) = \int_{-\infty}^{\infty} dt' x(t') K(t - t'). \tag{A.2.1}$$

The convolution theorem establishes that the convolution in the time domain is the multiplication of the Fourier transforms in the frequency domain

$$(x * K)(t) \Longleftrightarrow \tilde{x}(f)\tilde{K}(f), \tag{A.2.2}$$

where $\tilde{K}(f)$ is usually called the transfer function or kernel.

A.3 Correlation Theorem

The correlation of two functions $x(t)$ and $y(t)$ is a measure of the match in shape between the two signals when they are shifted relative to one another by an amount t

$$(x \otimes y)(t) = \int_{-\infty}^{\infty} dt' x(t') y(t + t'). \tag{A.3.1}$$

The correlation theorem establishes that

$$(x \otimes y)(t) \Longleftrightarrow \tilde{x}^*(f)\tilde{y}(f). \tag{A.3.2}$$

Parseval's Theorem (A.1.1) is the special case where $y = x$ at $t = 0$.

Finally, one can define the *auto-correlation function* of a time series $x(t)$, $C_x(t)$, setting $x = y$ and an appropriate normalization so that the integral does not diverge:

$$C_x(t) = \lim_{T\to\infty} \int_{-T/2}^{T/2} dt' x(t')x(t+t'). \tag{A.3.3}$$

Using this last definition for the auto-correlation function, one can rewrite the Power Spectral Density (A.1.3) as

$$P_x(f) = \int_{-\infty}^{\infty} dt C_x(t) e^{-i2\pi ft}. \tag{A.3.4}$$

This last expression implies that the Fourier transform of the auto-correlation function $C_x(t)$ is the power spectral density $P_x(t)$.

Bibliography

[1] The LIGO Scientific Collaboration and the Virgo Collaboration, "Observation of Gravitational Waves from a Binary Black Hole Merger", Phys. Rev. Lett. **116**, 061102 (2016).

[2] B. P. Abbott et al., "GWTC-1: A Gravitational-Wave Transient Catalog of Compact Binary Mergers Observed by LIGO and Virgo during the First and Second Observing Runs", Phys. Rev. X **9**, 031040 (2019).

[3] B. P. Abbott et al., "GWTC-2: Compact Binary Coalescences Observed by LIGO and Virgo During the First Half of the Third Observing Run", arXiv:2010.14527 (2021).

[4] A. Buonanno, Y. Chen, and M. Vallisneri, "Detecting gravitational waves from precessing binaries of spinning compact objects: Adiabatic limit", Phys. Rev. D **67**, 104025 (2003).

[5] A. Buonanno, Y. Chen, and T. Damour, "Transition from inspiral to plunge in precessing binaries of spinning black holes", Phys. Rev. D **74**, 104005 (2006).

[6] P. Schmidt et al., "Tracking the precession of compact binaries from their gravitational-wave signal", Phys. Rev. D **84**, 024046 (2011).

[7] P. Schmidt, M. Hannam, and S. Husa, "Towards models of gravitational waveforms from generic binaries: A simple approximate mapping between precessing and non-precessing inspiral signals", Phys. Rev. D **86**, 104063 (2012).

[8] S. Marsat and J. G. Baker, "Fourier-domain modulations and delays of gravitational-wave signals", arXiv:1806.10734 (2018).

[9] C. Cutler and É. E. Flanagan, "Gravitational waves from merging compact binaries: How accurately can one extract the binary's parameters from the inspiral waveform?", Phys. Rev. D **49**, 2658–2697 (1994).

[10] The LIGO Scientific Collaboration and The Virgo Collaboration, "GW170817: Observation of Gravitational Waves from a Binary Neutron Star Inspiral", Phys. Rev. Lett. **119**, 161101 (2017).

[11] R. Abbott et al. (LIGO Scientific, KAGRA, VIRGO), "Observation of Gravitational Waves from Two Neutron Star–Black Hole Coalescences", Astrophys. J. Lett. **915**, L5 (2021).

[12] M. Sieniawska and M. Bejger, "Continuous Gravitational Waves from Neutron Stars: Current Status and Prospects", Universe **5**, 217 (2019).

[13] S. Kalita and B. Mukhopadhyay, "Continuous gravitational wave from magnetized white dwarfs and neutron stars: possible missions for LISA, DECIGO, BBO, ET detectors", Mon. Not. Roy. Astron. Soc. **490**, [Erratum: Mon.Not.Roy.Astron.Soc. 491, 4396–4397 (2020)], 2692–2705 (2019).

[14] N. Christensen, "Stochastic gravitational wave backgrounds", Reports on Progress in Physics **82**, 016903 (2018).

[15] A. W. G., P. R. Brady, J. D. E. Creighton, and É. É. Flanagan, "A power filter for the detection of burst sources of gravitational radiation in interferometric detectors", International Journal of Modern Physics D **09**, 303–307 (2000).

[16] M. P. Haugan and C. Lämmerzahl, "Principles of Equivalence: Their Role in Gravitation Physics and Experiments That Test Them", Lecture Notes in Physics, 195–212.

[17] A. Einstein, "Die Feldgleichungen der Gravitation", Sitzungsber. Preuss. Akad. Wiss. Berlin, 844–847 (1915).

[18] A. Einstein, "Näherungsweise Integration der Feldgleichungen der Gravitation. (German) [Approximate integration of the field equations of gravitation]", German, Sitzungsber. Preuss. Akad. Wiss. Berlin, 688–696 (1916).

[19] S. M. Carroll, *Spacetime and Geometry* (Cambridge University Press, July 2019).

[20] J. M. Weisberg, J. H. Taylor, and L. A. Fowler, "Gravitational waves from an orbiting pulsar", Scientific American **245**, 74–82 (1981).

[21] *Virgo*, https://www.virgo-gw.eu/.

[22] *GEO*, https://www.geo600.org/.

[23] *LIGO Laboratory Caltech*, http://www.ligo.caltech.edu/news/ligo20200326.

[24] *KAGRA Large-scale Cryogenic Graviational wave Telescope Project*, https://gwcenter.icrr.u-tokyo.ac.jp/en/.

[25] R. Abbott et al. (LIGO Scientific, Virgo), "GW190412: Observation of a Binary-Black-Hole Coalescence with Asymmetric Masses", Phys. Rev. D **102**, 043015 (2020).

[26] R. Abbott, T. D. Abbott, S. Abraham, F. Acernese, K. Ackley, C. Adams, R. X. Adhikari, V. B. Adya, C. Affeldt, M. Agathos, and et al., "GW190814: Gravitational Waves from the Coalescence of a 23 Solar Mass Black Hole with a 2.6 Solar Mass Compact Object", The Astrophysical Journal **896**, L44 (2020).

[27] R. Abbott et al. (LIGO Scientific, Virgo), "GW190521: A Binary Black Hole Merger with a Total Mass of $150M_{\odot}$", Phys. Rev. Lett. **125**, 101102 (2020).

[28] R. Abbott et al. (LIGO Scientific, Virgo), "Properties and Astrophysical Implications of the 150 $M_{\odot}$ Binary Black Hole Merger GW190521", Astrophys. J. Lett. **900**, L13 (2020).

[29] *LIGO India*, https://www.ligo-india.in/.

[30] *Einstein Telescope*, http://www.et-gw.eu/.

[31] *LISA Consortium*, https://www.lisamission.org/.

[32] *LIGO - A Gravitational-Wave Interferometer*, https://www.ligo.caltech.edu/page/ligo-gw-interferometer.

[33] P. Barriga et al., "AIGO: A southern hemisphere detector for the worldwide array of ground-based interferometric gravitational wave detectors", Classical and Quantum Gravity **27**, 084005 (2013).

[34] D. V. Martynov et al., "Sensitivity of the Advanced LIGO detectors at the beginning of gravitational wave astronomy", Phys. Rev. D **93**, 112004 (2018).

[35] C. J. Moore, R. H. Cole, and C. P. L. Berry, "Gravitational-wave sensitivity curves", Class. Quant. Grav. **32**, 015014 (2015).

[36] L. Wainstein and V. Zubakov, *Extraction of Signals from Noise* (Prentice-Hall, Englewood Cliffs, NJ, 1962).

[37] M. Maggiore, *Gravitational Waves (Volume I)* (Oxford University Press, 2007).

[38] J. Roulet, L. Dai, T. Venumadhav, B. Zackay, and M. Zaldarriaga, "Template Bank for Compact Binary Coalescence Searches in Gravitational Wave Data: A General Geometric Placement Algorithm", Phys. Rev. D **99**, 123022 (2019).

[39] B. Allen, "χ^2 time-frequency discriminator for gravitational wave detection", Phys. Rev. D **71**, 062001, 062001 (2005).

[40] S. A. Usman et al., "The PyCBC search for gravitational waves from compact binary coalescence", Class. Quant. Grav. **33**, 215004 (2016).

[41] J. Veitch et al., "Parameter estimation for compact binaries with ground-based gravitational-wave observations using the LALInference software library", Phys. Rev. D **91**, 042003 (2015).

[42] E. Thrane and C. Talbot, "An introduction to Bayesian inference in gravitational-wave astronomy: Parameter estimation, model selection, and hierarchical models", Publications of the Astronomical Society of Australia **36**, e010 (2019).

[43] K. Schwarzschild, "On the gravitational field of a mass point according to Einstein's theory", Sitzungsber. Preuss. Akad. Wiss. Berlin, 189–196 (1916).

[44] M. D. Kruskal, "Maximal extension of schwarzschild metric", Phys. Rev. **119**, 1743–1745 (1960).

[45] R. P. Kerr, "Gravitational Field of a Spinning Mass as an Example of Algebraically Special Metrics", Phys. Rev. Lett. **11**, 237–238 (1963).

[46] E. T. Newman, E. Couch, K. Chinnapared, A. Exton, A. Prakash, and R. Torrence, "Metric of a rotating, charged mass", Journal of Mathematical Physics **6**, 918–919 (1965).

[47] W. Israel, "Event horizons in static vacuum space-times", Phys. Rev. **164**, 1776–1779 (1967).

[48] B. Carter, "Axisymmetric Black Hole Has Only Two Degrees of Freedom", Phys. Rev. Lett. **26**, 331–333 (1971).

[49] V. P. Frolov and I. D. Novikov, eds., *Black hole physics: Basic concepts and new developments* (1998).

[50] J. R. Oppenheimer and G. M. Volkoff, "On Massive Neutron Cores", Physical Review **55**, 374–381 (1939).

[51] G. Rakavy and G. Shaviv, "Instabilities in Highly Evolved Stellar Models", Astrophysical Journal **148**, 803 (1967).

[52] H. Estellés et al., "A detailed analysis of GW190521 with phenomenological waveform models", (2021).

[53] P. C. Peters, "Gravitational Radiation and the Motion of Two Point Masses", Phys. Rev. **136**, B1224–B1232 (1964).

[54] L. Blanchet, "Gravitational radiation from post-Newtonian sources and inspiralling compact binaries", Living Rev. Rel. **9**, 4 (2006).

[55] J. N. Goldberg, A. J. Macfarlane, E. T. Newman, F. Rohrlich, and E. C. G. Sudarshan, "Spin-s Spherical Harmonics and ð", J. Math. Phys. **8**, 2155–2161 (1967).

[56] Y. Wiaux, L. Jacques, and P. Vandergheynst, "Fast spin +-2 spherical harmonics transforms", J. Comput. Phys. **226**, 2359–2371 (2007).

[57] L. London, S. Khan, E. Fauchon-Jones, C. García, M. Hannam, S. Husa, X. Jiménez-Forteza, C. Kalaghatgi, F. Ohme, and F. Pannarale, "First higher-multipole model of gravitational waves from spinning and coalescing black-hole binaries", Phys. Rev. Lett. **120**, 161102 (2018).

[58] N. Andersson, "Evolving test fields in a black hole geometry", Phys. Rev. D **55**, 468–479 (1997).

[59] S. A. Teukolsky, "Rotating black holes - separable wave equations for gravitational and electromagnetic perturbations", Phys. Rev. Lett. **29**, 1114–1118 (1972).

[60] S. A. Teukolsky, "Perturbations of a rotating black hole. 1. Fundamental equations for gravitational electromagnetic and neutrino field perturbations", Astrophys. J. **185**, 635–647 (1973).

[61] E. Berti and A. Klein, "Mixing of spherical and spheroidal modes in perturbed Kerr black holes", Phys. Rev. D **90**, 064012 (2014).

[62] B. J. Kelly and J. G. Baker, "Decoding mode mixing in black-hole merger ringdown", Phys. Rev. D **87**, 084004 (2013).

[63] L. London, "Notes on the spheroidal harmonic multipole moments of gravitational radiation", arXiv:2006.11449 (2020).

[64] B. P. Abbott et al. (LIGO Scientific, Virgo), "The basic physics of the binary black hole merger GW150914", Annalen Phys. **529**, 1600209 (2017).

[65] F. Pretorius, "Evolution of Binary Black-Hole Spacetimes", Phys. Rev. L **95**, 121101 (2005).

[66] M. Campanelli et al., "Accurate Evolutions of Orbiting Black-Hole Binaries without Excision", Phys. Rev. L **96**, 111101 (2006).

[67] J. G. Baker et al., "Gravitational-Wave Extraction from an Inspiraling Configuration of Merging Black Holes", Phys. Rev. L **96**, 111102 (2006).

[68] A. Buonanno and T. Damour, "Effective one-body approach to general relativistic two-body dynamics", Phys. Rev. D **59**, 084006 (1999).

[69] T. Damour, "Coalescence of two spinning black holes: an effective one-body approach", Phys. Rev. D **64**, 124013 (2001).

[70] A. Taracchini, Y. Pan, A. Buonanno, E. Barausse, M. Boyle, T. Chu, G. Lovelace, H. P. Pfeiffer, and M. A. Scheel, "Prototype effective-one-body model for nonprecessing spinning inspiral-merger-ringdown waveforms", Phys. Rev. D **86**, 024011 (2012).

[71] T. Damour, A. Nagar, and S. Bernuzzi, "Improved effective-one-body description of coalescing nonspinning black-hole binaries and its numerical-relativity completion", Phys. Rev. D **87**, 084035 (2013).

[72] A. Taracchini et al., "Effective-one-body model for black-hole binaries with generic mass ratios and spins", Phys. Rev. D **89**, 061502 (2014).

[73] Y. Pan, A. Buonanno, A. Taracchini, L. E. Kidder, A. H. Mroué, H. P. Pfeiffer, M. A. Scheel, and B. Szilágyi, "Inspiral-merger-ringdown waveforms of spinning, precessing black-hole binaries in the effective-one-body formalism", Phys. Rev. D **89**, 084006 (2014).

[74] T. Damour, P. Jaranowski, and G. Schäfer, "Fourth post-Newtonian effective one-body dynamics", Phys. Rev. D **91**, 084024 (2015).

[75] A. Nagar, T. Damour, C. Reisswig, and D. Pollney, "Energetics and phasing of nonprecessing spinning coalescing black hole binaries", Phys. Rev. D **93**, 044046 (2016).

[76] M. Pürrer, "Frequency domain reduced order model of aligned-spin effective-one-body waveforms with generic mass-ratios and spins", Phys. Rev. D **93**, 064041 (2016).

[77] S. Babak, A. Taracchini, and A. Buonanno, "Validating the effective-one-body model of spinning, precessing binary black holes against numerical relativity", Phys. Rev. D **95**, 024010 (2017).

[78] A. Bohé et al., "Improved effective-one-body model of spinning, nonprecessing binary black holes for the era of gravitational-wave astrophysics with advanced detectors", Phys. Rev. D **95**, 044028 (2017).

[79] W. Del Pozzo and A. Nagar, "Analytic family of post-merger template waveforms", Phys. Rev. D **95**, 124034 (2017).

[80] T. Damour and A. Nagar, "The Effective-One-Body Approach to the General Relativistic Two Body Problem", Lect. Notes Phys. **905**, 273–312 (2016).

[81] A. Nagar, G. Riemenschneider, and G. Pratten, "Impact of Numerical Relativity information on effective-one-body waveform models", Phys. Rev. D **96**, 084045 (2017).

[82] A. Nagar, F. Messina, P. Rettegno, D. Bini, T. Damour, A. Geralico, S. Akcay, and S. Bernuzzi, "Nonlinear-in-spin effects in effective-one-body waveform models of spin-aligned, inspiralling, neutron star binaries", Phys. Rev. D **99**, 044007 (2019).

[83] A. Nagar et al., "Time-domain effective-one-body gravitational waveforms for coalescing compact binaries with nonprecessing spins, tides and self-spin effects", Phys. Rev. D **98**, 104052 (2018).

[84] S. Akcay, S. Bernuzzi, F. Messina, A. Nagar, N. Ortiz, and P. Rettegno, "Effective-one-body multipolar waveform for tidally interacting binary neutron stars up to merger", Phys. Rev. D **99**, 044051 (2019).

[85] A. Nagar and P. Rettegno, "Efficient effective one body time-domain gravitational waveforms", Phys. Rev. D **99**, 021501 (2019).

[86] R. Cotesta, A. Buonanno, A. Bohé, A. Taracchini, I. Hinder, and S. Ossokine, "Enriching the Symphony of Gravitational Waves from Binary Black Holes by Tuning Higher Harmonics", Phys. Rev. D **98**, 084028 (2018).

[87] R. Cotesta, S. Marsat, and M. Pürrer, "Frequency domain reduced order model of aligned-spin effective-one-body waveforms with higher-order modes", Phys. Rev. D **101**, 124040 (2020).

[88] S. Ossokine et al., "Multipolar Effective-One-Body Waveforms for Precessing Binary Black Holes: Construction and Validation", Phys. Rev. D **102**, 044055 (2020).

[89] S. Husa, S. Khan, M. Hannam, M. Pürrer, F. Ohme, X. Jiménez Forteza, and A. Bohé, "Frequency-domain gravitational waves from nonprecessing black-hole binaries. I. New numerical waveforms and anatomy of the signal", Phys. Rev. **D93**, 044006 (2016).

[90] S. Khan, S. Husa, M. Hannam, F. Ohme, M. Pürrer, X. Jiménez Forteza, and A. Bohé, "Frequency-domain gravitational waves from nonprecessing black-hole binaries. II. A phenomenological model for the advanced detector era", Phys. Rev. **D93**, 044007 (2016).

[91] M. Hannam, P. Schmidt, A. Bohé, L. Haegel, S. Husa, et al., "Simple Model of Complete Precessing Black-Hole-Binary Gravitational Waveforms", Phys.Rev.Lett. **113**, 151101 (2014).

[92] A. Bohé, M. Hannam, S. Husa, F. Ohme, M. Puerrer, and P. Schmidt, *Phenompv2 - technical notes for lal implementation*, tech. rep. LIGO-T1500602 (LIGO Project, 2016).

[93] S. Khan, K. Chatziioannou, M. Hannam, and F. Ohme, "Phenomenological model for the gravitational-wave signal from precessing binary black holes with two-spin effects", Phys. Rev. D **100**, 024059 (2019).

[94] S. Khan, F. Ohme, K. Chatziioannou, and M. Hannam, "Including higher order multipoles in gravitational-wave models for precessing binary black holes", Phys. Rev. D **101**, 024056 (2020).

[95] G. Pratten, S. Husa, C. Garcia-Quiros, M. Colleoni, A. Ramos-Buades, H. Estelles, and R. Jaume, "Setting the cornerstone for the IMRPhenomX family of models for gravitational waves from compact binaries: The dominant harmonic for non-precessing quasi-circular black holes", arXiv:2001.11412 (2020).

[96] C. García-Quirós, M. Colleoni, S. Husa, H. Estellés, G. Pratten, A. Ramos-Buades, M. Mateu-Lucena, and R. Jaume, "IMRPhenomXHM: A multi-mode frequency-domain model for the gravitational wave signal from non-precessing black-hole binaries", ArXiv:2001.10914 (2020).

[97] G. Pratten et al., "Let's twist again: computationally efficient models for the dominant and sub-dominant harmonic modes of precessing binary black holes", arXiv:2004.06503 (2020).

[98] H. Estellés, S. Husa, M. Colleoni, D. Keitel, M. Mateu-Lucena, C. García-Quirós, A. Ramos-Buades, and A. Borchers, "Time domain phenomenological model of gravitational wave subdominant harmonics for quasi-circular non-precessing binary black hole coalescences", arXiv:2012.11923 (2020).

[99] H. Estellés, A. Ramos-Buades, S. Husa, C. García-Quirós, M. Colleoni, L. Haegel, and R. Jaume, "IMRPhenomTP: A phenomenological time domain model for dominant quadrupole gravitational wave signal of coalescing binary black holes", arXiv:2004.08302 (2020).

[100] H. Estellés, M. Colleoni, C. García-Quirós, S. Husa, D. Keitel, M. Mateu-Lucena, M. d. L. Planas, and A. Ramos-Buades, "New twists in compact binary waveform modelling: a fast time domain model for precession", (2021).

[101] J. Blackman, S. E. Field, M. A. Scheel, C. R. Galley, D. A. Hemberger, P. Schmidt, and R. Smith, "A Surrogate Model of Gravitational Waveforms from Numerical Relativity Simulations of Precessing Binary Black Hole Mergers", Phys. Rev. D **95**, 104023 (2017).

[102] V. Varma, S. E. Field, M. A. Scheel, J. Blackman, L. E. Kidder, and H. P. Pfeiffer, "Surrogate model of hybridized numerical relativity binary black hole waveforms", Phys. Rev. D **99**, 064045 (2019).

[103] V. Varma, S. E. Field, M. A. Scheel, J. Blackman, D. Gerosa, L. C. Stein, L. E. Kidder, and H. P. Pfeiffer, "Surrogate models for precessing binary black hole simulations with unequal masses", Phys. Rev. Research. **1**, 033015 (2019).

[104] M. Favata, "The gravitational-wave memory effect", Class. Quantum Gravity **27**, 84036 (2010).

[105] M. Boyle et al., "Gravitational-wave modes from precessing black-hole binaries", arXiv:1409.4431 (2014).

[106] L. E. Kidder, "Coalescing binary systems of compact objects to (post)5/2-Newtonian order. V. Spin effects", Physical Review D **52**, 821–847 (1995).

[107] K. S. Thorne and J. B. Hartle, "Laws of motion and precession for black holes and other bodies", Phys. Rev. D **31**, 1815–1837 (1985).

[108] M. Hannam et al., "Simple Model of Complete Precessing Black-Hole-Binary Gravitational Waveforms", Phys. Rev. L **113**, 151101 (2014).

[109] A. Bohe, S. Marsat, G. Faye, and L. Blanchet, "Next-to-next-to-leading order spin-orbit effects in the near-zone metric and precession equations of compact binaries", Class. Quant. Grav. **30**, 075017 (2013).

[110] S. Marsat, A. Bohé, L. Blanchet, and A. Buonanno, "Next-to-leading tail-induced spin–orbit effects in the gravitational radiation flux of compact binaries", Class. Quant. Grav. **31**, 025023 (2014).

[111] K. Chatziioannou, A. Klein, N. Yunes, and N. Cornish, "Constructing Gravitational Waves from Generic Spin-Precessing Compact Binary Inspirals", Phys. Rev. D **95**, 104004 (2017).

[112] M. Boyle, R. Owen, and H. P. Pfeiffer, "A geometric approach to the precession of compact binaries", Phys. Rev. D **84**, 124011 (2011).

[113] L. Santamaria et al., "Matching post-Newtonian and numerical relativity waveforms: systematic errors and a new phenomenological model for non-precessing black hole binaries", Phys. Rev. D **82**, 064016 (2010).

[114] A. Bohé et al., "PhenomPv2 - Technical notes for the LAL implementation", PhenomPv2 - Technical notes for the LAL implementation (2016).

[115] C. García-Quirós, S. Husa, M. Mateu-Lucena, and A. Borchers, "Accelerating the evaluation of inspiral-merger-ringdown waveforms with adapted grids", ArXiv:2001.10897 (2020).

[116] LIGO Scientific Collaboration, *LIGO Algorithm Library - LALSuite*, free software (GPL), 2018.

[117] V. Varma, D. Gerosa, L. C. Stein, F. Hébert, and H. Zhang, "High-accuracy mass, spin, and recoil predictions of generic black-hole merger remnants", Phys. Rev. Lett. **122**, 011101 (2019).

[118] A. Ramos-Buades, P. Schmidt, G. Pratten, and S. Husa, "Validity of common modeling approximations for precessing binary black holes with higher-order modes", Phys. Rev. D **101**, 103014 (2020).

[119] E. P. Wigner, *Group theory and its application to the quantum mechanics of atomic spectra* (Academic Press, New York, 1959), p. 372.

[120] L. M. Thomas, P. Schmidt, and G. Pratten, "New effective precession spin for modeling multimodal gravitational waveforms in the strong-field regime", Phys. Rev. D **103**, 083022 (2021).

[121] Y. Mino, M. Sasaki, and T. Tanaka, "Gravitational radiation reaction: Chapter 7", Prog. Theor. Phys. Suppl. **128**, 373–406 (1997).

[122] T. A. Apostolatos, C. Cutler, G. J. Sussman, and K. S. Thorne, "Spin induced orbital precession and its modulation of the gravitational wave forms from merging binaries", Phys. Rev. D **49**, 6274–6297 (1994).

[123] L. E. Kidder, "Coalescing binary systems of compact objects to postNewtonian 5/2 order. 5. Spin effects", Phys. Rev. D **52**, 821–847 (1995).

[124] P. Schmidt, F. Ohme, and M. Hannam, "Towards models of gravitational waveforms from generic binaries II: Modelling precession effects with a single effective precession parameter", Phys. Rev. D **91**, 024043 (2015).

[125] A. Klein, N. Cornish, and N. Yunes, "Gravitational waveforms for precessing, quasicircular binaries via multiple scale analysis and uniform asymptotics: The near spin alignment case", Phys. Rev. D **88**, 124015 (2013).

[126] A. Klein, N. Cornish, and N. Yunes, "Fast Frequency-domain Waveforms for Spin-Precessing Binary Inspirals", Phys. Rev. D **90**, 124029 (2014).

[127] R. O'Shaughnessy, L. London, J. Healy, and D. Shoemaker, "Precession during merger: Strong polarization changes are observationally accessible features of strong-field gravity during binary black hole merger", Phys. Rev. D **87**, 044038 (2013).

[128] R. Courant and D. Hilbert, *Methods of mathematical physics*, Vol. 1 (Wiley, New York, 1989).

[129] A. Mroue, M. Boyle, G. Lovelace, B. Szilagyi, H. Pfeiffer, A. Zenginoglu, L. Kidder, N. Taylor, D. Hemberger, and M. Scheel, *Binary black-hole simulation sxs:bbh:0037* (Zenodo, July 2019).

[130] M. Colleoni, M. Mateu-Lucena, H. Estellés, C. García-Quirós, D. Keitel, G. Pratten, A. Ramos-Buades, and S. Husa, "Towards the routine use of subdominant harmonics in gravitational-wave inference: Reanalysis of GW190412 with generation X waveform models", Phys. Rev. D **103**, 024029 (2021).

[131] M. Mateu-Lucena, S. Husa, M. Colleoni, H. Estellés, C. García-Quirós, D. Keitel, M. d. L. Planas, and A. Ramos-Buades, "Adding harmonics to the interpretation of the black hole mergers of GWTC-1", (2021).

[132] G. Ashton et al., "BILBY: A user-friendly Bayesian inference library for gravitational-wave astronomy", Astrophys. J. Suppl. **241**, 27 (2019).

[133] R. J. E. Smith, G. Ashton, A. Vajpeyi, and C. Talbot, "Massively parallel Bayesian inference for transient gravitational-wave astronomy", Mon. Not. Roy. Astron. Soc. **498**, 4492–4502 (2020).

[134] X. Jiménez-Forteza, D. Keitel, S. Husa, M. Hannam, S. Khan, and M. Pürrer, "Hierarchical data-driven approach to fitting numerical relativity data for nonprecessing binary black holes with an application to final spin and radiated energy", Phys. Rev. D **95**, 064024 (2017).

[135] C. Cutler, "Angular resolution of the LISA gravitational wave detector", Phys. Rev. D **57**, 7089–7102 (1998).

[136] C. Shannon, "Communication in the Presence of Noise", Proceedings of the IRE **37**, 10–21 (1949).